Flow Visualizations of Perpendicular Blade Vortex Interactions

Semi-Annual Progress Report Submitted to NASA Langley
under Research Award NAG-1-1119 for the period ending October 15 1992

Michael C. Rife and William J. Devenport
Department of Aerospace and Ocean Engineering
Virginia Polytechnic Institute and State University
Blacksburg, VA 24060

ABSTRACT

Helium bubble flow visualizations of have been performed to study the perpendicular interaction of a turbulent trailing vortex and a rectangular wing in the Virginia Tech Stability Tunnel. Many combinations of vortex strength, vortex-blade separation (z_s) and blade angle of attack were studied. Photographs of representative cases are presented. A range of phenomena were observed. For z_s greater than a few percent chord the vortex is deflected as it passes the blade under the influence of the local streamline curvature and its image in the blade. Initially the interaction appears to have no influence on the core. Downstream, however, the vortex core begins to diffuse and grow, presumably as a consequence of its interaction with the blade wake. The magnitude of these effects increases with reduction in z_s. For z_s near zero the form of the interaction changes and becomes dependent on the vortex strength. For lower strengths the vortex appears to split into two filaments on the leading edge of the blade, one passing on the pressure and one passing on the suction side. At higher strengths the vortex bursts in the vicinity of the leading edge. In either case the core or its remnants then rapidly diffuse with distance downstream. Increase in Reynolds number did not qualitatively affect the flows apart from decreasing the amplitude of the small low-frequency wandering motions of the vortex. Changes in wing tip geometry and boundary layer trip had very little effect.

1. INTRODUCTION

In general blade vortex interactions are both three-dimensional and unsteady. Most often, however, two idealized cases are studied (figure 1). The first (figure 1a) is where the vortex is parallel to the leading edge of the blade. This type of interaction is two-dimensional and unsteady. The second (figure 1b) is where the vortex is perpendicular to the blade. This is known as blade wake interaction (BWI) and is fairly steady but highly three-dimensional. Examining and understanding BWI is the primary purpose of the work described in this report.

BWI noise has been identified by Brooks and Martin (1987) as the most important contributor to helicopter noise during level flight and mild climb conditions. This noise source mechanism has been shown by Brooks, Marcolini, and Pope (1987) and Glegg (1989) to be the result of interaction of the rotor blades with turbulence associated with the tip vortices in the rotor disk plane. Glegg and Devenport (1991) and Devenport et al. (1992) attempted to predict this noise by studying the turbulence structure of trailing vortices in isolation and incorporating these results into a BWI noise prediction scheme. The assumption here was that the impact of the blade did not significantly alter the turbulence structure from the point of view of noise prediction. However, this assumption did not appear to be valid - the turbulence structure of the isolated vortex was insufficient to account for all BWI noise generated. There are two possibilities here; either changes in the flow structure during the interaction strongly effect the noise produced or, the

vortex structure is significantly altered by its encounter with the blade, changing the nature of all subsequent interactions. To cover both these possibilities a study of the details of the interaction and the flow it produces is required.

There has been surprisingly little research into the fluid mechanics of BWI. What has been done has concentrated primarily on effects on the aerodynamic characteristics of the blade rather than on the vortex itself. Kalkhoran, Wilson, and Seath (1992) studied transonic perpendicular blade vortex interactions at Mach numbers of .68 to .9 and Reynolds numbers based on chord of 3.8×10^6 to 5.5×10^6. They used a NACA 0012 wing instrumented with static pressure taps for the interaction. They took pressure rake measurements at the leading and trailing edge of the blade as well as pressure measurements on the blade surface under the vortex. They found the vortex to significantly affect the pressure distribution on the blade for only the first 30% of the chord. This was due to spanwise drift of the vortex across the wing caused by the vortex image. Schlinker and Amiet (1983) performed three-dimensional blade vortex interaction experiments using hot wires to measure the vortex core. They determined the acoustic signature after the interaction and concluded that the ingestion of the vortex into the rotor plane generates harmonic noise and impulsive wave forms. Seath and Wilson (1986) conducted studies of a perpendicular blade vortex interaction at 200ft/s and Reynolds numbers of 500,000 per foot. An 11 inch chord NACA 0015 wing was used as a vortex generator and a 10 inch chord NACA 64A015 wing with chord wise pressure taps as the blade. They also saw significant changes in the pressure distribution on the blade in the vicinity of the vortex and observed a spanwise drift of the vortex over the blade surface.

Phillipe and Armand (1978) used two NACA 0012 wings to study blade vortex interactions at higher speeds (M=0.6). They found the vortex interaction to cause a loss of lift on the blade and an increase in its drag of approximately 40%.

The aim of this investigation is to examine and understand the details of perpendicular blade vortex interactions and the flows they produce over a range of conditions, with a view to improving BWI noise prediction. The investigation is split into two parts, (i) helium-bubble flow visualizations to examine the nature of the interactions and the gross features of the resulting flows, and (ii) detailed three-component hot-wire velocity measurements in those flows. This report describes the results of the flow visualizations.

2. EQUIPMENT

2.1 Wind Tunnel

Experiments were performed in the Virginia Tech Stability Wind Tunnel (figure 2). It is a closed-circuit tunnel powered by a 600 horsepower axial fan. The test section is square with a cross section of 1.83m X 1.83m and a length of 7.33m. Flow in the empty test section is closely uniform with a turbulence intensity of less than 0.05% (see Choi and Simpson (1987)). One side of the test section is made of plexiglas and glass panels through which observations are made.

2.2 Wing models

Mason and Marchman's (1972) wing model was used along with a copy produced on a numerically controlled milling machine. Both models have a rectangular planform, NACA 0012 airfoil section and a blunt wing tip. The chord and span are .20 m and 1.22m respectively. Mason and Marchman's wing is made from solid brass while the copy is made from solid aluminum. Surfaces of both wings are accurate to within ±.25mm.

The aluminum model was used as the vortex generator. It was mounted vertically as a half wing at the center of the upper wall of the test section entrance (figure 3). Its

root was held cantilever fashion in a turntable and cable assembly (figure 4), this allowing the wing to be rotated to angle of attack about its quarter chord location. In this arrangement 0.89m of this wing protruded into the test section flow. The brass model, used as the interaction blade, was mounted in a similar manner some 14 chord lengths downstream (figure 3), its effective span being 1.0m. Here the mount consisted primarily of two large aluminum beams resting on the tunnel superstructure (figure 5). These allowed the angle of attack and lateral position to be independently adjusted.

The wing models were initially placed at zero angle of attack, with an accuracy of $\pm 0.2°$ by using a removable wing tip holding 48 static pressure ports. The tip was first placed on the rear wing and used to position it at zero angle of attack by equalizing the static pressures on both sides. The forward wing was then put in place and zeroed in a similar manner.

To eliminate possible unsteadiness and non-uniformity that might result from natural transition, the boundary layers on the wings were tripped. Glass beads with a diameter of 0.5mm were glued to the wings in a random pattern in a strip extending between 20% and 40% chord locations. Average density was 200 beads/cm^2. The resulting turbulent boundary layers were documented for a range of angles of attack by Devenport et al. (1992).

2.3 Helium Bubble Generator, Lighting, Photography

The flow visualizations were performed using a Model 5 console helium bubble generator with two "plug in" heads produced by Sage Action Inc. (figure 6). The generator produces helium filled soap bubbles by supplying bubble film solution, helium, and compressed air to the heads. The heads generate bubbles using a double hypodermic tube. Bubbles are then passed through two "vortex" filters which centrifuge out heavier than air bubbles. They leave the filters through two 12.7mm diameter plastic tubes which in this investigation were connected to two pieces of 4.8mm thick aluminum tubing of airfoil cross section. The airfoil tubing allowed bubbles to be injected into the flow with minimal interference. Tubes were mounted 1.0m upstream of the forward wing tip. At no time did the bubble probes have any visible effects on the flow.

The helium bubbles were illuminated using a Varian arc lamp (model p150s-7) supplied by Sage Action Inc. The arc lamp was mounted at the downstream end of the test section on a moveable mount. This mount allowed the light to be placed at the best position for illumination of the vortex. It was adjusted to produce a well defined narrow light beam aligned with the vortices. The amount of unnecessary scattered light was therefore minimized. The side of the test section opposite the plexiglas and glass panels, and the floor of the test section were covered with flat black plastic sheet to improve the visibility of the helium bubbles.

Over 1000 photographs were taken using a Nikon N6006 camera with ASA 1600 color film using exposure times varying between 0.5s to 2.0s and aperture settings varying between f/1.8 to f/4. Several hours of video film were taken using a standard video camera.

3. RESULTS AND DISCUSSION

The coordinate system shown in figure 3 will be used in describing the results of the flow visualizations. The direction of the free stream flow is along the x axis, the y axis is vertical and parallel to the wing spans, z is parallel to the direction of lift. The origin of the coordinate system is the leading edge of the tip of the vortex-generating wing.

Most flow visualizations were performed at Reynolds numbers based on chord ($Re_c=U_{ref}c/\nu$) of 130,000 and 260,000, corresponding to free-stream velocities U_{ref} of 10 and 20 m/s. Some visualizations were also performed at Reynolds numbers up to 530,000 to check Reynolds number independence. The free stream velocity U_{ref} was monitored using a pitot static tube placed at (3.9c, 2.8c, 3.0c). Visualizations were performed with the wings at equal ($\alpha_1=\alpha_2$) and different ($\alpha_1 \neq \alpha_2$) angles of attack. Angle of attack of the vortex generator, α_1, was set at either 10°, 5°, and 2.5°. The angle of attack of the blade, α_2, was set at 0°, 5°, or 10°. The lateral (z) position of the blade was also varied. Its z position relative to the vortex is denoted by the symbol z_s, where $z_s=0$ corresponds to the blade position (determined experimentally) where the streamline marking the vortex center stagnates upon its leading edge, see figure 3. z_s is positive when the vortex passes the pressure side of the blade and negative when it passes the suction side. Photographs and videos were taken at different streamwise locations through the transparent tunnel wall,

ceiling panel, and looking upstream from the diffuser. Table 1 lists all the conditions at which visualizations were performed.

Because of the volume of pictures only a representative sample are presented here. Figures 7 through 54 show the photographs grouped by vortex generator angle of attack, α_1, and then by blade-vortex spacing z_s. Many of the figures are photomosaics produced by patching together photographs measured at different streamwise locations to give a whole view of the flow. Flow direction is always from right to left or top to bottom.

Note that these pictures are not instantaneous views of the flow but are time averaged exposures; therefore, the paths followed by the bubbles appear as streaks. The vortex core is generally seen as a single bright streak generated by the lighter than air helium bubbles centrifuged there.

3.1 Vortex generator at 5° angle of attack, blade at 5° angle of attack

3.1.1 Effects of blade vortex separation z_s

Blade-vortex separations z_s were varied from +.625c to -.625c, see table 1. Figures 7 through 19 show visualizations performed at Re_c=260,000. We begin by describing figure 11 for which z_s = .063, this being more or less representative of all cases where the vortex passed on the pressure side of the blade.

The bubble stream marking the vortex core enters figure 11a on its right-hand side and passes the blade at a spanwise location approximately 0.92 chordlengths from its tip. As it passes, the core is deflected slightly inboard. Viewed from above (figure 11b), it is seen to curve around the blade much like any other streamline of the flow. The drift

inboard is a consequence of the vortex seeing its image in the blade surface. The total spanwise drift, from leading to trailing edge is about 8% chord. This phenomena is the same as that seen by Kalkhoran *et. al* (1992) and Seath and Wilson (1986). Initially, the core size appears unaffected by the interaction. However, downstream of the blade the bubble stream marking the core begins to grow at a much greater rate than it otherwise would. By the downstream end of the test section (beyond the left hand edge of figure 11a), the stream has grown to about 5 times its original diameter, presumably indicating a similar growth in the core[1]. It seems probable that this rapid growth is due to the interaction of the vortex with the blade wake. It is well known that trailing vortices embedded in turbulent shear flows diffuse much more rapidly than they otherwise would (see for example Shabaka, Mehta, and Bradshaw (1985) and Bell, Mehta, and Rabindra (1990)). It should be noted that the path of the vortex after leaving the blade is influenced to an extent by the vortex shed from the blade tip. Since the two vortices are of the same sign they tend to rotate slowly about one another. However, since they were fairly far apart (0.90c) no other significant interaction appeares to occur.

A phenomena not seen in these pictures is a small amount of low-frequency wandering of the primary vortex core. In this case the wandering had an amplitude of ±0.031c in y and ±0.047c in z measured by eye as the vortex passed the blade leading edge. Zsoldos (1992) and Devenport and Sharma (1991) saw similar vortex motions while performing experiments on vortices without blade interaction. Zsoldos concluded that

[1] Strictly speaking the increase in bubble stream diameter indicates a reduction in the strength of the pressure gradient confining the bubbles to the core, equivalent to a reduction in the core angular velocity.

these motions were due to small flow direction changes resulting from viscous effects in the contraction and diffuser of the wind tunnel.

Flow visualizations performed for values of z_s between .031c and .625c show a flow structure qualitatively identical to that described above, see figures 7 through 12. Quantitative differences are summarized in table 1 and figure 20 in terms of the spanwise drift of the vortex over the blade, the amplitude of its wandering at the blade leading edge and the divergence angle of the bubble stream marking the core downstream of the blade. Overall the spanwise drift of the vortex increases as z_s is reduced, as would be expected given the influence of its image (see table 1 and figure 20a). The rate of divergence of vortex core also increases as z_s falls, consistent with a stronger interaction between the core and the blade wake as their separation is reduced (figure 20b). At constant Reynolds number the amplitude of the wandering diminishes as the vortex is moved closer to the blade, suggesting that the proximity of the blade attenuates these motions (table 1).

Between z_s = .031 and 0 (vortex impinging on the leading edge) the form of the interaction changes. As shown in figure 13a, at z_s= 0 the vortex appears to split as it impinges on the wing leading edge. Of course, what is actually observed is a split in the bubble stream. However, bifurcation of trailing vortices is sometimes observed in the initial stages of burst, so splitting is not impossible. (A close up of the wing leading edge, figure 13b, does not show evidence of a complete burst). After the split identifiable bubble streams travel over both sides of the blade. The stream passing over the pressure side drifts inboard and the suction side drifts outboard. This is circumstantial evidence that significant proportions of the vorticity end up on opposite sides of the blade. The two

bubble streams diffuse rapidly downstream of the trailing edge, but can be distinguished for several chordlengths. Within this distance they rotate about each other - further suggesting that they are distinct vortical structures and not just preferred bubble paths. As illustrated in figure 20b the rate of divergence of the core bubbles downstream of the blade was greater than for any other z_s value. In terms of vortex wandering this flow was relatively stable the amplitudes being less than ±0.024c in y and ±0.031c in z respectively at the blade leading edge.

The flow pattern with the vortex passing on the suction side of the blade (figures 14 through 19, z_s = -.031 to -.625) is in many ways similar to that produced with the vortex passing the pressure side. Figure 15, for which z_s =-0.063, is a typical example. The vortex again passes the leading edge of the blade about 0.91c from its tip. This time it drifts outboard in response to its image, the total drift (9%c) being very similar in magnitude to that seen in figure 13. Downstream of the blade the bubble stream marking the core grows at about the same rate as in the equivalent pressure-side case. Again we suspect that this is due to injestion of the blade wake by the vortex. Wandering in this case was slightly less than for z_s = +.063 at ±.024 in y and ±.031 in z.

Flow visualizations performed for values of z_s between -.031c and -.625c show a flow structure qualitatively identical to that described immediately above, see figures 14 through 19. Quantitative differences are again summarized in table 1 and figure 20. As on the pressure side, the spanwise drift of the vortex over the blade, the amplitude of its wandering at the blade leading edge and the divergence angle of the bubble stream marking the core downstream of the blade all increase as the magnitude of z_s is reduced.

3.1.2 Effects of Reynolds Number

Video tapes and direct observations of the above configurations showed no significant qualitative or quantitative changes in flow structure with increase in Reynolds number up to Re_c = 530,000 except, perhaps, for some decrease in the amplitude of the wandering motions. A significant change was observed however with reduction in Reynolds number to 130,000. Figures 21, 22 and 23 show visualizations performed at this Reynolds number for z_s = 0.125, 0 and -0.125. With the vortex passing to the suction or pressure sides of the blade the flow structure is essentially the same as that described above (figures 21 and 23) with the exception that the vortex wandering motions were of significantly greater amplitude. For z_s=0, however, a new unsteady flow structure is seen (figures 22a and b). The vortex moves from the pressure to the suction side of the blade and back again in an irregular wandering motion with a period of about 10 seconds. The amplitude of these wandering motions is substantially larger than in other cases (±.094c in y and ±0.125c in z). When the vortex impinges on the leading edge it splits evenly as at the higher Reynolds number. It is possible that this behavior is caused by the fact that the boundary-layer trip on the blade is not fully effective at this low speed. Devenport et al. (1992) show the blade boundary layer to be fully turbulent only for Re_c= 260,000 and greater. With a less well developed boundary layer the vortex is more likely to induce separation from the blade surface. Separation would produce large scale unsteadiness perhaps with the effects observed here.

3.1.3 Effects of Vortex Generator Tip Geometry

To investigate the effects of the tip geometry of the vortex-generating wing, a rounded tip was attached. The tip was built from wood and added a half body of rotation, with a NACA 0012 section, to the otherwise blunt tip. Visualizations performed at Re_c=260,000, for three representative vortex-blade separations (z_s = .063, 0 and -.063) and are presented in figures 24, 25 and 26. Accounting for differences in the contrast of the photographs (produced by ageing of the arc lamp during the test) these flows appear almost identical to their counterparts produced with the blunt tip (figures 11, 13 and 15). The only differences are in the spanwise location at which the vortex passes the blade (0.75c compared to 0.9c from the tip) and in the amplitude of the vortex wandering motions (these being significantly larger for z_s = 0.5, see table 1). The change in spanwise location is simply a result of the tip of the vortex generating wing being about 0.16c lower with the rounded tip than without. The increase in wandering motion may indicate that the rounded tip is less effective at anchoring the origin of the vortex.

3.1.4 Effects of the Boundary Layer Trips

Three cases (z_s = .063, 0 and -.063) were studied at a Reynolds number of 260,000 with the trips removed from the blade (figures 27, 28 and 29) and with the trips removed from both blade and vortex generator (figures 30,31, and 32). Some of these photographs are of poor quality due to deterioration of the light source. However, upon close examination of the originals (confirmed by the video tapes and observations by eye) they show the same qualitative flow structure seen with both trips in place. Table 1 reveals some small quantitative differences. The spanwise drift of the vortex as it passes the blade

appears larger with the blade trip removed (by .02 to .05c). This may be because the trip and resulting thicker boundary layer deflect the streamlines and therefore the vortex a little further from the blade surface, decreasing the influence of the image. The divergence angle of the bubble streaks marking the core downstream of the blade also appears to have been affected. However, with the poor quality of the photographs in these cases the uncertainty in this measurement is very large, so this may not be a significant difference. Finally, the amplitude of the vortex wandering motions was clearly increased by removal of the trips. This is consistent with the above argument that a less well developed boundary layer on the blade is more prone to separation in the presence of the vortex, resulting in a more unstable flow.

3.2 Vortex generator at 10° angle of attack, blade at 10° angle of attack.

3.2.1 Effects of blade vortex separation z_s

Blade-vortex separations z_s were varied from +.125c to -.125c, see table 1. To show the effects of z_s we present the photographs taken at Re_c = 130,000 since these are clearer than those taken at Re_c = 260,000 and there were no significant qualitative changes in flow structure occured between these two Reynolds numbers. Visualizations for Re_c = 130,000 are presented in figures 33 through 38.

With the vortex passing to the pressure side of the blade at z_s = 0.125c and 0.063c (figures 33 and 34), it crosses the blade leading edge at a spanwise location 0.84 chordlengths from its tip and then drifts inboard under the action of its image. The total movement, from leading to trailing edge, is 7%c and 9%c respectively for z_s = 0.125c and

0.063c. As with both wings at 5° angle of attack, the core appears initially to be unaffected by the interaction. Downstream of the blade, however, the bubble stream marking the core begins to diverge, presumably indicating a rapid growth of the core as it interacts with the blade wake. The core also appears to be deflected downwards under the influence of the blade tip vortex, this influence being stronger than at 5°. Wandering motions (table 1) are on the whole slightly smaller than at 5° but, as before, decreased with reduction in z_s.

Between z_s = 0.063c and 0.031c a distinct change in flow structure is seen. For z_s = 0.031c (figure 35) the vortex core appears to undergo an abrupt increase in cross section as it meets the strong adverse pressure gradient upstream of the blade. The bubble streaks marking the core initially fan out, but are then brought back together as the favourable pressure gradient between the leading edge and maximum thickness is encountered (see especially figures 35b, c and d). This re-assembled vortex core, having a diameter roughly twice that of the original vortex, appears to be fairly unstable since the bubble streaks show it diffusing rapidly downstream once it reaches the trailing edge. Careful observations by eye did not show any evidence of instantaneous flow reversals in the region of rapid core growth near the blade leading edge. The flow pattern here appeared similar to that commonly referred to as a 'spiral' burst.

Between z_s = .031 and 0 a further change in structure is seen (figure 36). At z_s=0 the burst occurs directly (0.12c) upstream of the leading edge and the vortex does not re-form (figure 36b). A close up of the burst region (figure 36c) shows it to be fairly axisymmetric. Videotapes clearly show the instantaneous reversal of the flow within this

region. Overall the flow pattern appears similar to that commonly referred to as a 'bubble' burst. The burst destroys all semblance of coherent flow structure in the vortex over the wing and in the wake. In the wake bubble streaks marking the remains of the vortex form a band approximately twenty times wider than that marking the incoming vortex core.

With the vortex passing on the suction side of the blade, the flow structure changes once more. Figure 37 shows the visualizations for z_s = -.063. The most notable feature in this figure is the widening of the bubble stream which begins immediately upon the vortex encountering the wing (presumably as a result of the adverse pressure gradient here). This does not appear to be a burst since it is a relatively gradual process which continues downstream of the trailing edge. For z_s=-0.125 (figure 38) the flow appears similar except that the widening of the bubble stream does not start until the vortex core passes the mid-chord of the blade.

3.2.2 Effects of Reynolds Number

Figures 39 through 45 show visualizations performed at Re_c = 260,000 over the same range of z_s positions. Although it is not as clear in the photographs, these flows did exhibit the same qualitative flow structure seen in their counterparts at Re_c = 130,000, including the spiral and bubble bursts. As shown in table 1 vortex wandering motions decreased somewhat between Re_c = 130,000 and 260,000. Video tapes and direct observations showed this trend continuing further up to Re_c = 530,000.

3.3 Other angle of attack combinations.

Flow visualizations were performed at Re_c = 260,000 for four different angle of attack combinations; α_1=5° and α_2=0, α_1=10° and α_2=5°, α_1=10° and α_2=0, α_1 = 2.5° and α_2 = 5°, where α_1 is the angle of attack of the vortex generator and α_2 the blade angle of attack. Although a complete range of blade vortex separations (z_s) were examined by eye in each case only a proportion of these visualizations produced useful photographs. These pictures are presented in figures 46 through 54.

Setting the wings at different angles of attack produced no phenomena not already described. As a general rule the form of the interaction appeared to be governed by the strength of the vortex and the blade angle of attack. For example, we observed by eye bursting of the vortex upstream of the blade for both α_1=10°, α_2=5° (figure 48b) and α_1=10°, α_2=0, though the size of the burst region did decrease substantially with α_2. Bursting was not observed for α_1=5°, α_2=0. Some quantitative measures of these flows are included in table 1.

4. CONCLUSIONS AND FUTURE WORK

Helium bubble flow visualizations have been performed to study the perpendicular interaction of a turbulent trailing vortex and a rectangular wing in the Virginia Tech Stability Tunnel. Many combinations of vortex strength, vortex-blade separation (z_s) and blade angle of attack were studied.

A range of phenomena were observed. For z_s greater than a few percent chord the vortex is deflected as it passes the blade under the influence of the local streamline curvature and its image in the blade. Initially the interaction appears to have no influence on the core. Downstream, however, the vortex core begins to diffuse and grow presumably as a consequence of its interaction with the blade wake. The magnitude of these effects increases with reduction in z_s. For z_s near zero the form of the interaction changes and becomes dependent on the vortex strength. For lower strengths the vortex appears to split into two filaments on the leading edge of the blade, one passing on the pressure and one passing on the suction side. At higher strengths the vortex bursts in the vicinity of the leading edge. In either case the core or its remnants then rapidly diffuse with distance downstream. Increase in Reynolds number does not qualitatively affect the flows apart from decreasing the amplitude of the small low-frequency wandering motions of the vortex. Changes in wing tip geometry and boundary layer trip had very little effect.

Future work will involve detailed velocity measurements in the flow downstream of the blade. The following cases have been selected for further study based on the the above visualizations and their relevance to helicopter applications;

a) $\alpha_1=\alpha_2=5°$, $z_s=0.125c$, and $Re_c=260,000$

b) $\alpha_1=\alpha_2=5°$, $z_s=0.063c$, and $Re_c=260,000$

c) $\alpha_1=\alpha_2=5°$, $z_s=0.0c$, and $Re_c=260,000$

d) $\alpha_1=\alpha_2=5°$, $z_s=-0.063c$, and $Re_c=260,000$

e) $\alpha_1=\alpha_2=5°$, $z_s=-0.125c$, and $Re_c=260,000$.

The authors would like to thank NASA Langley, in particular Tom Brooks and Mike Marcolini for their support under grant NAG-1-1119 and Stewart Glegg, of Florida Atlantic University, for his cooperation on this work. The help of Lee Fuglestad and Chris Shively in performing the visualizations is also gratefully acknowledged.

5. REFERENCES

Bell, J. H.; Mehta, R. D.; and Rabindra, D., "Interaction of a Streamwise Vortex with a Turbulent Mixing Layer.", Physics of Fluids, vol. 2, pp. 2011-2023, 1990.

Brooks, T. F. and Martin, R. M., "Results of the 1986 NASA/FAA/DFVLR Main Rotor Test Entry in the German-Dutch Wind Tunnel (DNW)", NASA TM 100507, 1987.

Brooks, T. F.; Marcolini, M. A.; and Pope, D. A., "Main Rotor Noise Study in the DNW", presented to the AMS Specialist Meeting on Aerodynamics and Aeroacoustics, Arlington, Texas, 1987.

Choi, K. and Simpson, R. L., "Some Mean-Velocity, Turbulence, and Unsteadiness Characteristics of the VPI&SU Stability Wind Tunnel", Report VPI-AOE-161, VPI&SU, Blacksburg, VA, 1987.

Devenport, W. J.; Glegg, A. L.; and Sharma, G.; "Turbulence Measurements in Trailing Vortices for B.W.I. Noise Prediction", Report to NASA Langley under grant NAG-1-1119, June 1992.

Devenport, W. J. and Sharma, G., "Far-Field Turbulence Structure of the Tip Vortex Shed by a Single Rectangular Wing", Eighth Symposium on Turbulent Shear Flows, 1991.

Glegg, S., "The Prediction of Blade Wake Interaction Noise Based on a Turbulent Vortex Model", AIAA 12th Aeroacoustics Conference, AIAA paper 89-1134, San Antonio, TX, April 10-12, 1989.

Glegg, S. A. L. and Devenport, W.J., "The application of experimental data to blade wake interaction noise prediction", Sixth International Symposium on Unsteady Aerodynamics, Aeroacoustics and Aeroelasticity of Turbomachines and Propellers, University of Notre Dame, IN, September 15-19, 1991.

Kalkhoran, I. M.; Wilson, D. R.; and Seath, D. D.; "Experimental Investigation of the Perpendicular Rotor Blade-Vortex Interaction at Transonic Speeds", AIAA Journal, vol. 30, No. 3, pp. 747-755, March 1992.

Mason, W. H. and Marchman, J. F., "Farfield Structure aof an Aircraft Trailing Vortex, Including Effects of Mass Injection", NASA contractor report CR-62078, April 1972.

Phillipe, J. J. and Armand, C., "ONERA Aerodynamic Research on Helicopters", Rotorcraft Design, AGARD CP-223, Jan. 1978.

Seath, D. D. and Wilson, D. R.,"Vortex-Airfoil Interaction Tests", AiAA 24th Aerospace Sciences Meeting, AIAA Paper 86-0354, Reno, NV, Jan. 6-9, 1986.

Schlinker, R. H. and Amiet, R. K., "Rotor-Vortex Interaction Noise", AIAA Eighth Aeroacoustics Conference, AIAA Paper 83-0720, Atlanta, GA, April 11-13, 1983.

Shabaka, I. M. M. A.; Mehta, R. D.; and Bradshaw, P., "Longitudinal Vortices Embedded in Turbulent Boundary Layers. Part 1. Single Vortex.", Journal of Fluid Mechanics, vol. 155, p. 37, 1985.

Zsoldos, J. S., "An Experimental Investigation of Interacting Wing-Tip Vortex Pairs", MS Thesis, VPI&SU, June 1992.

TABLES

α_1,α_2	Re×10^5	z_v/c	Fig#	1	2	3	4
5°,5°	2.6	0.625	7	0.063	0.047	0.02	0.14
		0.313	8	0.063	0.031	0.02	0.27
		0.188	9	0.031	0.031	0.02	0.23
		0.125	10	0.031	0.031	0.05	0.23
		0.063	11	0.031	0.047	0.08	1.50
		0.031	12	0.023	0.031	0.10	1.04
		0.0	13	0.016	0.031	-	3.15
		-0.031	14	0.031	0.031	-0.07	3.09
		-0.063	15	0.023	0.031	-0.09	0.81
		-0.125	16	0.031	0.031	-0.05	0.41
		-0.188	17	0.031	0.031	-0.02	0.28
		-0.313	18	0.023	0.031	-0.02	0.27
		-0.625	19	0.047	0.094	-0.01	0.14
	1.3	0.125	21	0.047	0.031	0.07	0.48
		0.0	22	0.125	0.094	-	3.14
		-0.125	23	0.094	0.094	-0.06	0.79
5°$^+$,5°	2.6	0.063	24	0.063	0.047	0.10	0.35
		0.0	25	0.031	-	-	3.50
		-0.063	26	0.016	0.016	-0.09	1.00
5°,5°*		0.063	27	0.031	0.031	0.11	0.40
		0.0	28	0.047	0.063	-	3.00
		-0.063	29	0.031	-	-	0.67
5°*,5°*		0.063	30	0.063	0.032	0.13	0.82
		0.0	31	0.063	-	-	2.88
		-0.063	32	0.031	0.031	-	0.67

Table 1: Table of flow properties compiled from flow visualization mozaics. (1) amplitude of core wandering in y direction (chords) (2) amplitude of core wandering in z direction (chords) (3) total spanwise drift of vortex between leading and trailing edges of blade (chords) (4) Divergence angle of bubble stream marking vortex core after encountering blade (degrees). Note $^+$ indicates rounded wing tip and * indicates no trip.

α_1,α_2	$Re\times10^5$	z/c	Fig#	1	2	3	4
10°,10°	1.3	0.125	33	0.031	0.063	0.07	-
		0.063	34	0.063	0.063	0.09	0.80
		0.031	35	-	-	0.15	3.94
		0.0	36	0.016	0.042	-	8.16
		-0.063	37	0.094	-	-	7.62
		-0.125	38	0.094	≈0.0	-	6.34
	2.6	0.125	39	0.016	0.016	0.08	0.62
		0.063	40	≈0.0	0.031	0.14	0.68
		0.031	41	0.016	≈0.0	0.07	1.80
		0.0	42	0.031	≈0.0	-	-
		-0.031	43	≈0.0	-	-	-
		-0.063	44	-	-	-0.08	0.45
		-0.125	45	0.016	0.016	-	-
5°,0°		0.063	46	0.063	0.047	0.12	1.28
		0.0	47	0.031	-	-	1.73
10°,5°		0.063	48	≈0.0	0.031	0.16	1.00
		0.0	49	0.016	0.031	-	3.55
		-0.063	50	0.031	0.047	-	0.96
10°,0°		0.063	51	0.047	0.031	0.18	-
2.5°,5°		0.063	52	0.047	0.031	0.05	0.32
		0.0	53	≈0.0	0.031	-	4.13
		-0.063	54	-	-	-0.05	0.62

Table 1: Table of flow properties compiled from flow visualization mozaics. (1) amplitude of core wandering in y direction (chords) (2) amplitude of core wandering in z direction (chords) (3) total spanwise drift of vortex between leading and trailing edges of blade (chords) (4) Divergence angle of bubble stream marking vortex core after encountering blade (degrees). Note $^+$ indicates rounded wing tip and * indicates no trip.

FIGURES

b perpendicular

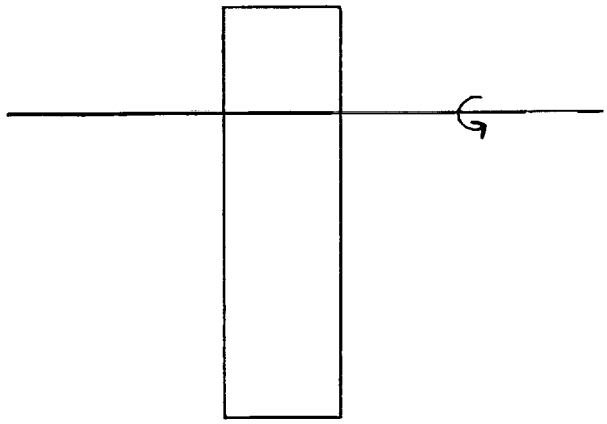

a parallel

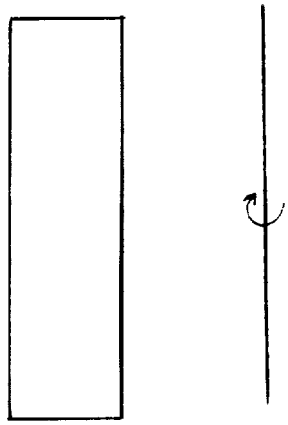

Figure 1: Two types of blade vortex interactions.

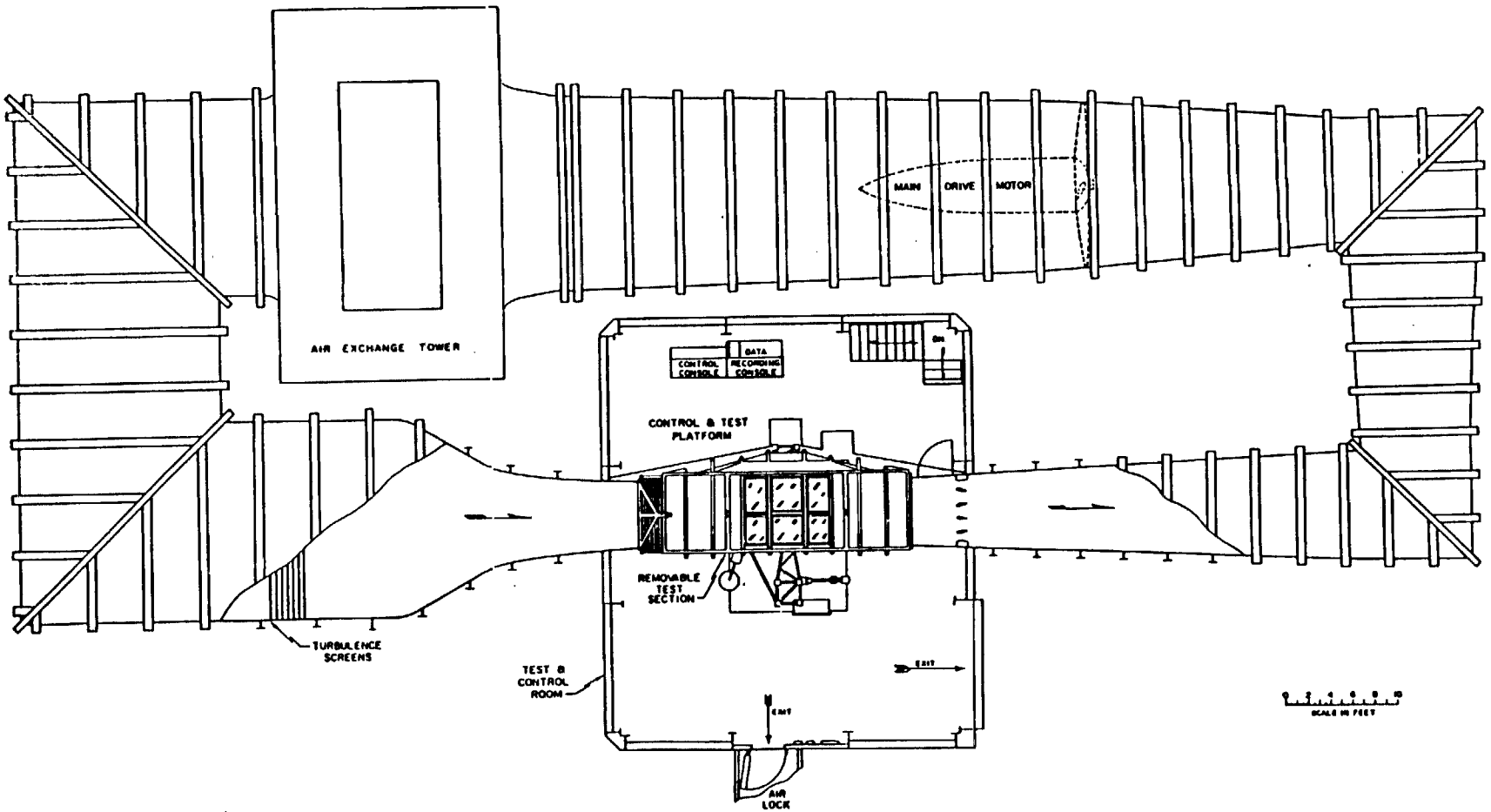

Figure 2: Schematic of the Virginia Tech Stability Wind Tunnel.

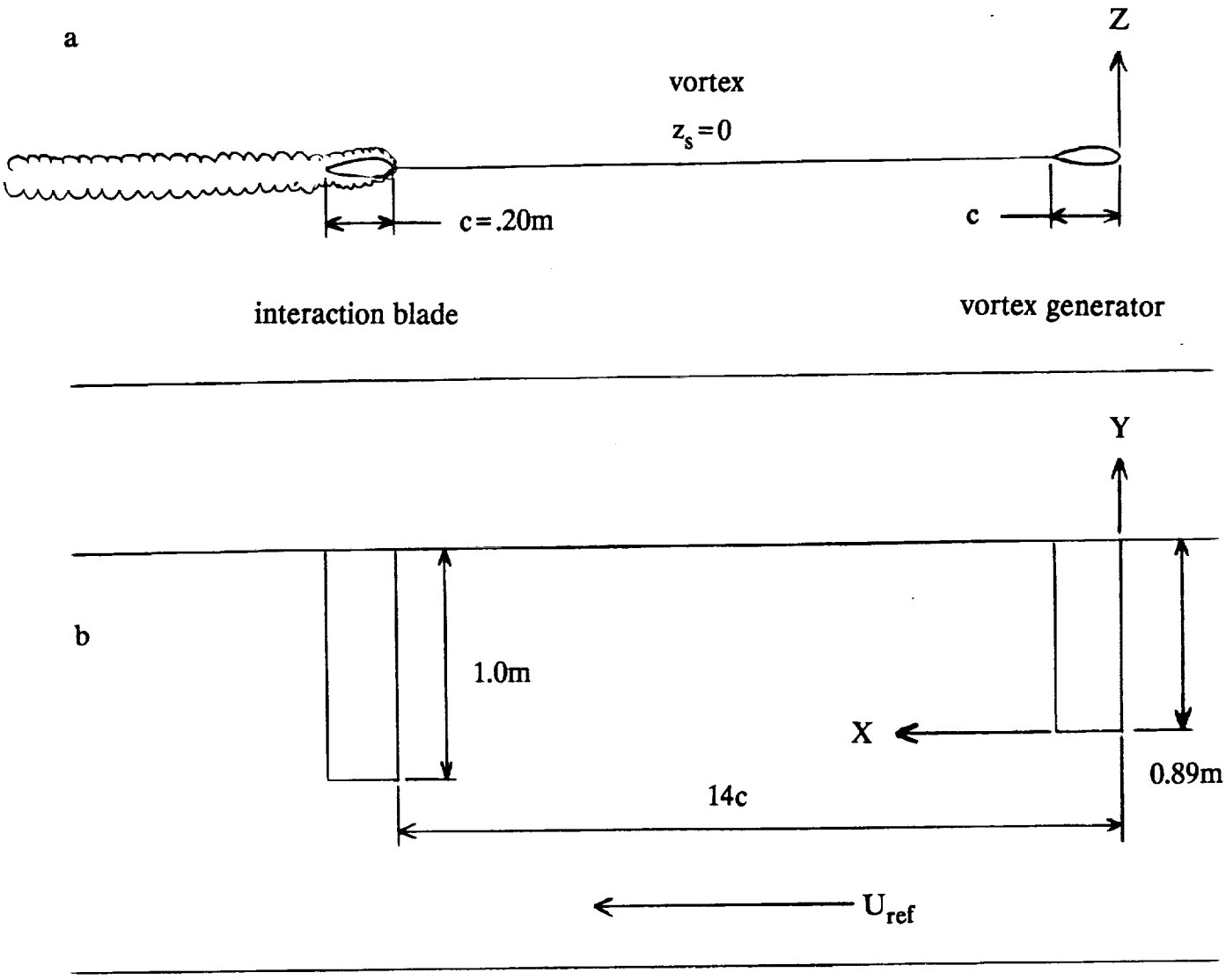

Figure 3: Schematic of the test section showing experimental set up and tunnel coordinate system. a) top view b) side view

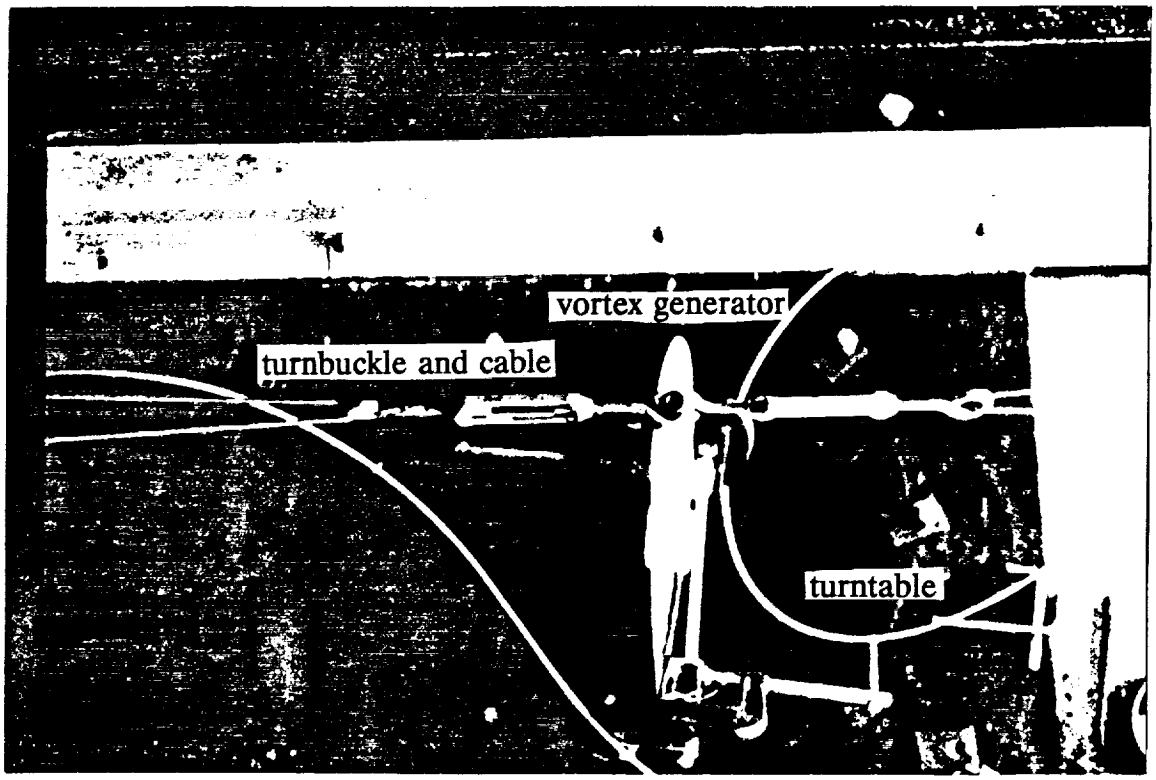

Figure 4: Top view of forward wing mount.

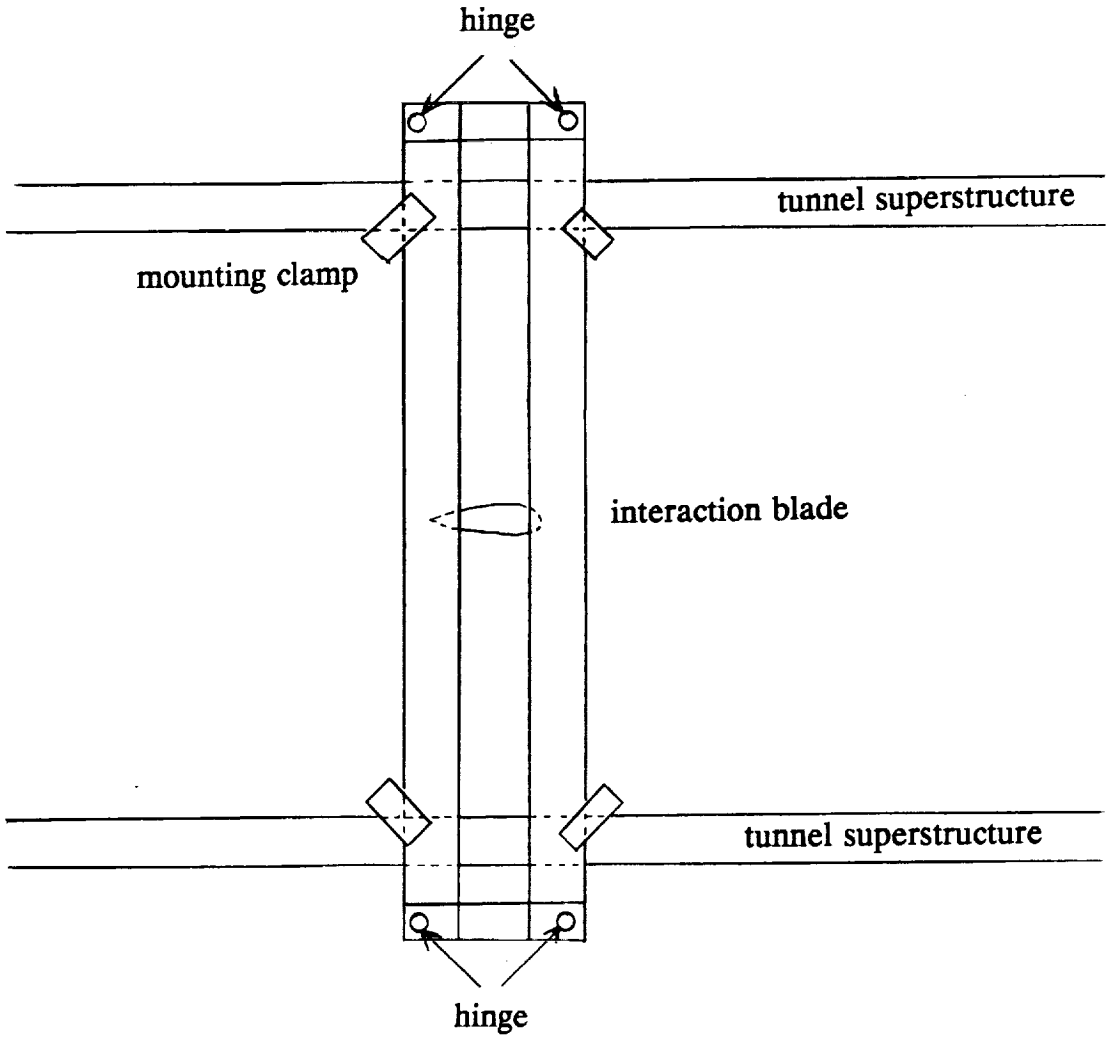

Figure 5: Schmatic top view of interaction blade mount.

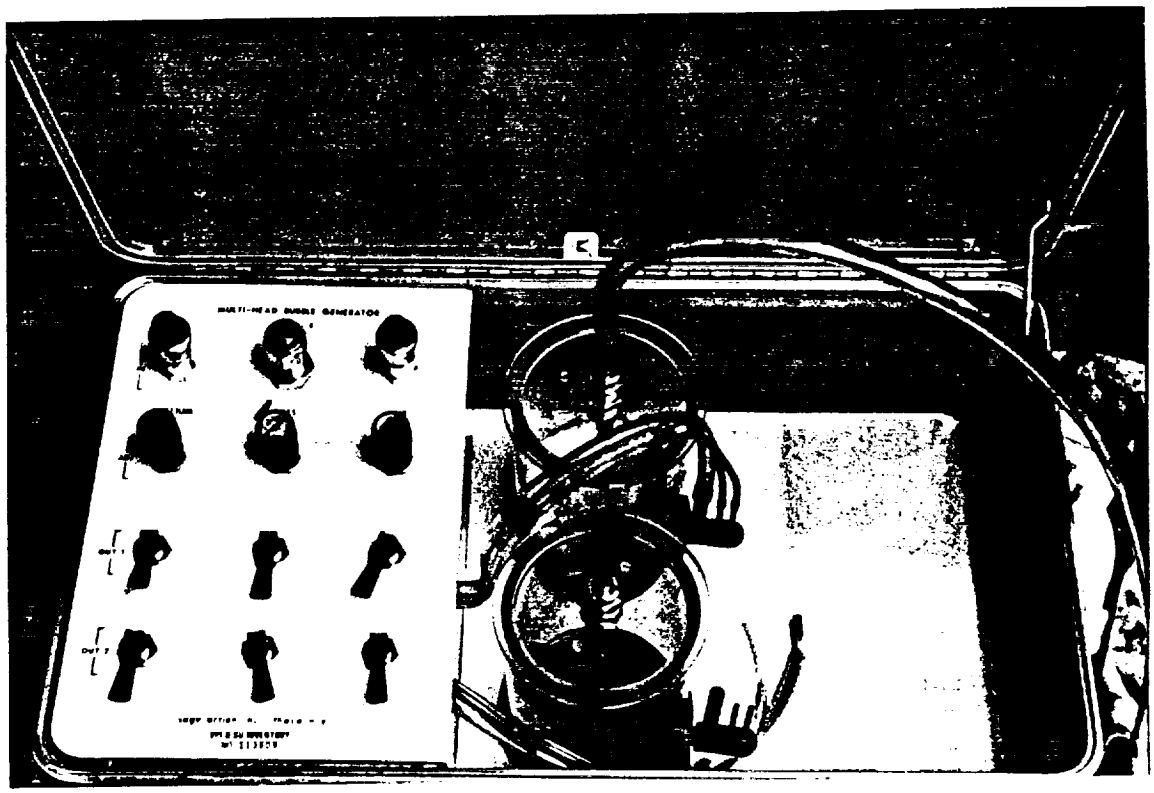

Figure 6: Top view of Sage Action helium bubble generator. Mixture adjustments are on the left of the case with "vortex" filters and "plug in" heads located on the right side of the case.

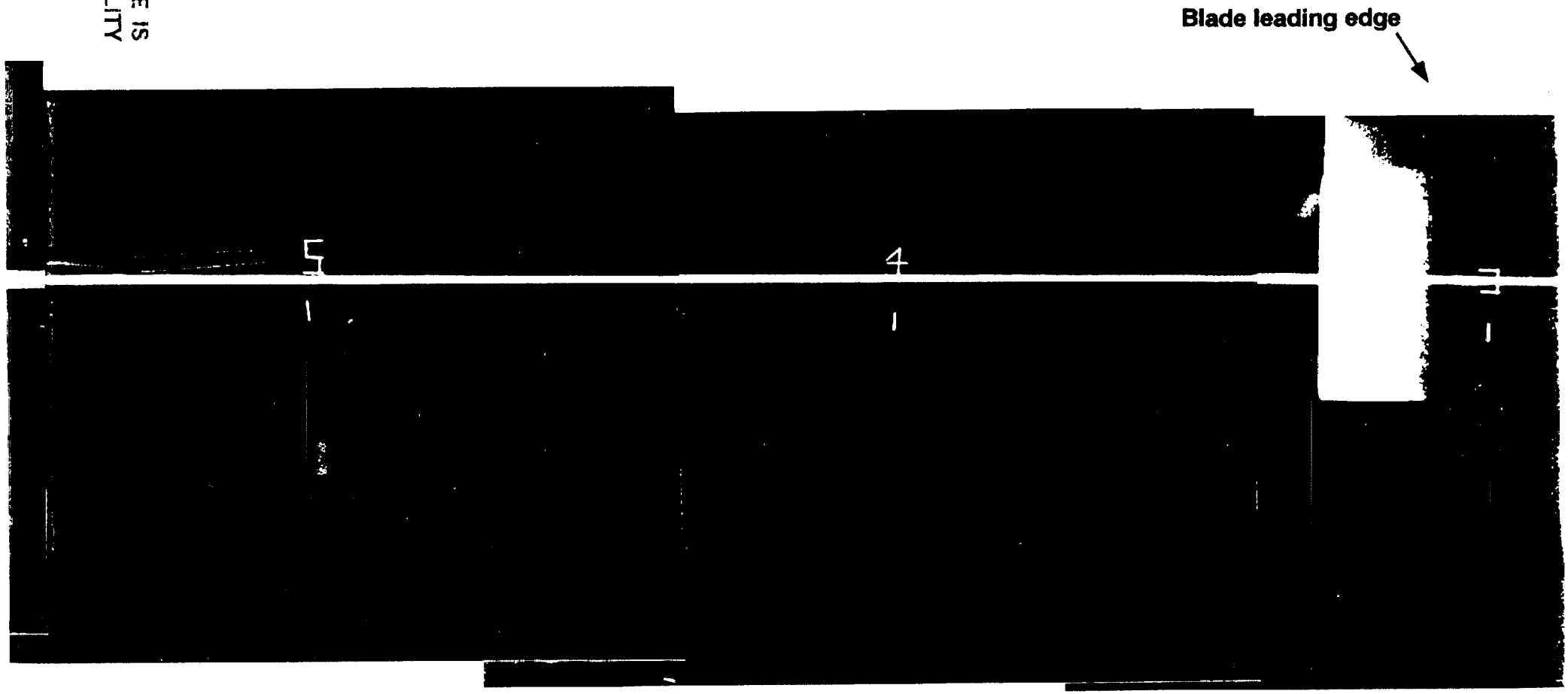

Figure 7. Flow visualization for $z_s = .625$, $Re_c = 260{,}000$, $\alpha_1 = \alpha_2 = 5°$. Side view.

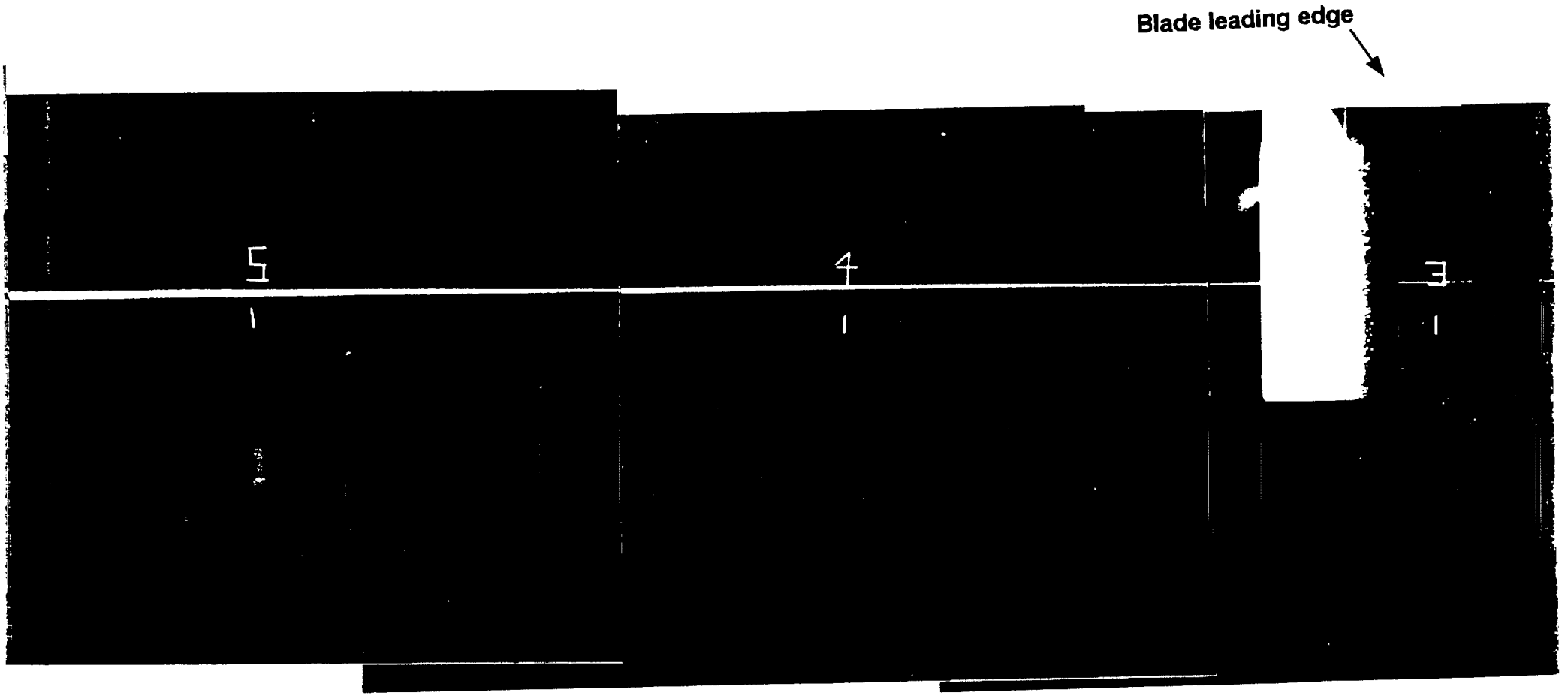

Figure 8. Flow visualization for z_s = .313, Re_c = 260,000, $\alpha_1 = \alpha_2 = 5°$. Side view.

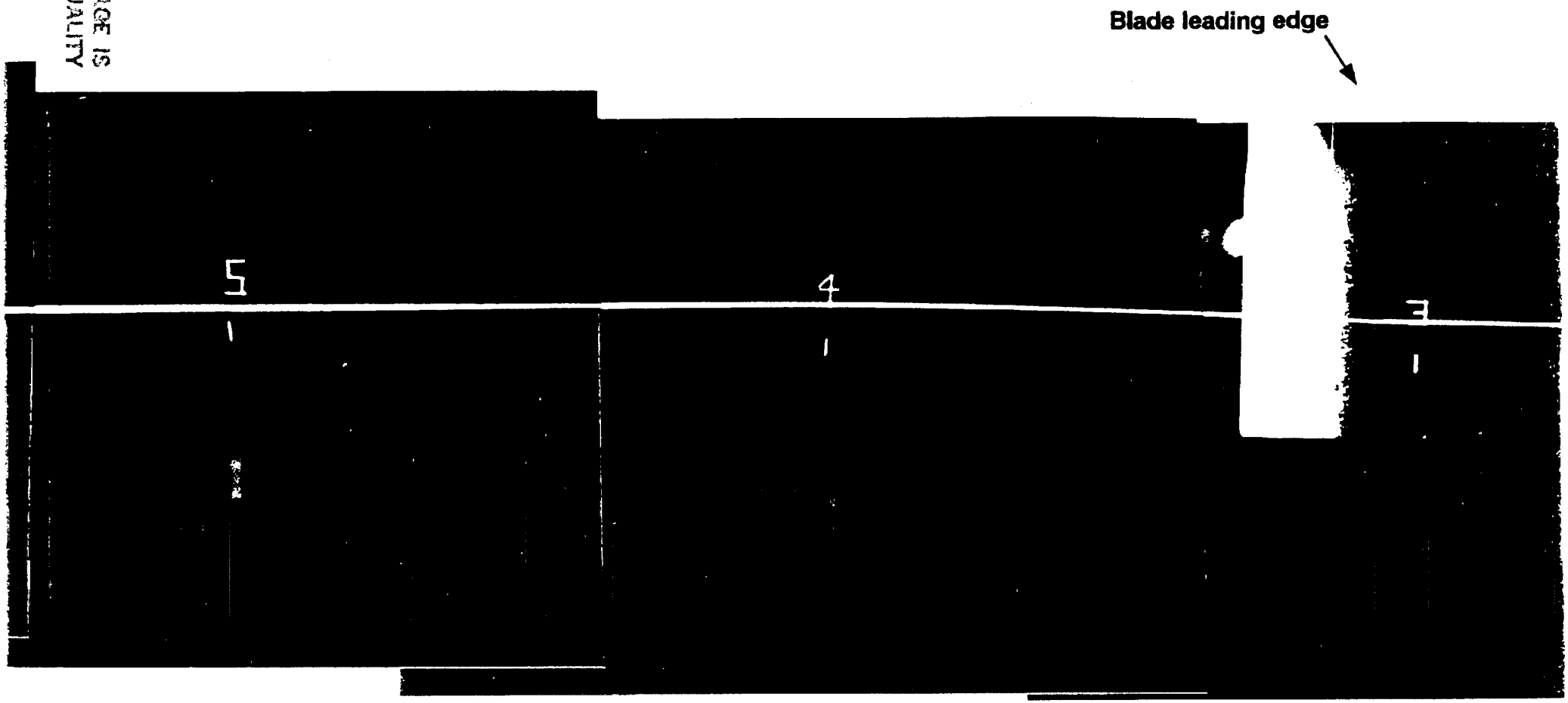

Figure 9. Flow visualization for z_s = .188, Re_c = 260,000, $\alpha_1 = \alpha_2 = 5°$. Side view.

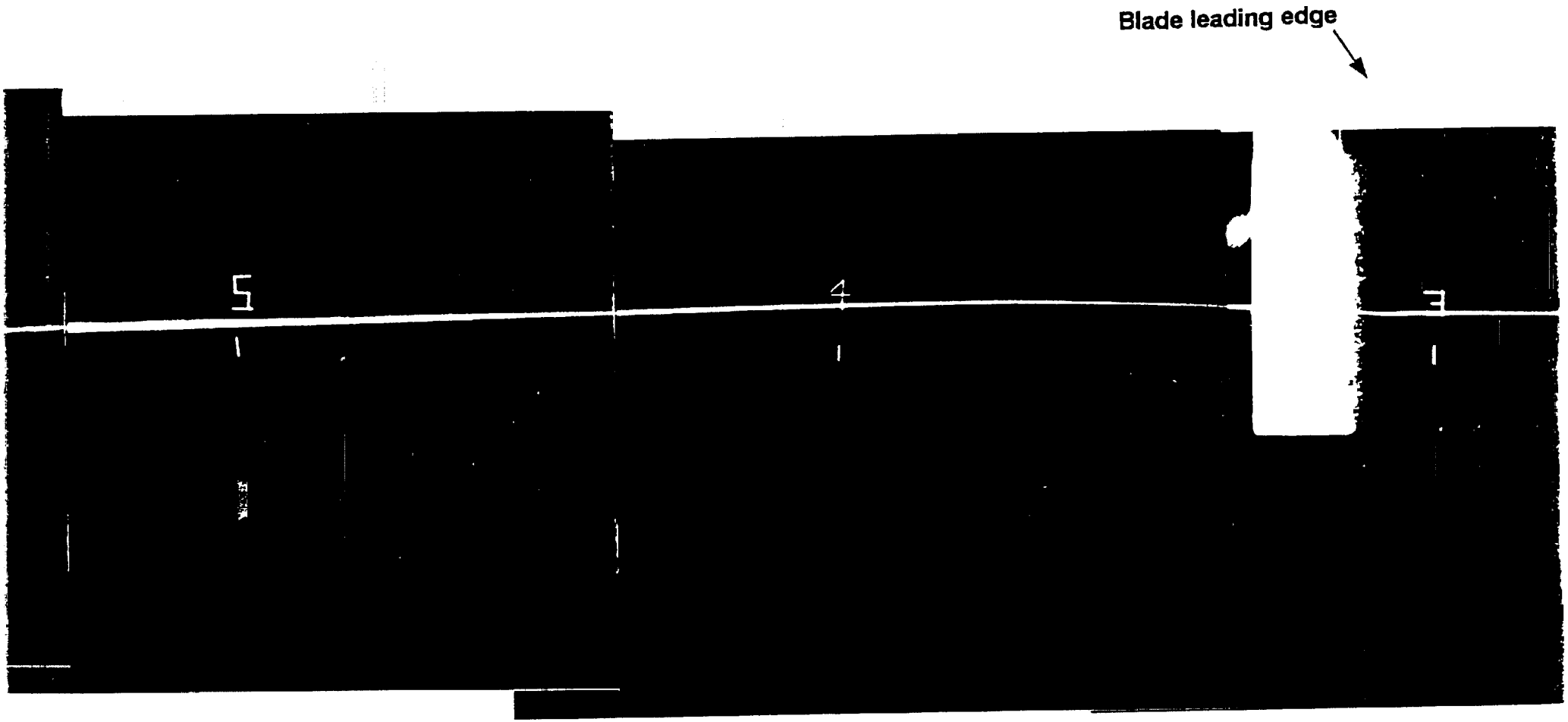

Figure 10. Flow visualization for z_s = .125, Re_c = 260,000, $\alpha_1 = \alpha_2 = 5°$. Side view.

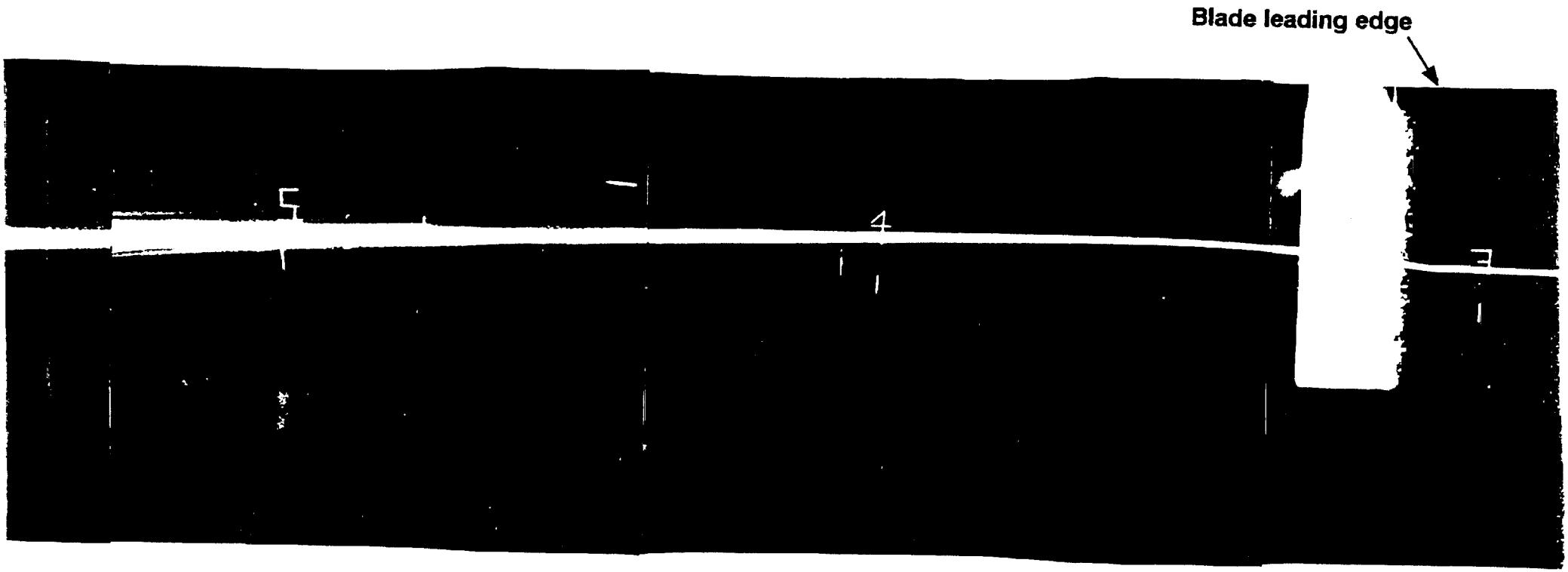

(a)

Figure 11. Flow visualization for z_s = .063, Re_c = 260,000, $\alpha_1 = \alpha_2 = 5°$. (a) Side view. (b) View from blade root.

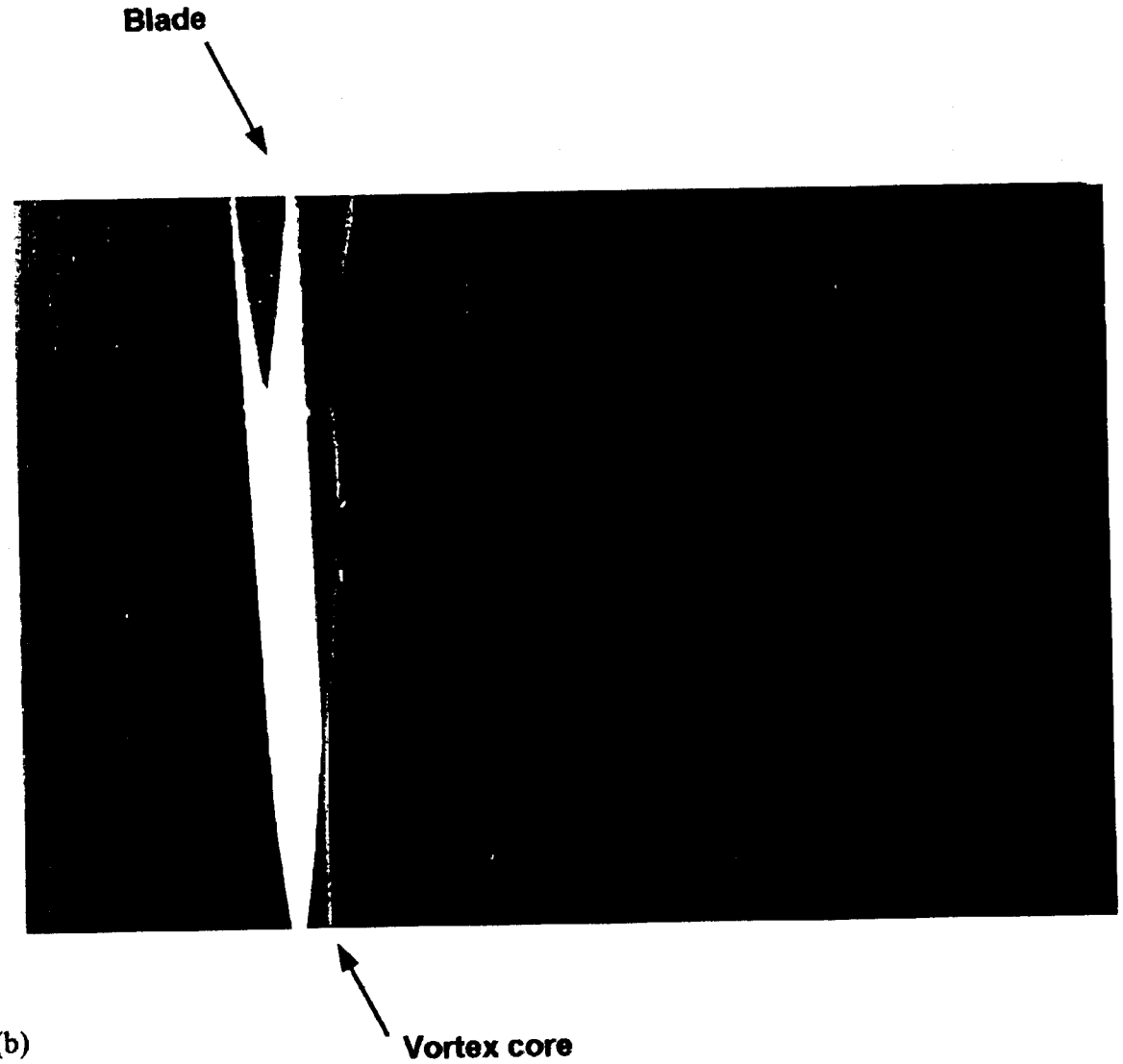

Figure 11. Flow visualization for z_s = .063, Re_c = 260,000, $\alpha_1 = \alpha_2 = 5°$. (a) Side view. (b) View from blade root.

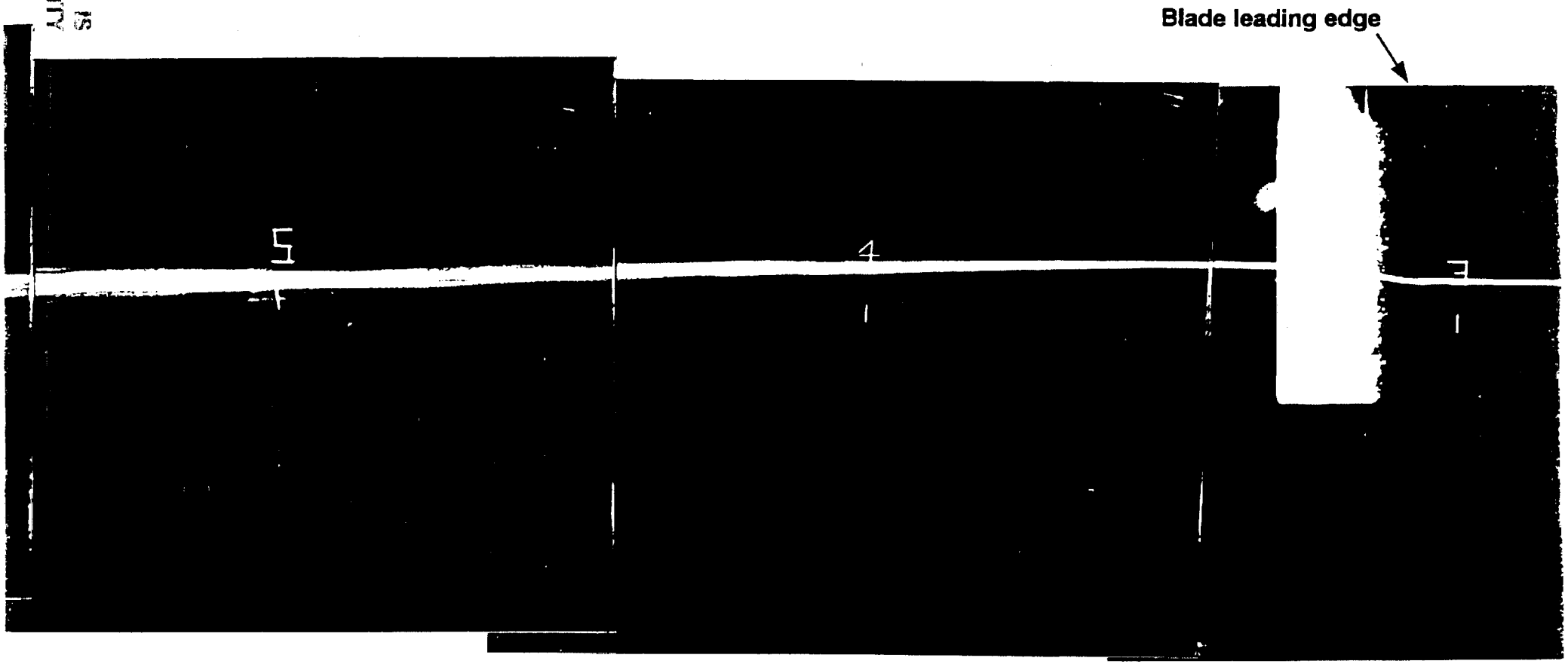

Figure 12. Flow visualization for z_s = .031, Re_c = 260,000, $\alpha_1 = \alpha_2 = 5°$. Side view.

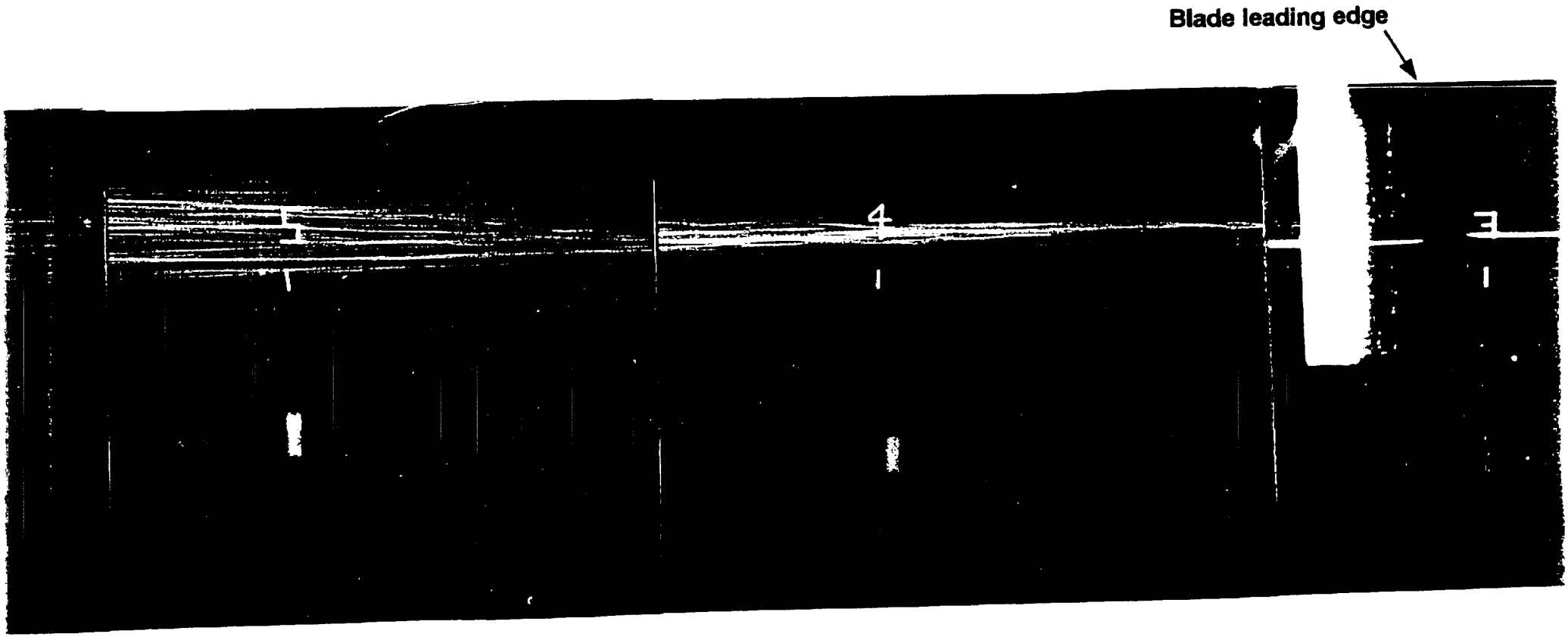

(a)

Figure 13. Flow visualization for z_s = .0, Re_c = 260,000, $\alpha_1 = \alpha_2 = 5°$. (a) Side view. (b) Close up of blade leading edge.

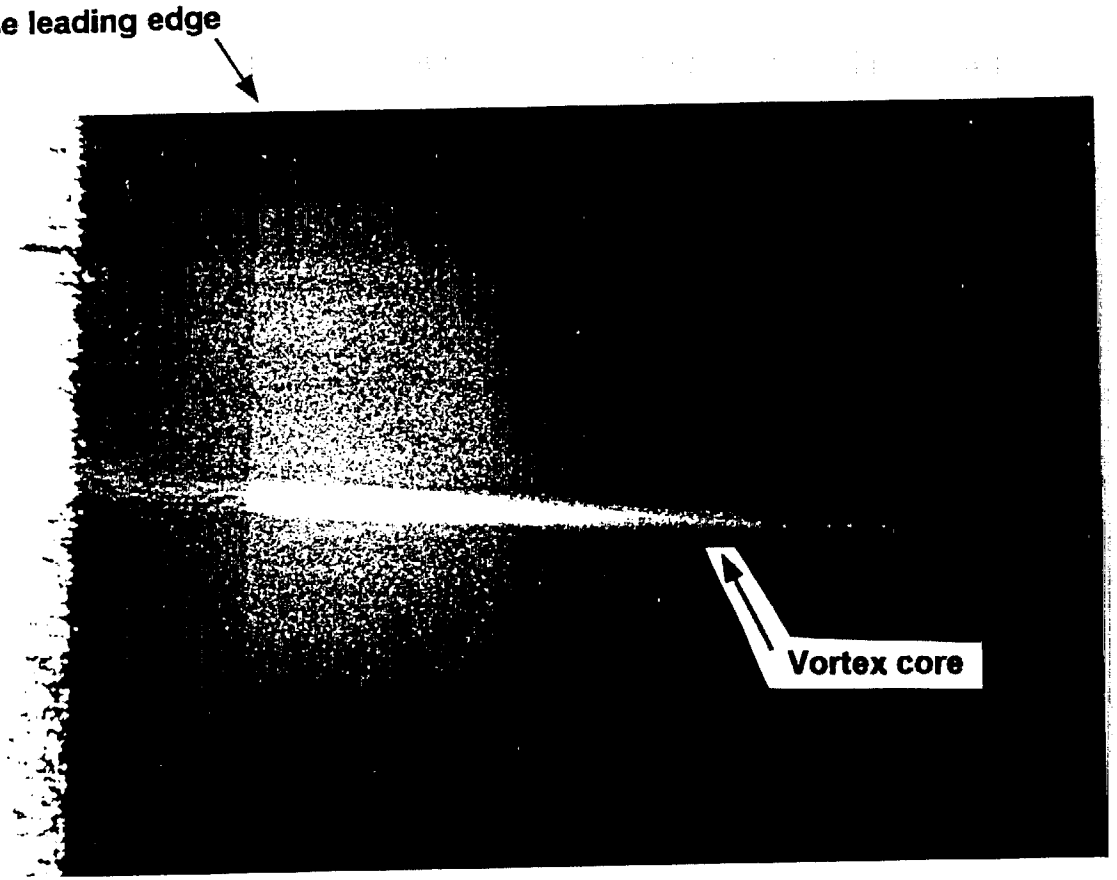

(b)

Figure 13. Flow visualization for z_s = .0, Re_c = 260,000, $\alpha_1 = \alpha_2 = 5°$. (a) Side view. (b) Close up of blade leading edge.

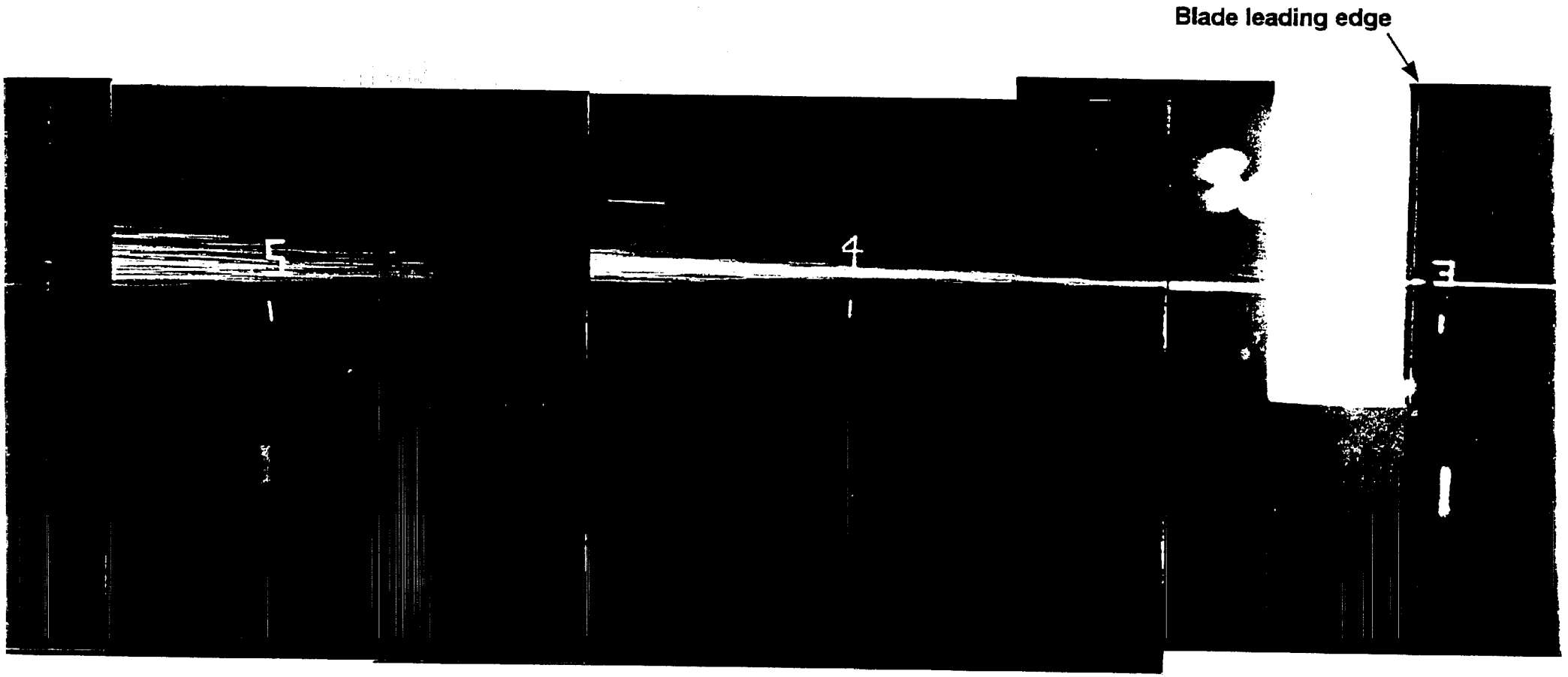

Figure 14. Flow visualization for z_s = -.031, Re_c = 260,000, $\alpha_1 = \alpha_2 = 5°$. Side view.

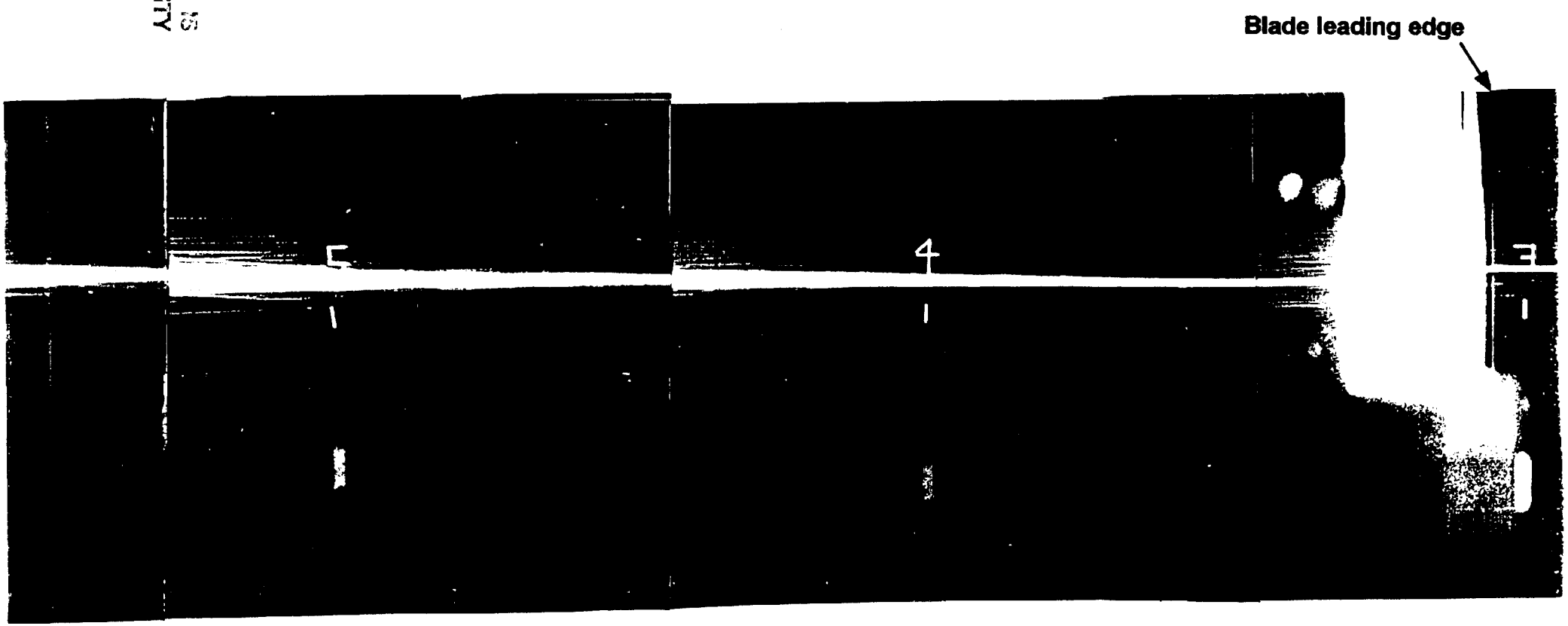

(a)

Figure 15. Flow visualization for z_s = -.063, Re_c = 260,000, $\alpha_1 = \alpha_2 = 5°$. (a) Side view. (b) View from blade root.

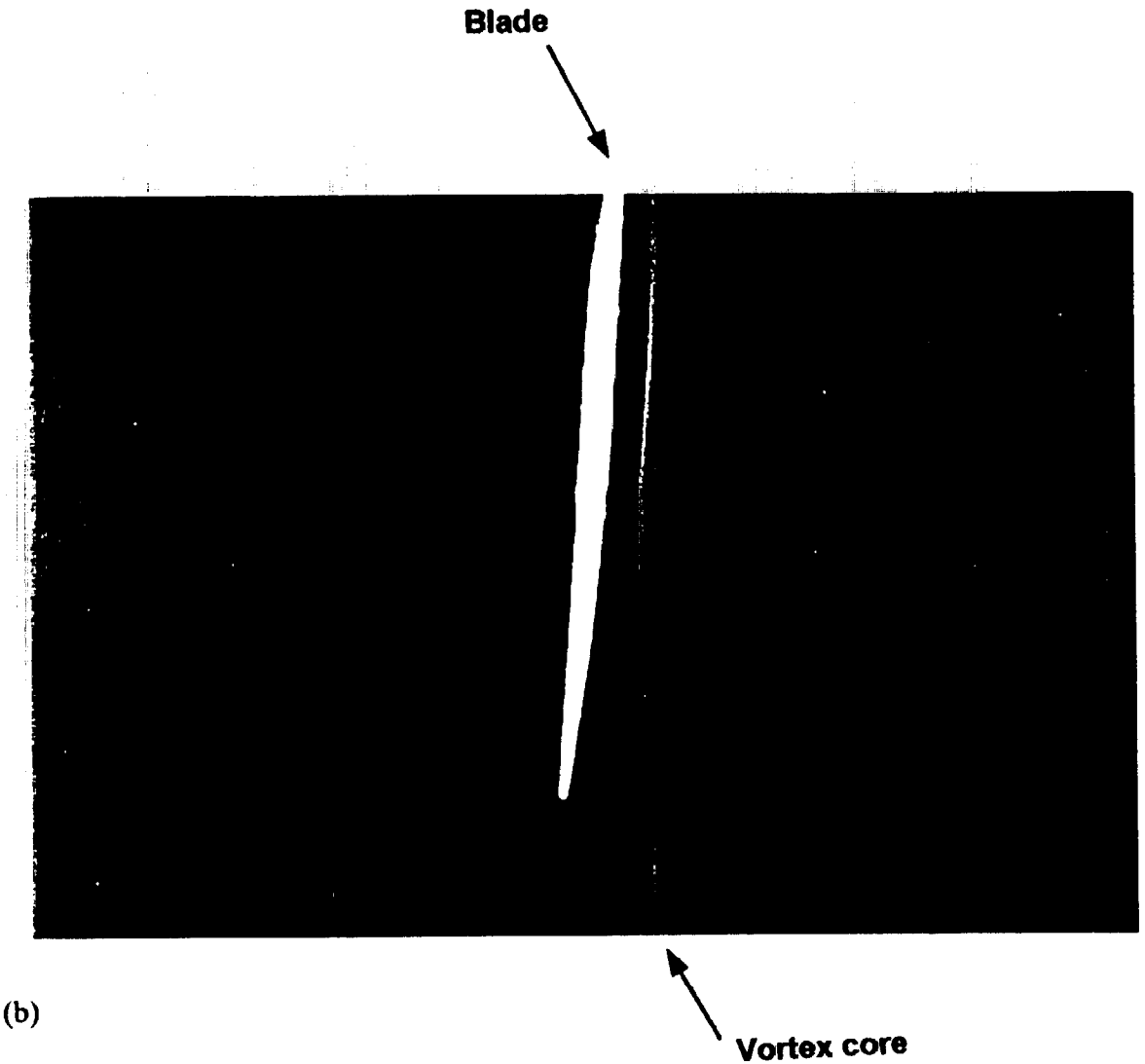

Figure 15. Flow visualization for z_s = -.063, Re_c = 260,000, $\alpha_1 = \alpha_2 = 5°$. (a) Side view. (b) View from blade root.

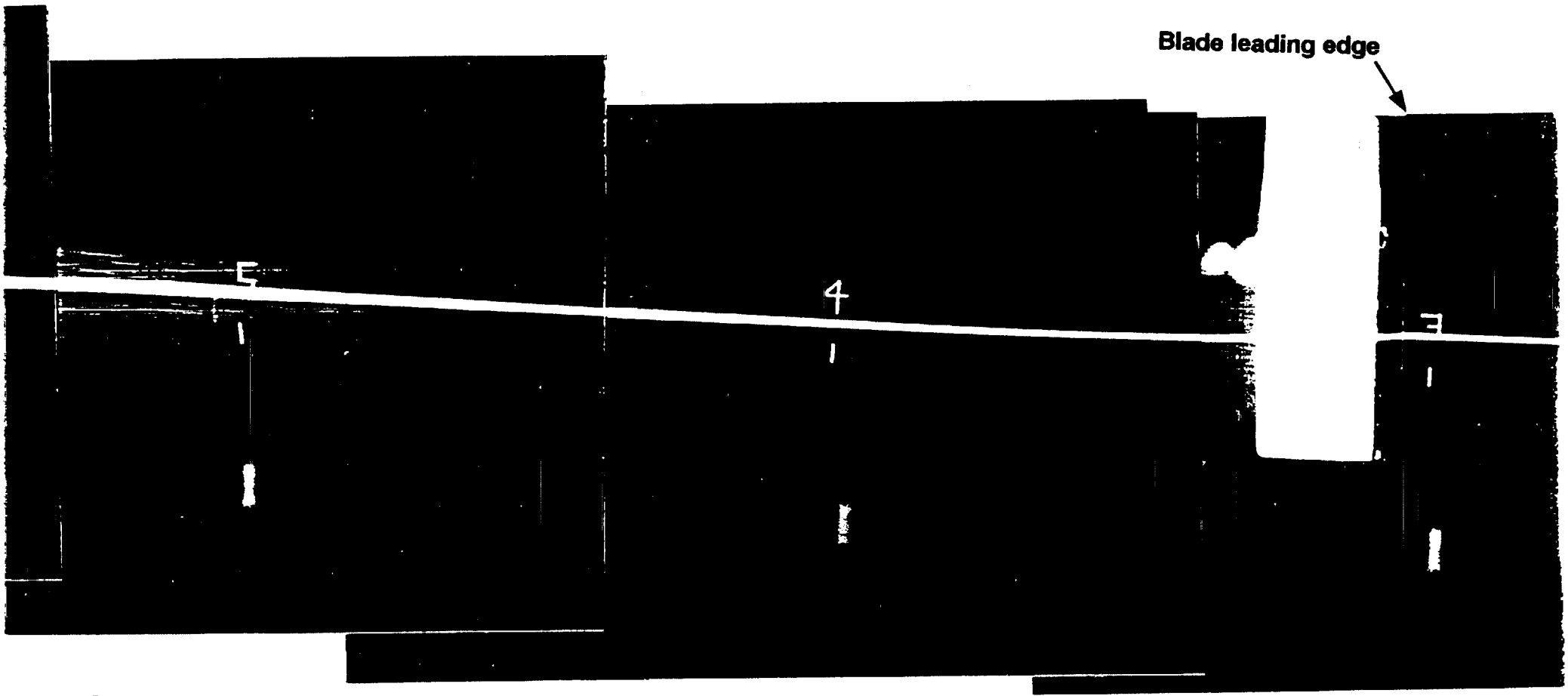

Figure 16. Flow visualization for z_s = -.125, Re_c = 260,000, $\alpha_1 = \alpha_2$ = 5°. Side view.

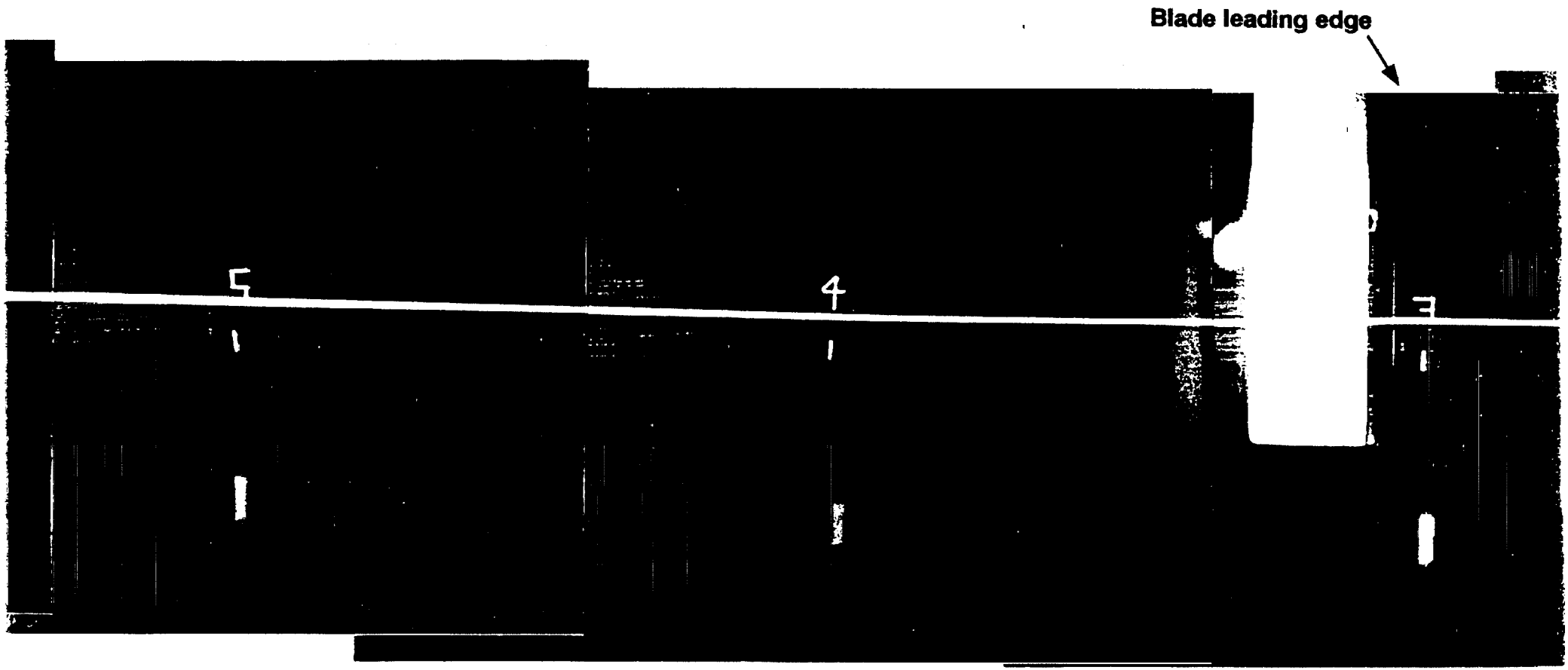

Figure 17. Flow visualization for z_s = -.188, Re_c = 260,000, $\alpha_1 = \alpha_2 = 5°$. Side view.

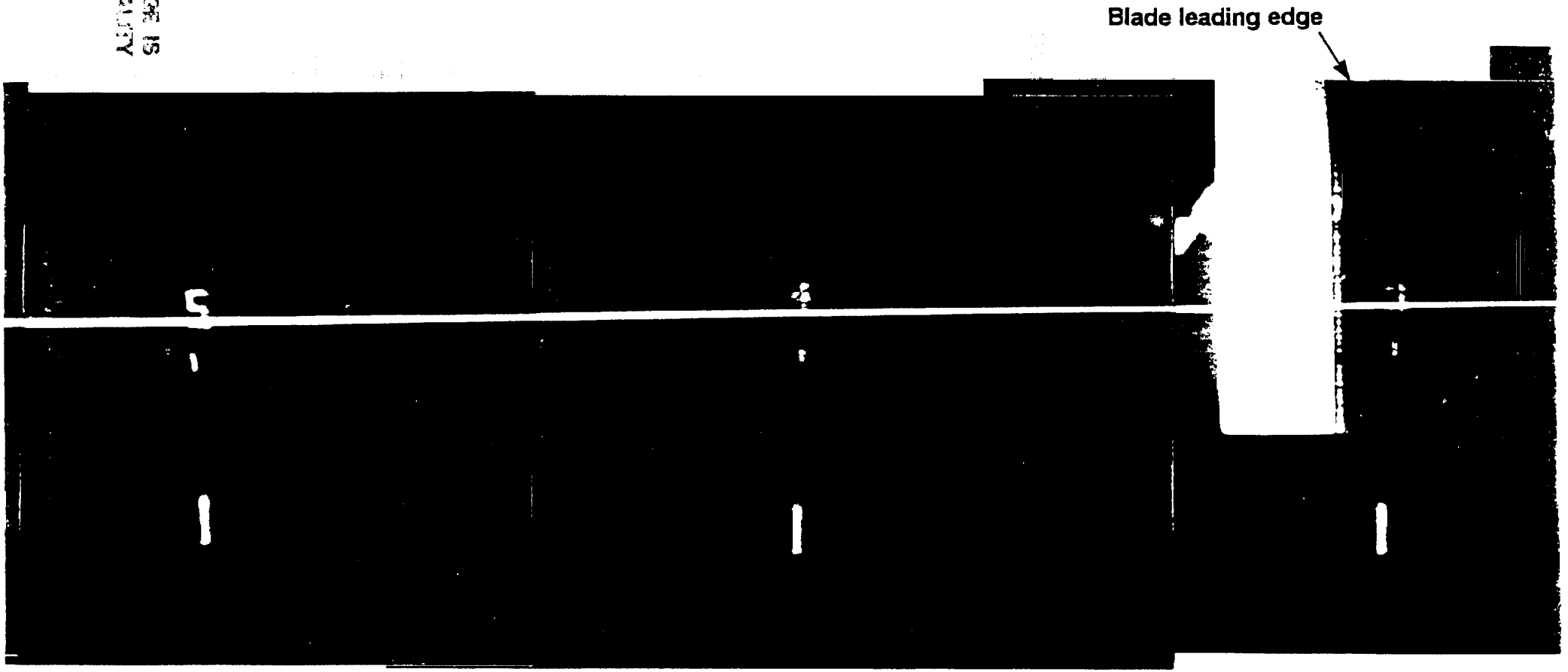

Figure 18. Flow visualization for z_s = -.313, Re_c = 260,000, $\alpha_1 = \alpha_2 = 5°$. Side view.

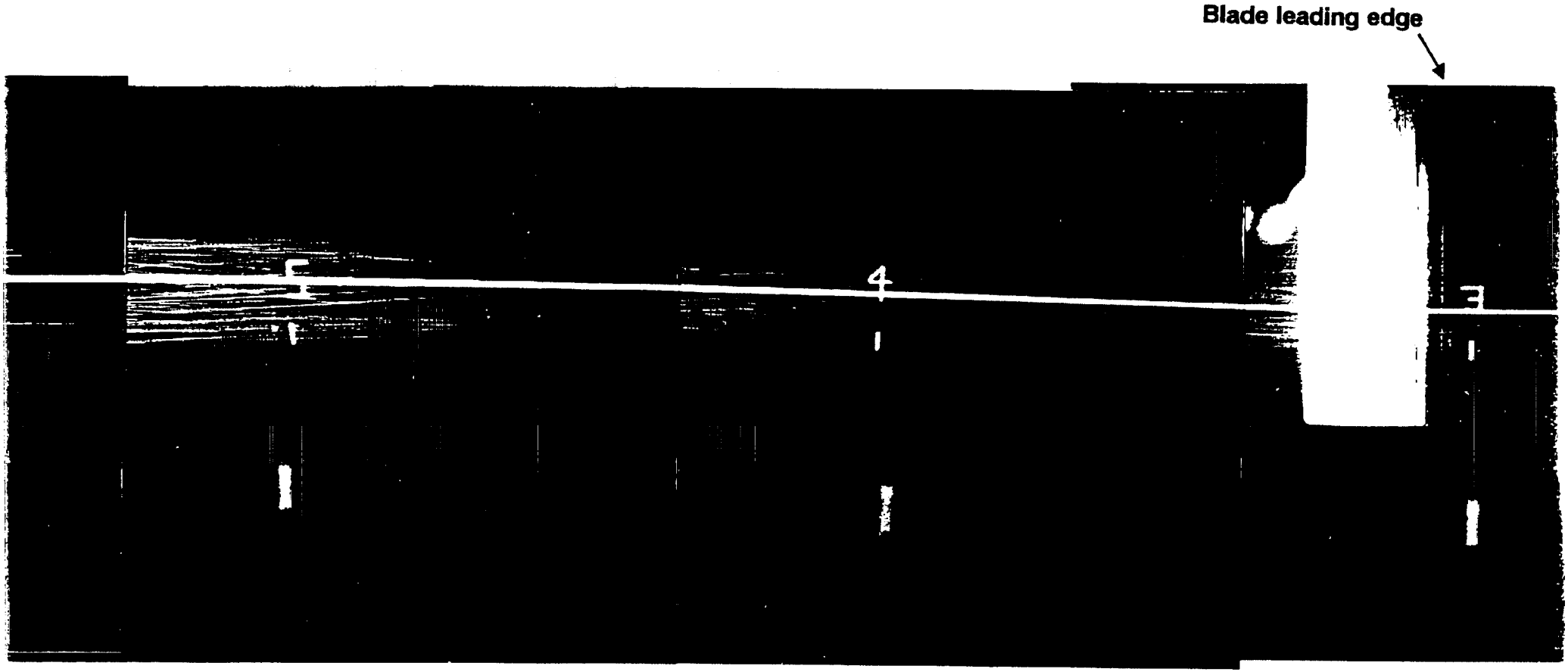

Figure 19. Flow visualization for z_s = -.625, Re_c = 260,000, $\alpha_1 = \alpha_2 = 5°$. Side view.

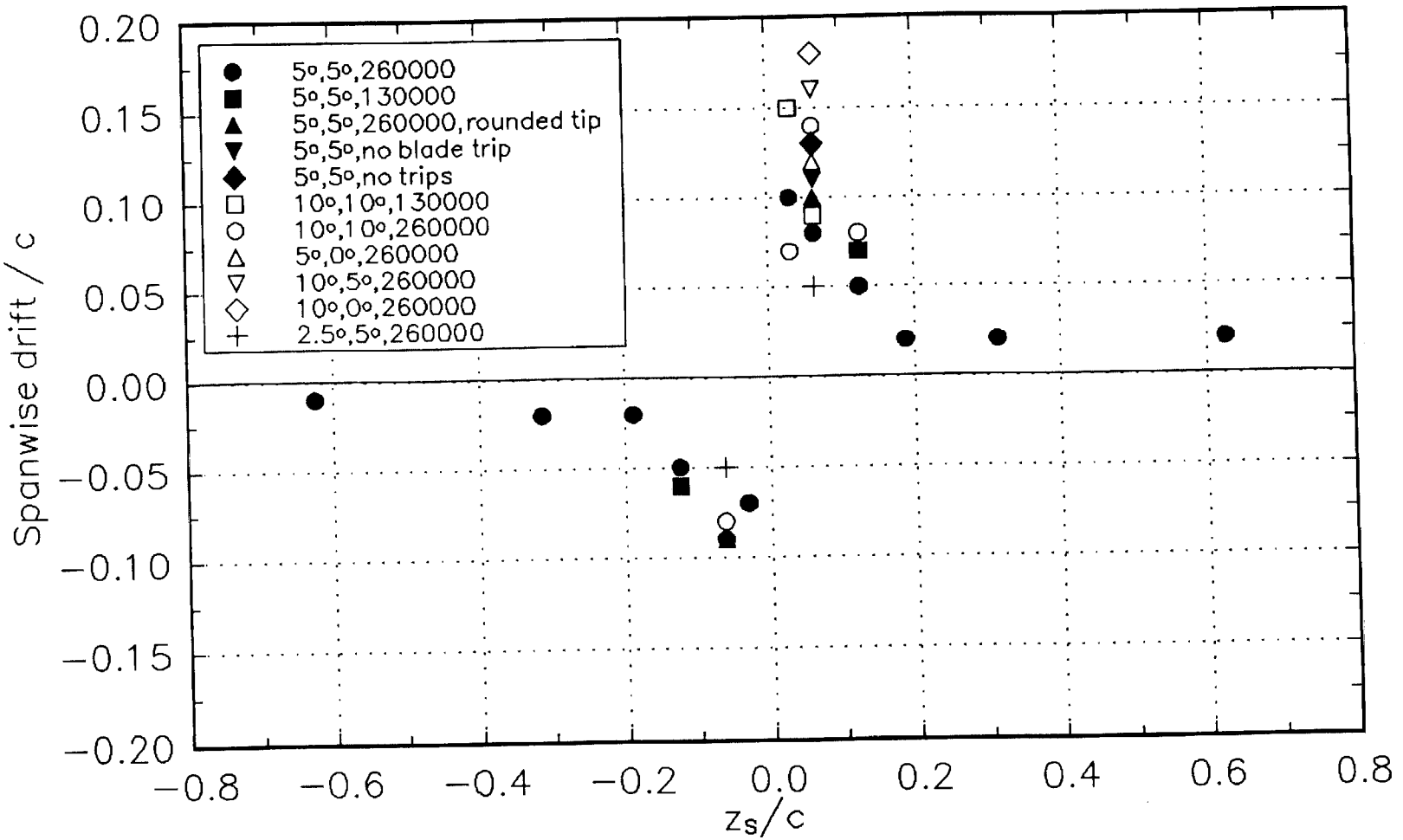

Figure 20(a) Spanwise drift of the vortex between the leading and trailing edges as a function of blade-vortex separation z_s. Numbers in legend are, respectively, angle of attack of vortex generator, angle of attack of blade, chord Reynolds number.

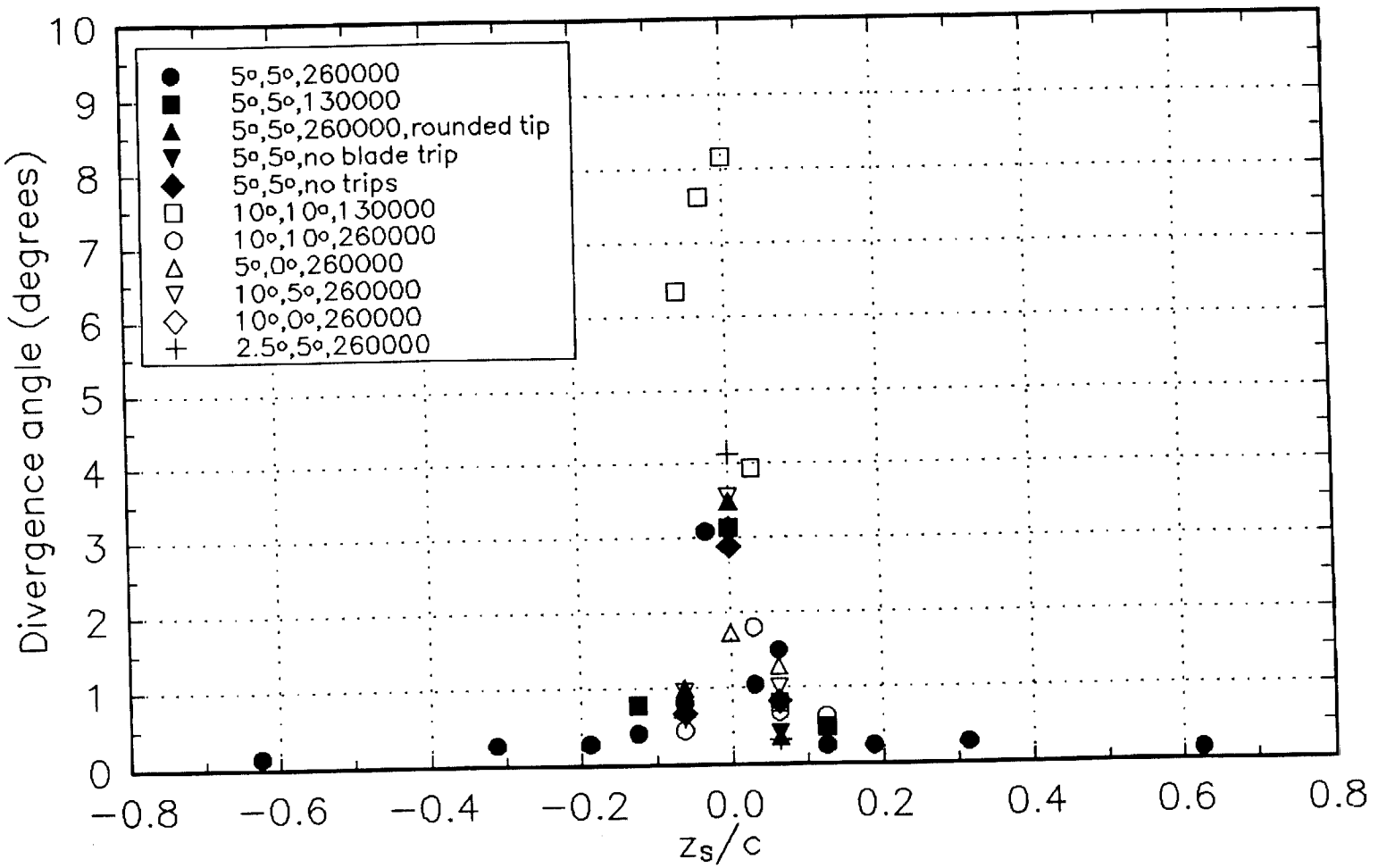

Figure 20(b) Divergence angle of bubble stream marking the vortex core as a function of blade vortex separation z_s. Numbers in legend are, respectively, angle of attack of vortex generator, angle of attack of blade, chord Reynolds number.

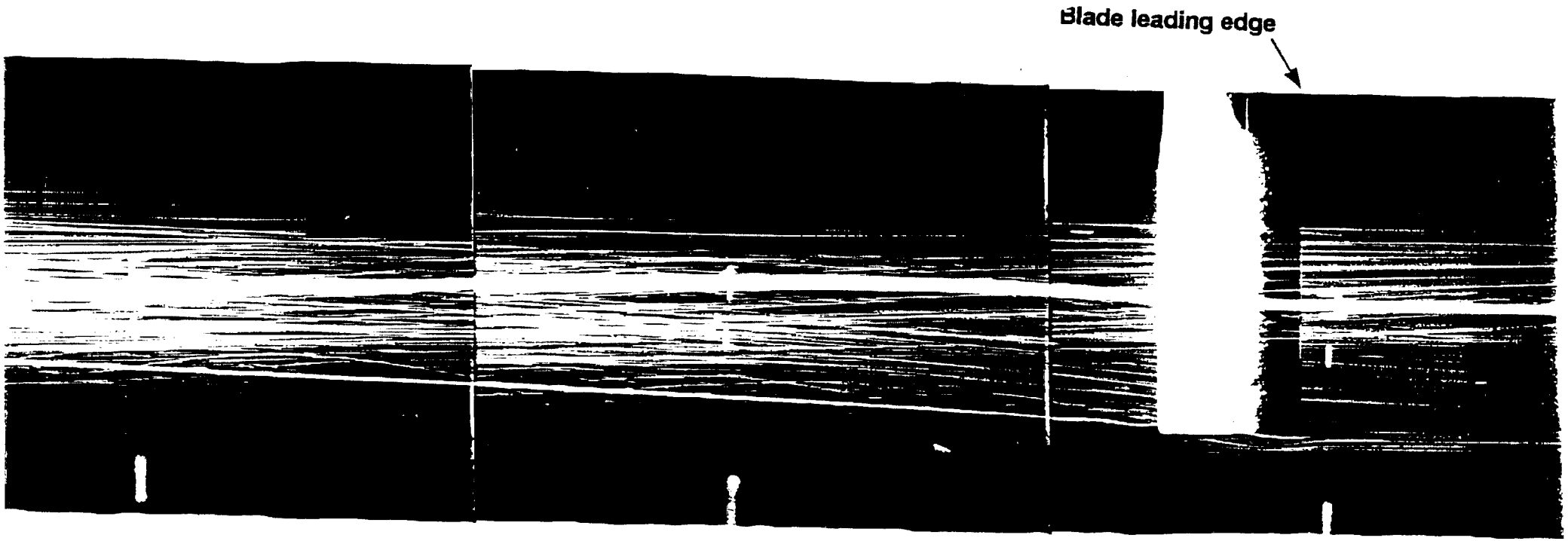

Figure 21. Flow visualization for z_s = .125, Re_c = 130,000, $\alpha_1 = \alpha_2 = 5°$. Side view.

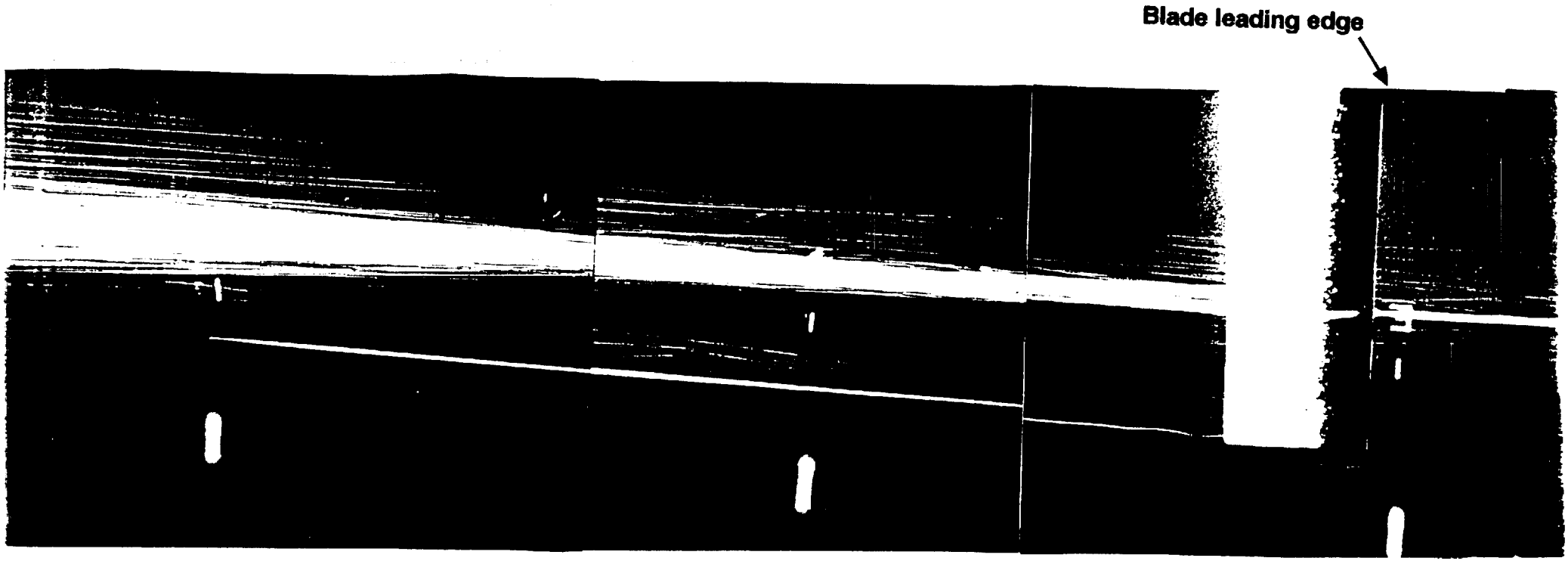

(a)

Figure 22. Flow visualization for z_s = .0, Re_c = 130,000, $\alpha_1 = \alpha_2 = 5°$. Side view.

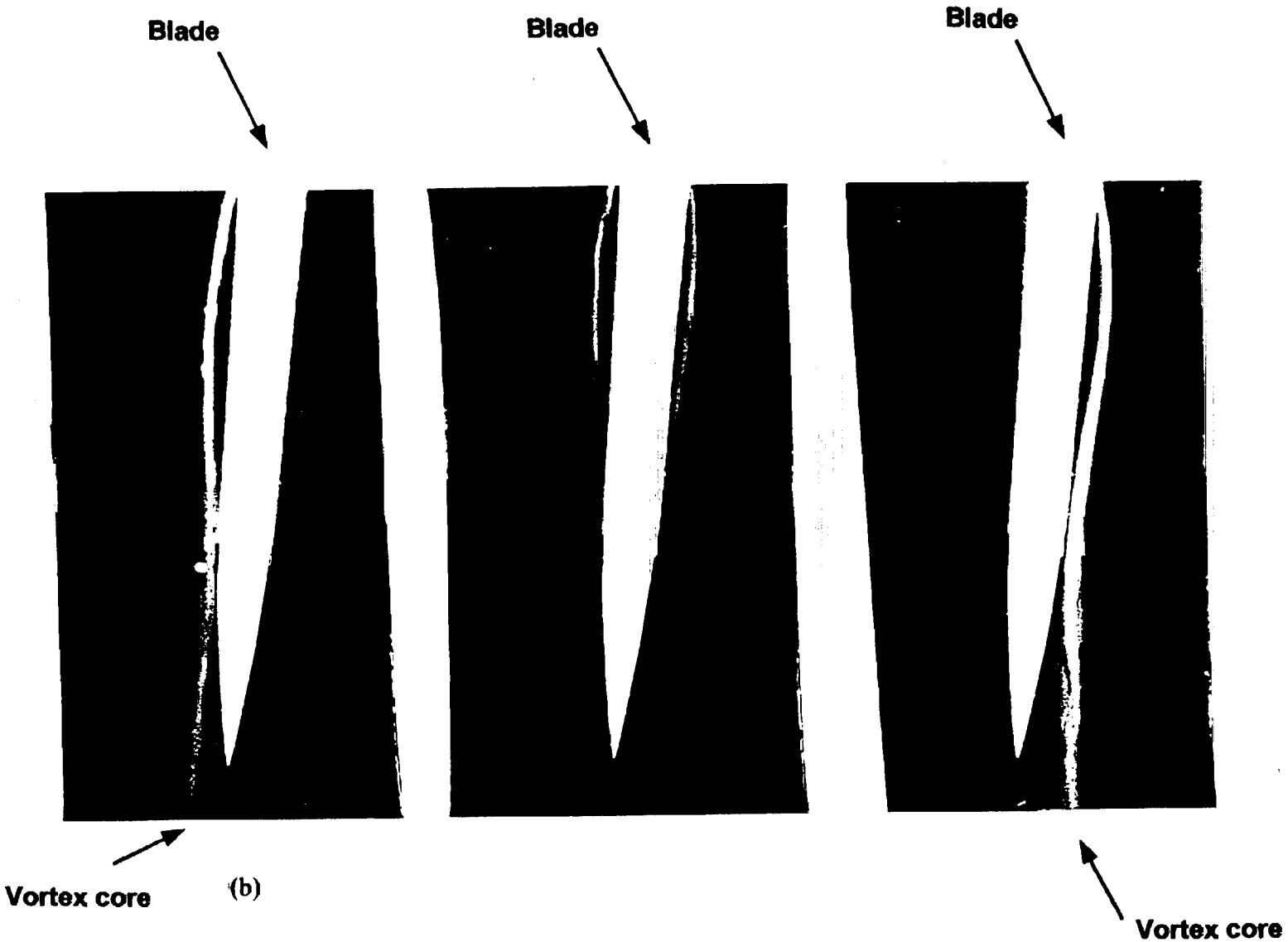

Figure 22. Flow visualization for $z_s = .0$, $Re_c = 130{,}000$, $\alpha_1 = \alpha_2 = 5°$. (a) Side view. (b) Successive views from the blade root.

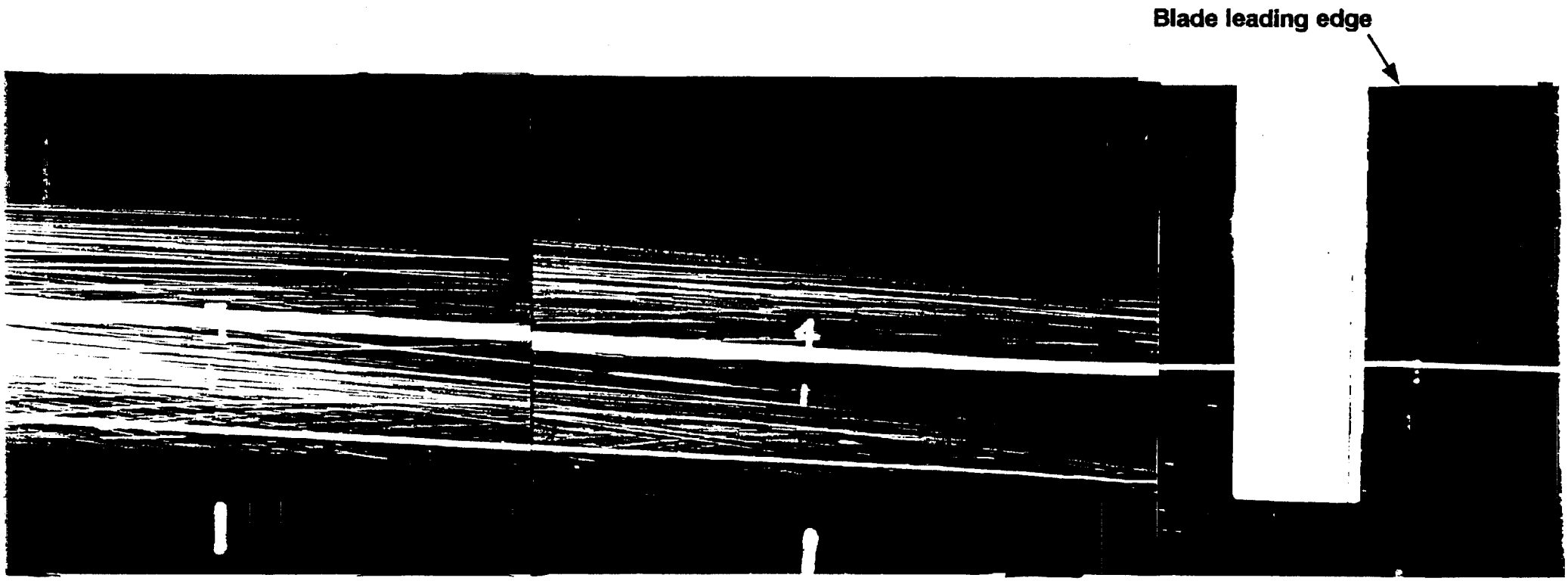

Figure 23. Flow visualization for z_s = -.125, Re_c = 130,000, $\alpha_1 = \alpha_2 = 5°$. Side view.

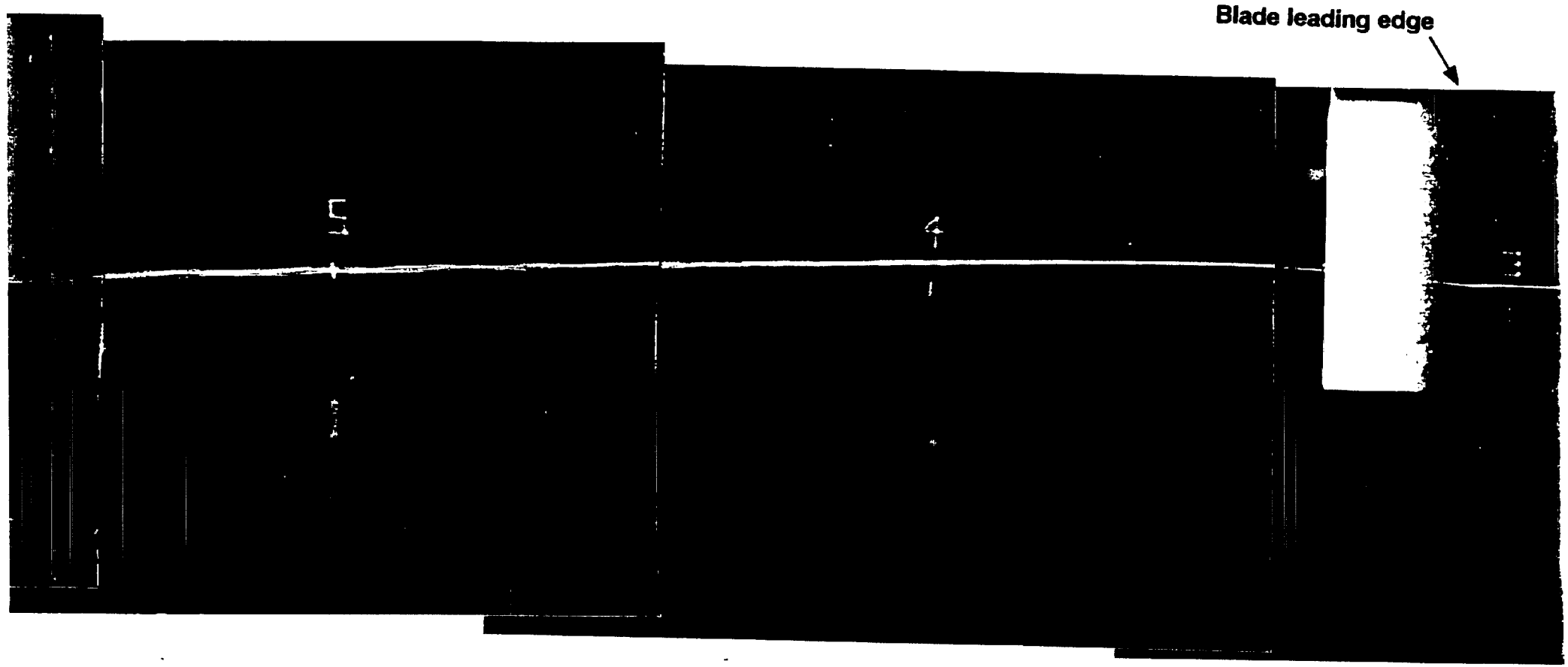

Figure 24. Flow visualization for $z_s = .063$, $Re_c = 260{,}000$, $\alpha_1 = \alpha_2 = 5°$, with rounded tip on vortex generator. Side view.

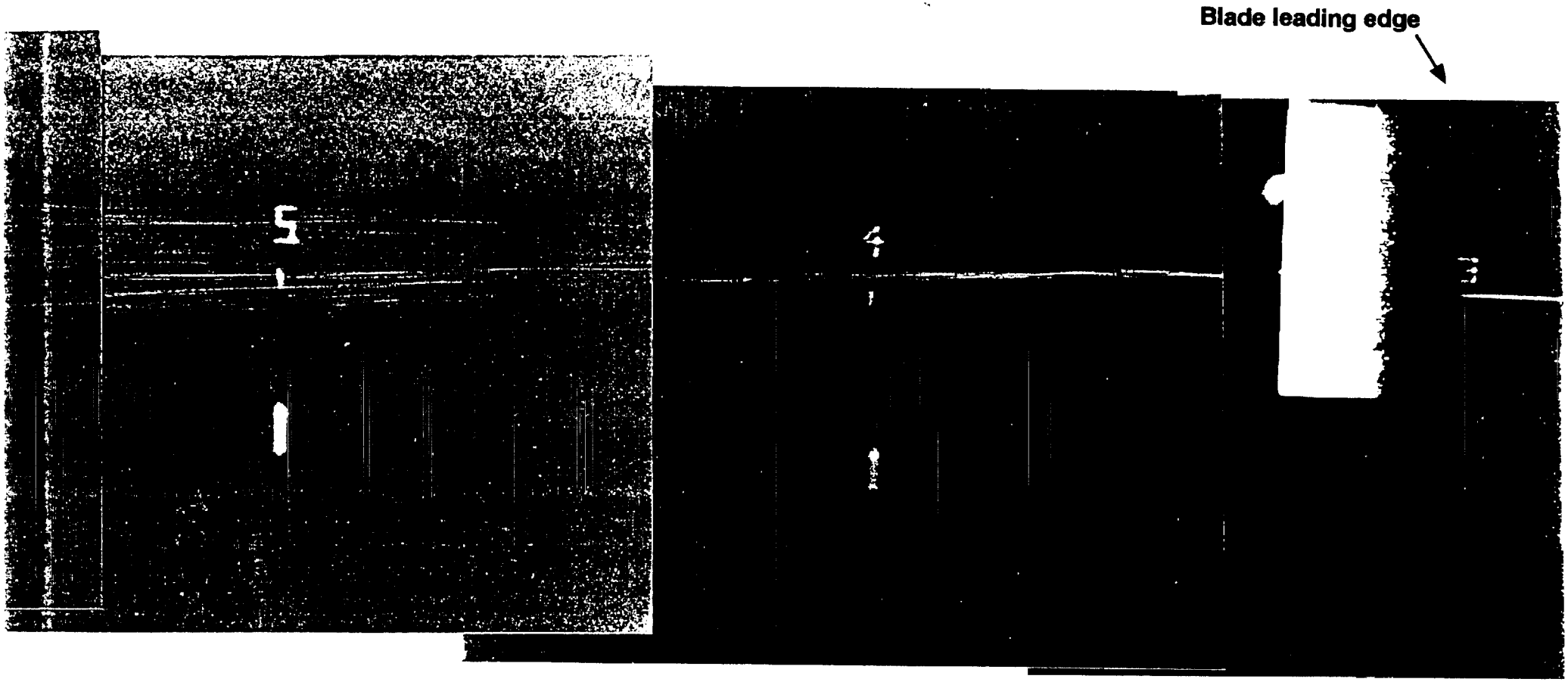

Figure 25. Flow visualization for z_s = .0, Re_c = 260,000, $\alpha_1 = \alpha_2 = 5°$, with rounded tip on vortex generator. Side view.

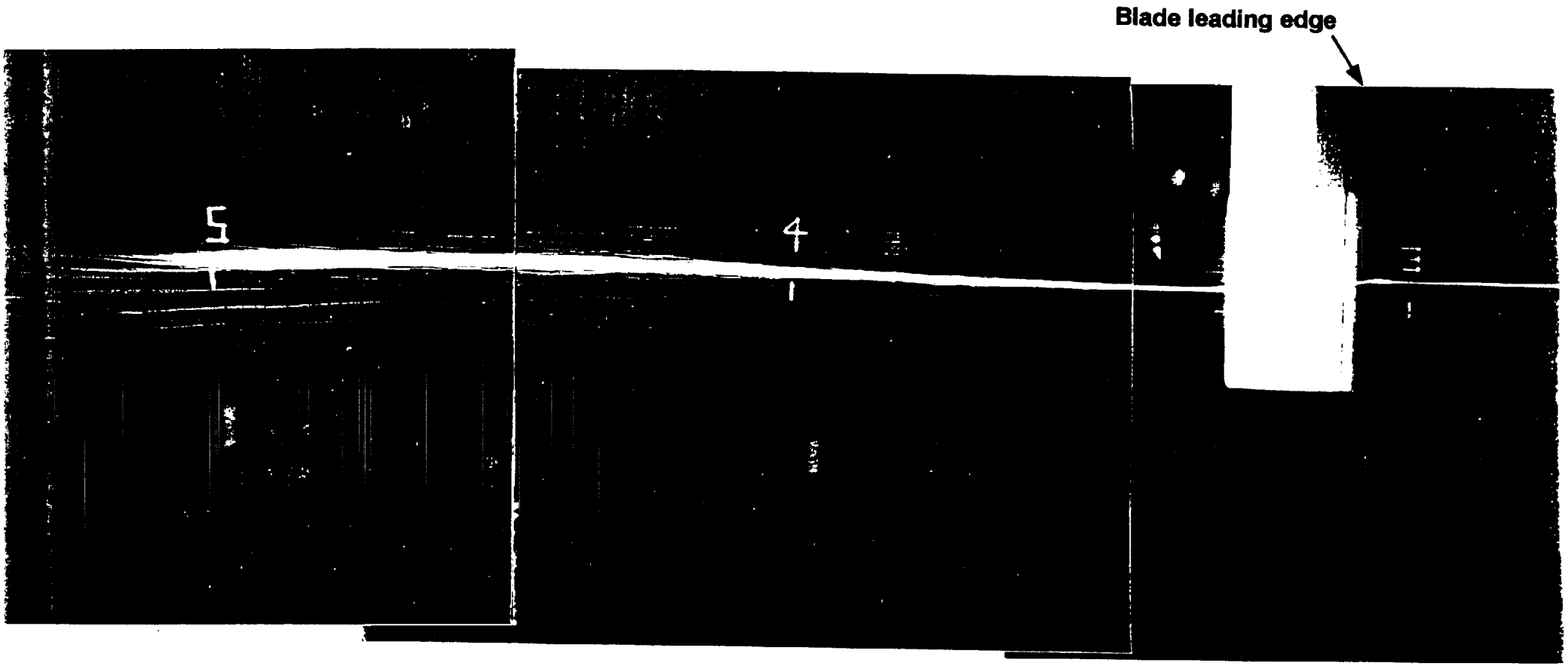

Figure 26. Flow visualization for z_s = -.063, Re_c = 260,000, $\alpha_1 = \alpha_2 = 5°$, with rounded tip on vortex generator. Side view.

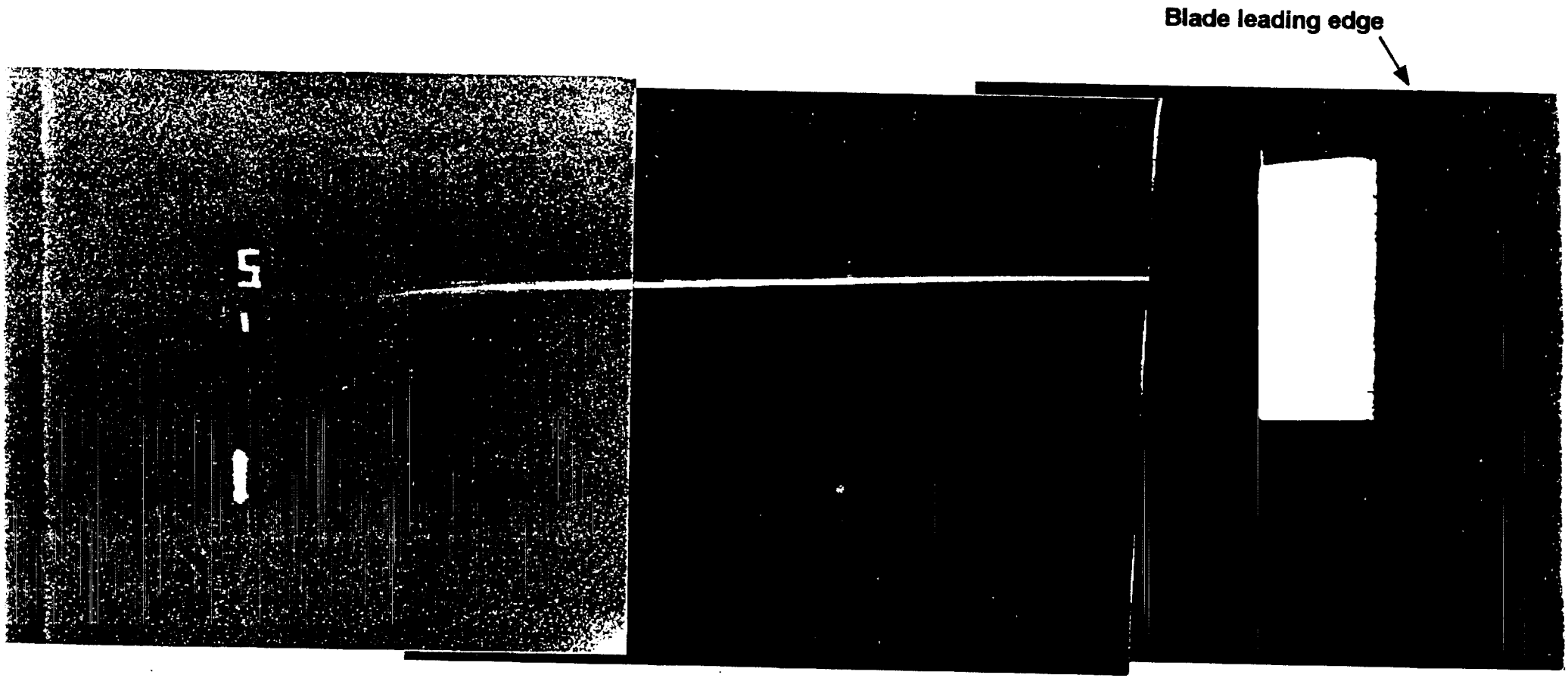

Figure 27. Flow visualization for z_s = .063, Re_c = 260,000, $\alpha_1 = \alpha_2 = 5°$, trip removed from blade. Side view.

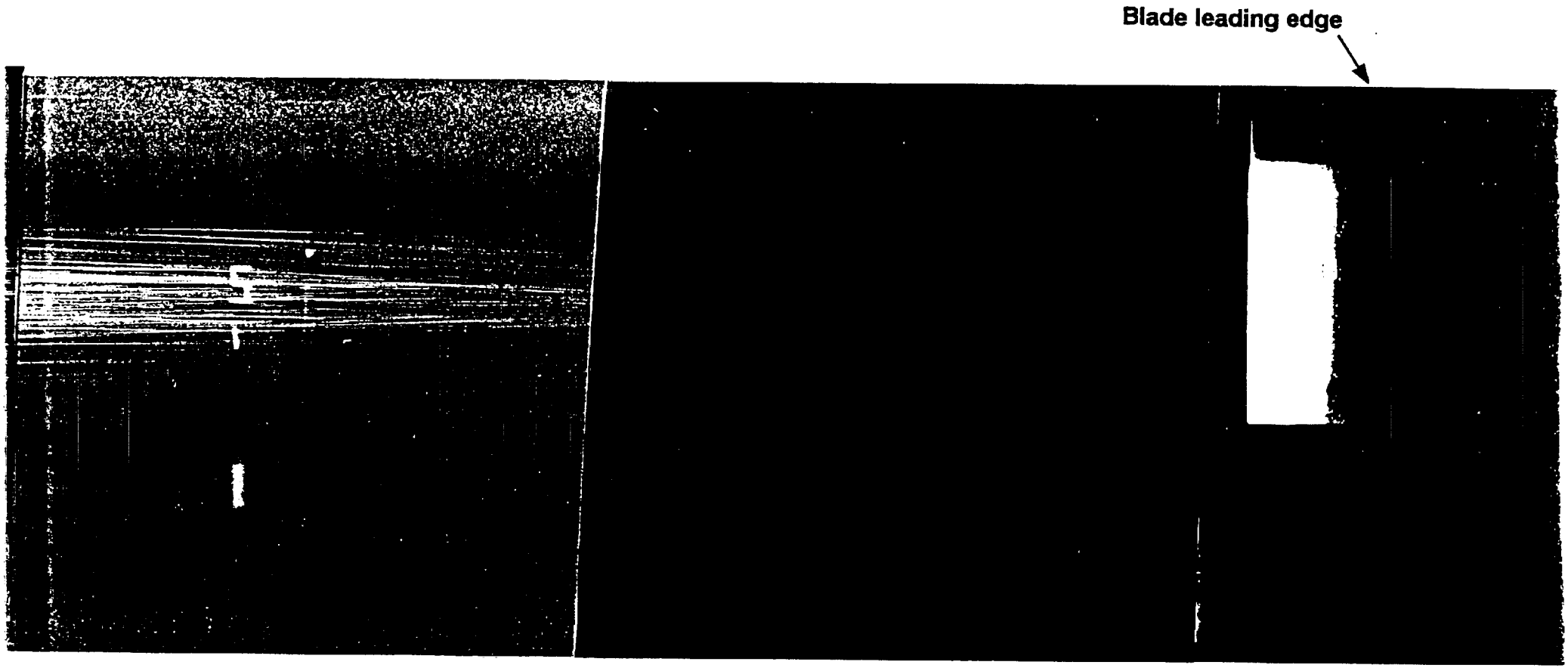

Figure 28. Flow visualization for z_s = .0, Re_c = 260,000, $\alpha_1 = \alpha_2 = 5°$, trip removed from blade. Side view.

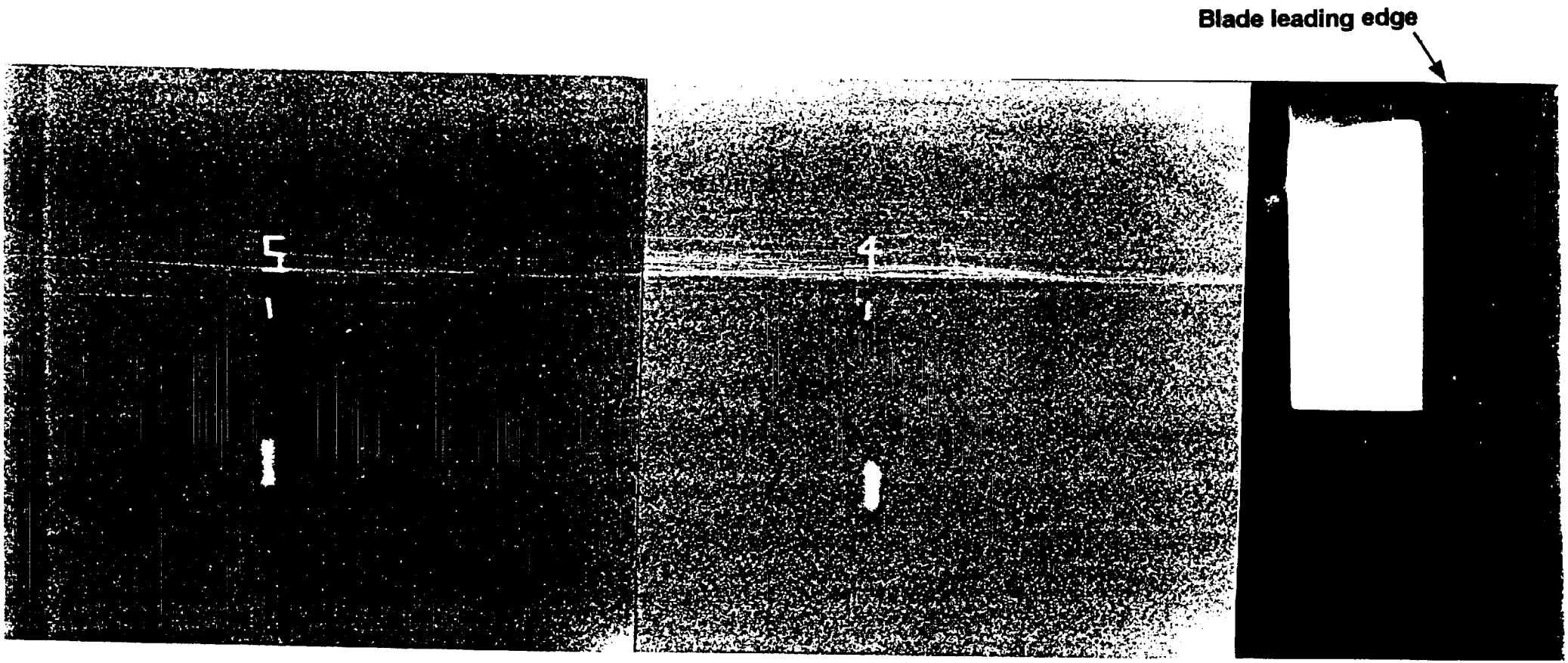

Figure 29. Flow visualization for z_s = -.063, Re_c = 260,000, $\alpha_1 = \alpha_2 = 5°$, trip removed from blade. Side view.

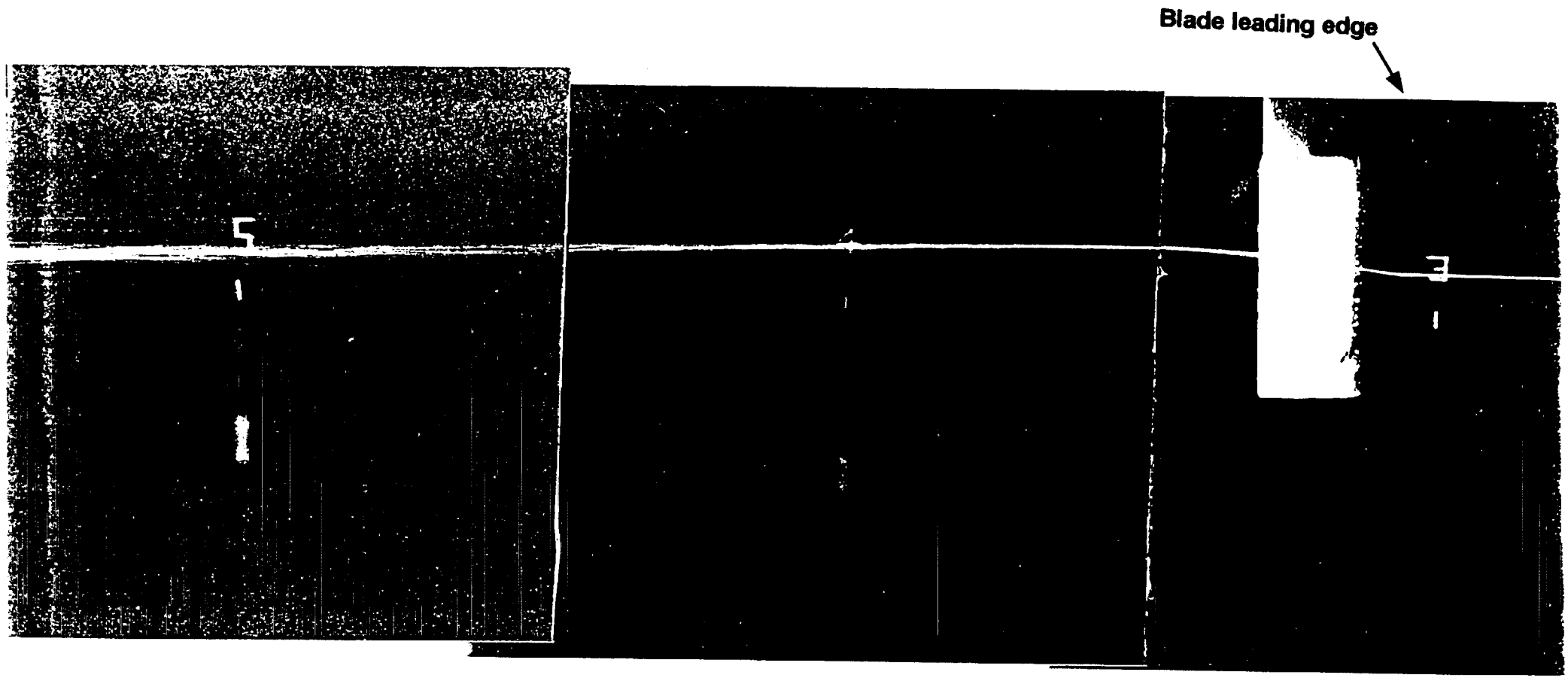

Figure 30. Flow visualization for z_s = .063, Re_c = 260,000, $\alpha_1 = \alpha_2 = 5°$, trip removed from vortex generator and blade. Side view.

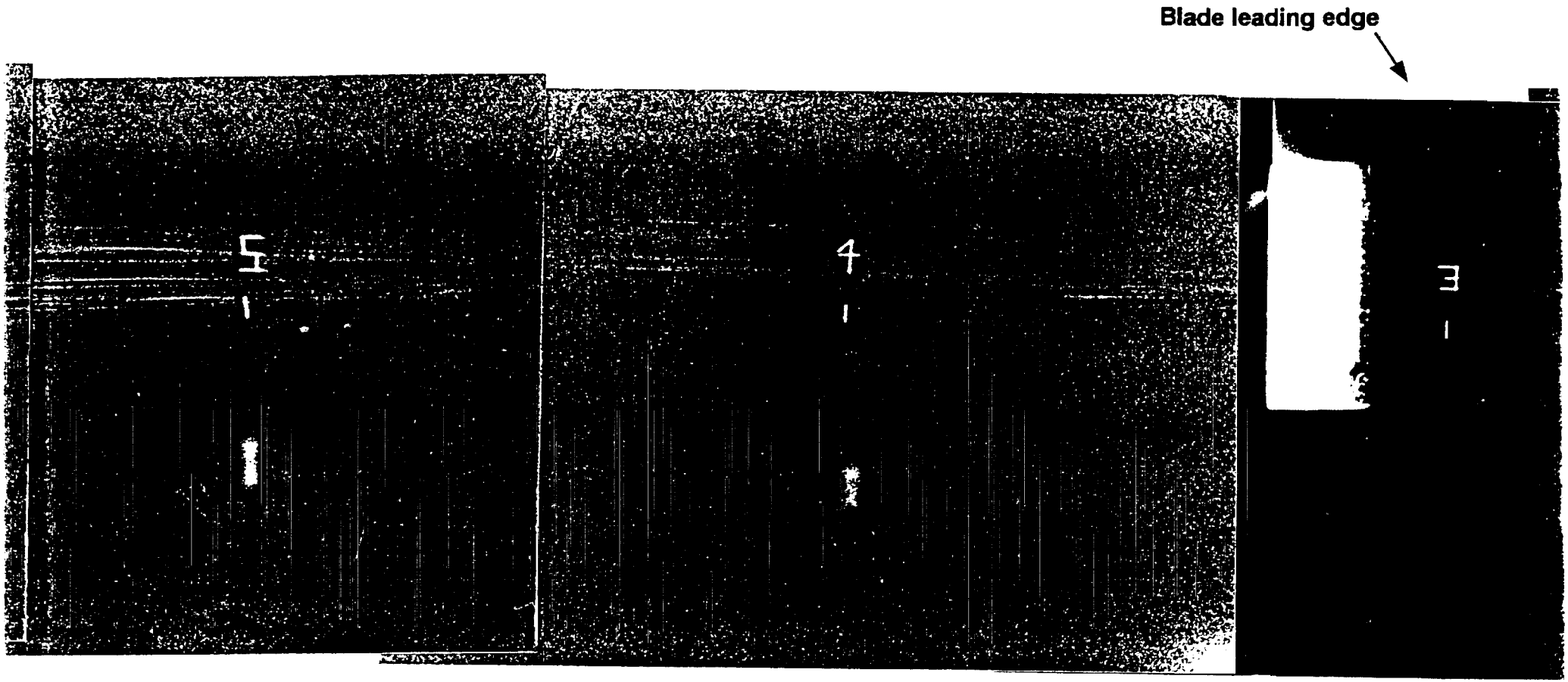

Figure 31. Flow visualization for $z_s = .0$, $Re_c = 260{,}000$, $\alpha_1 = \alpha_2 = 5°$, trip removed from vortex generator and blade. Side view.

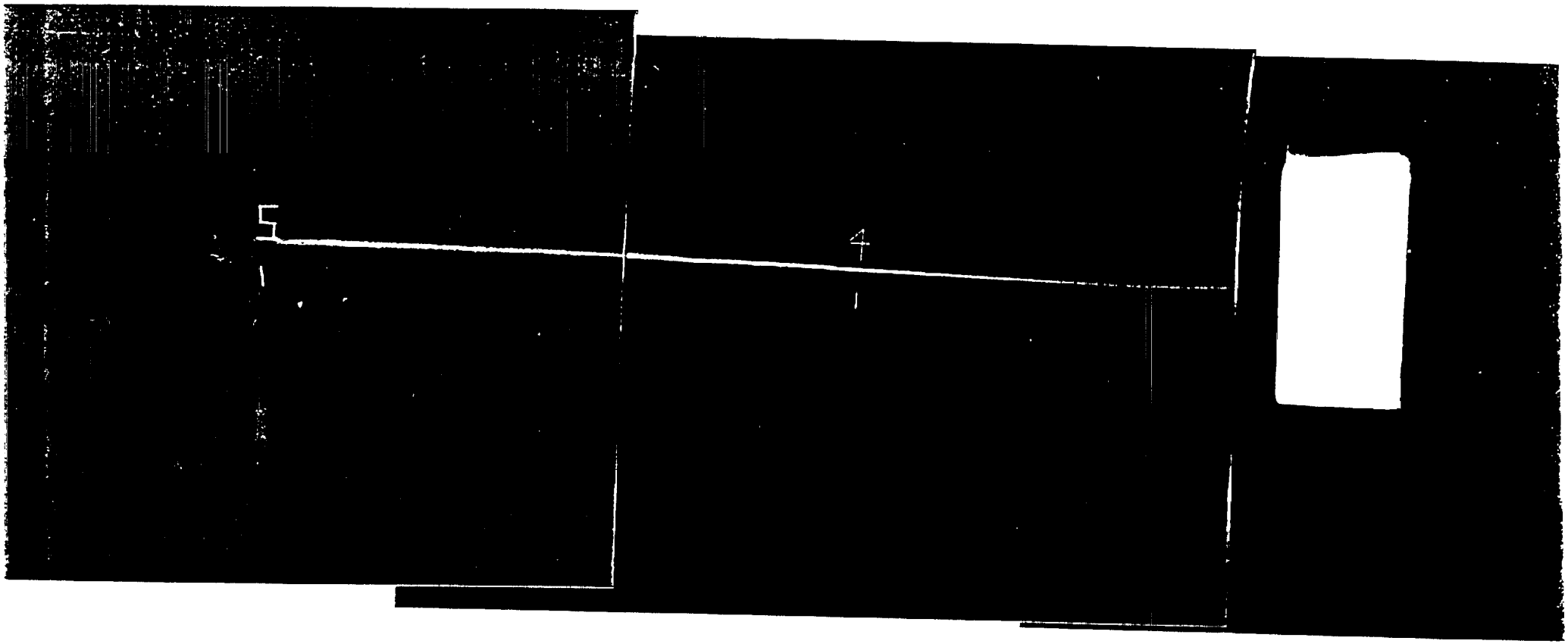

Figure 32. Flow visualization for z_s = -.063, Re_c = 260,000, $\alpha_1 = \alpha_2 = 5°$, trip removed from vortex generator and blade. Side view.

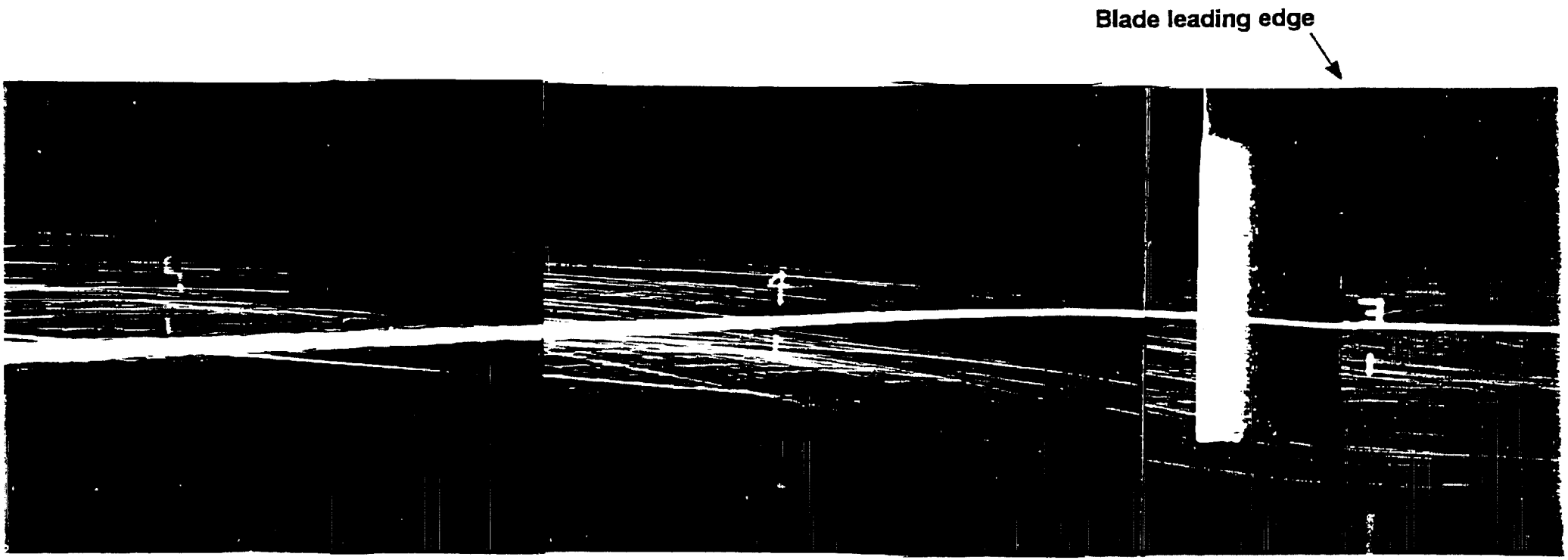

Figure 33. Flow visualization for z_s = .125, Re_c = 130,000, $\alpha_1 = \alpha_2 = 10°$. Side view.

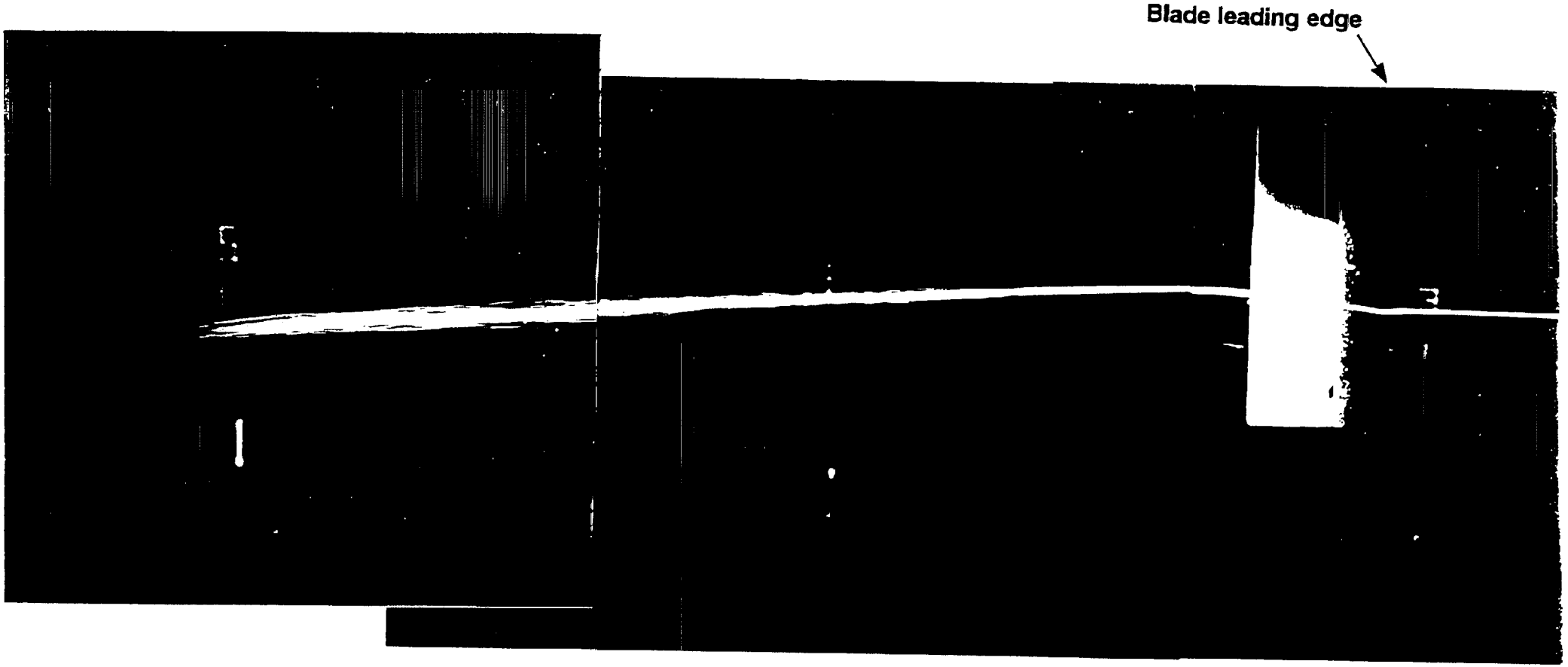

Figure 34. Flow visualization for z_s = .063, Re_c = 130,000, $\alpha_1 = \alpha_2 = 10°$. Side view.

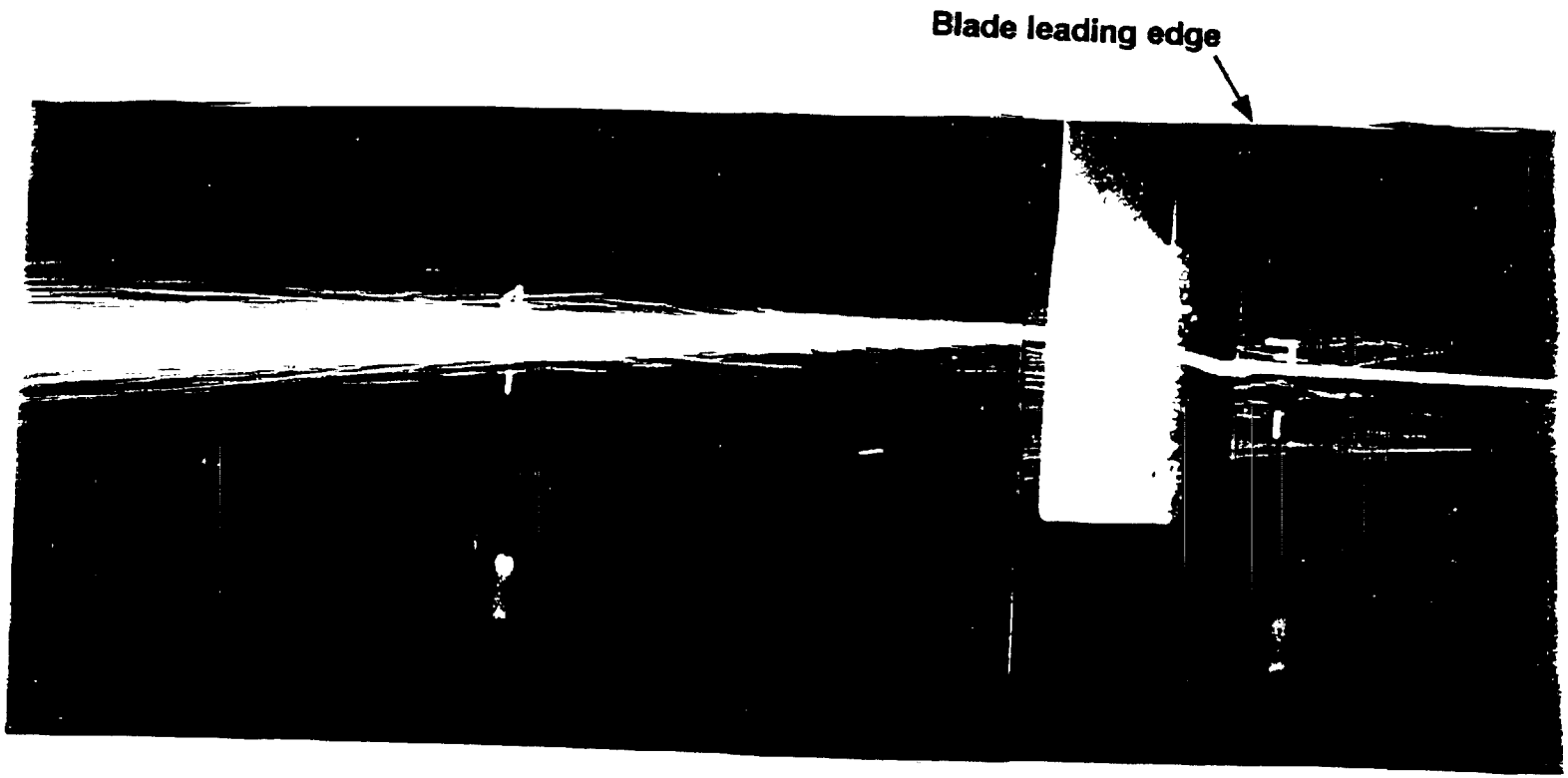

(a)

Figure 35. Flow visualization for z_s = .031, Re_c = 130,000, $\alpha_1 = \alpha_2 = 10°$. (a) Side view. (b) View from downstream. (c) Close up from side. (d) View from root.

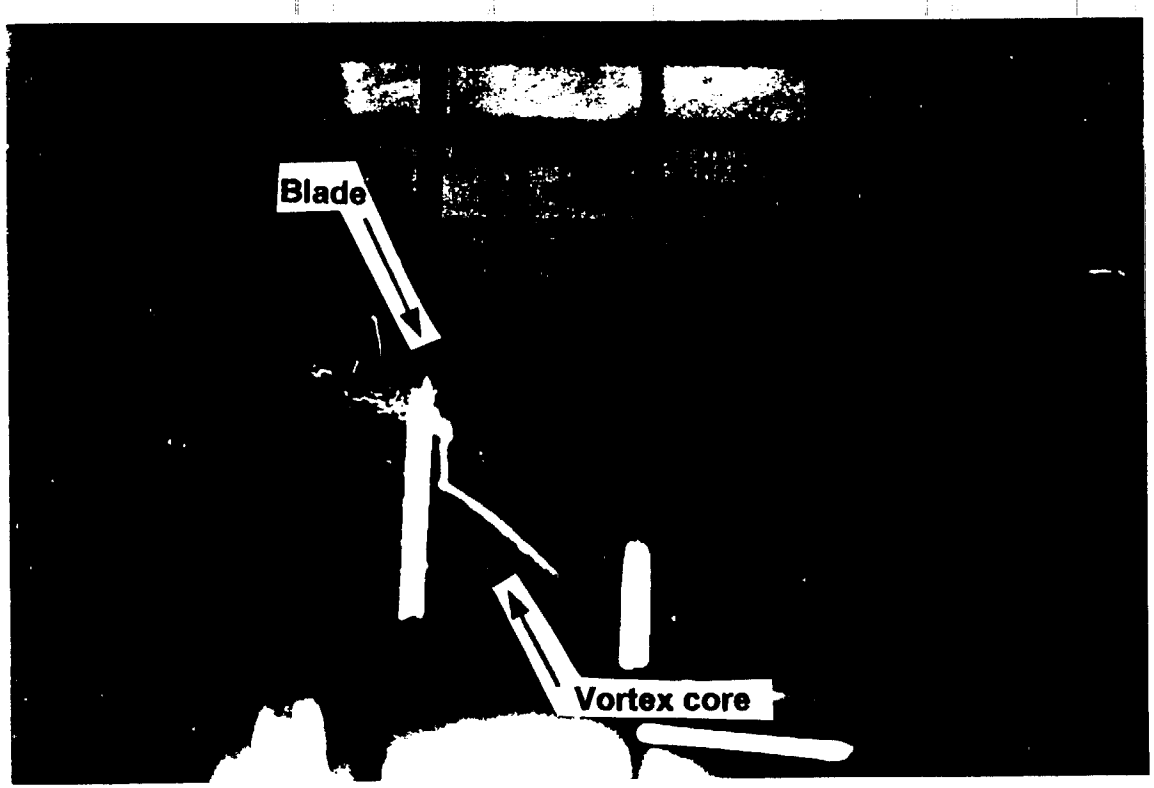

(b)

Figure 35. Flow visualization for z_s = .031, Re_c = 130,000, $\alpha_1 = \alpha_2 = 10°$. (a) Side view. (b) View from downstream. (c) Close up from side. (d) View from root.

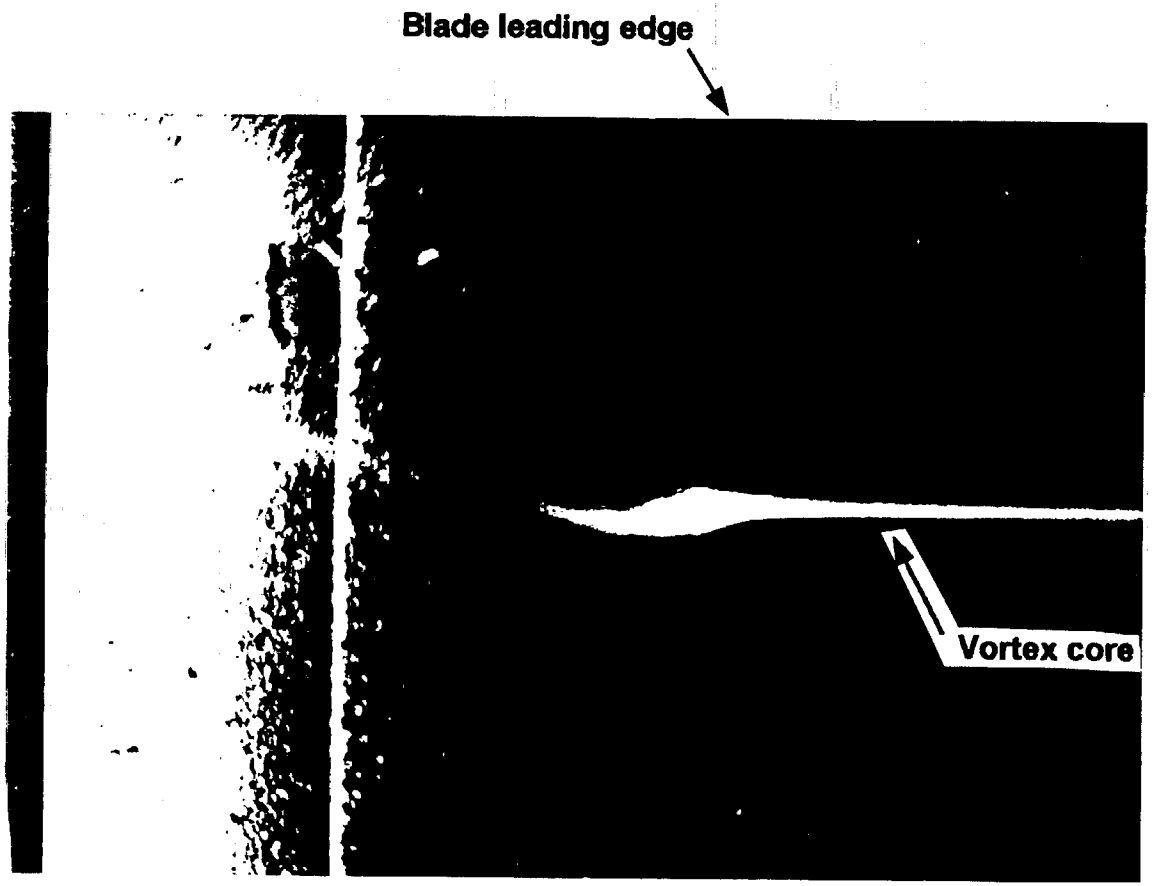

(c)

Figure 35. Flow visualization for z_s = .031, Re_c = 130,000, $\alpha_1 = \alpha_2 = 10°$. (a) Side view. (b) View from downstream. (c) Close up from side. (d) View from root.

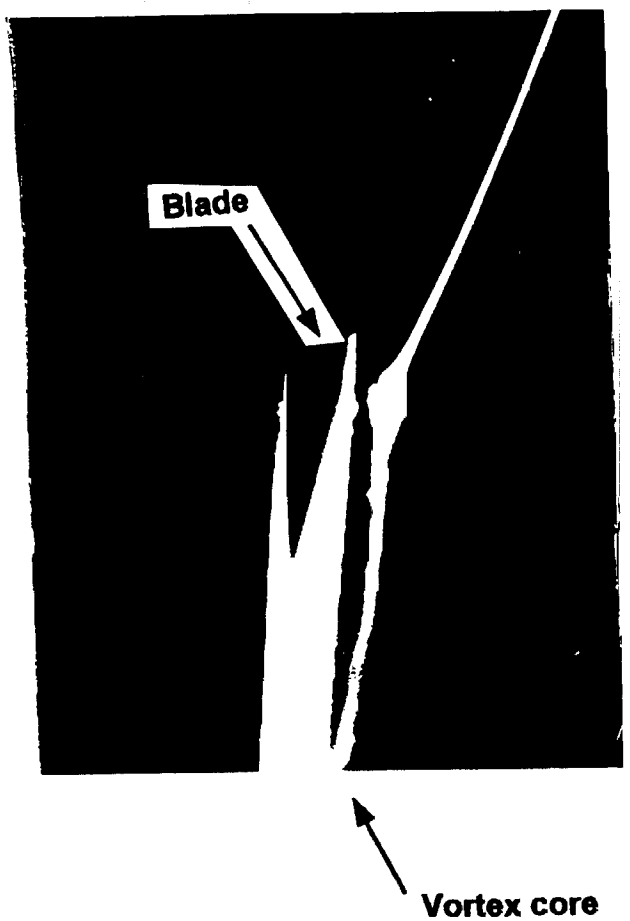

(d)

Figure 35. Flow visualization for z_s = .031, Re_c = 130,000, $\alpha_1 = \alpha_2 = 10°$. (a) Side view. (b) View from downstream. (c) Close up from side. (d) View from root.

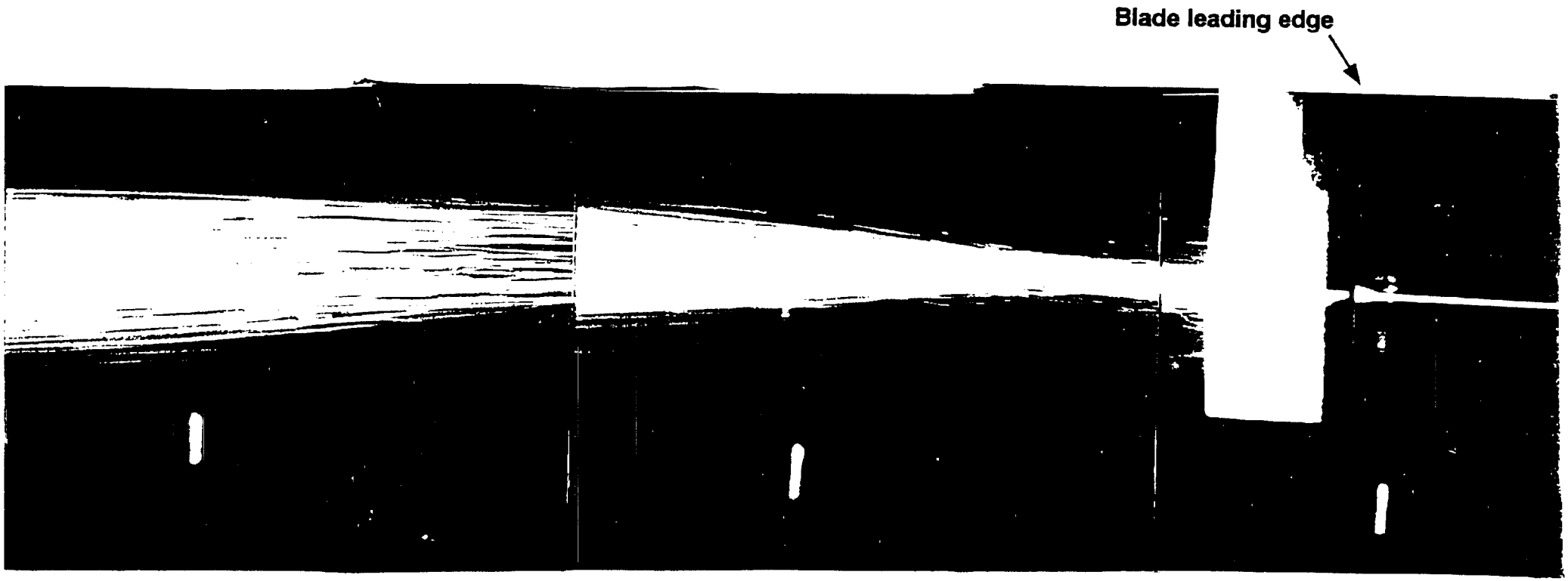

(a)

Figure 36. Flow visualization for z_s = .0, Re_c = 130,000, $\alpha_1 = \alpha_2 = 10°$. (a) Side view. (b) View from downstream. (c) Close up of burst region.

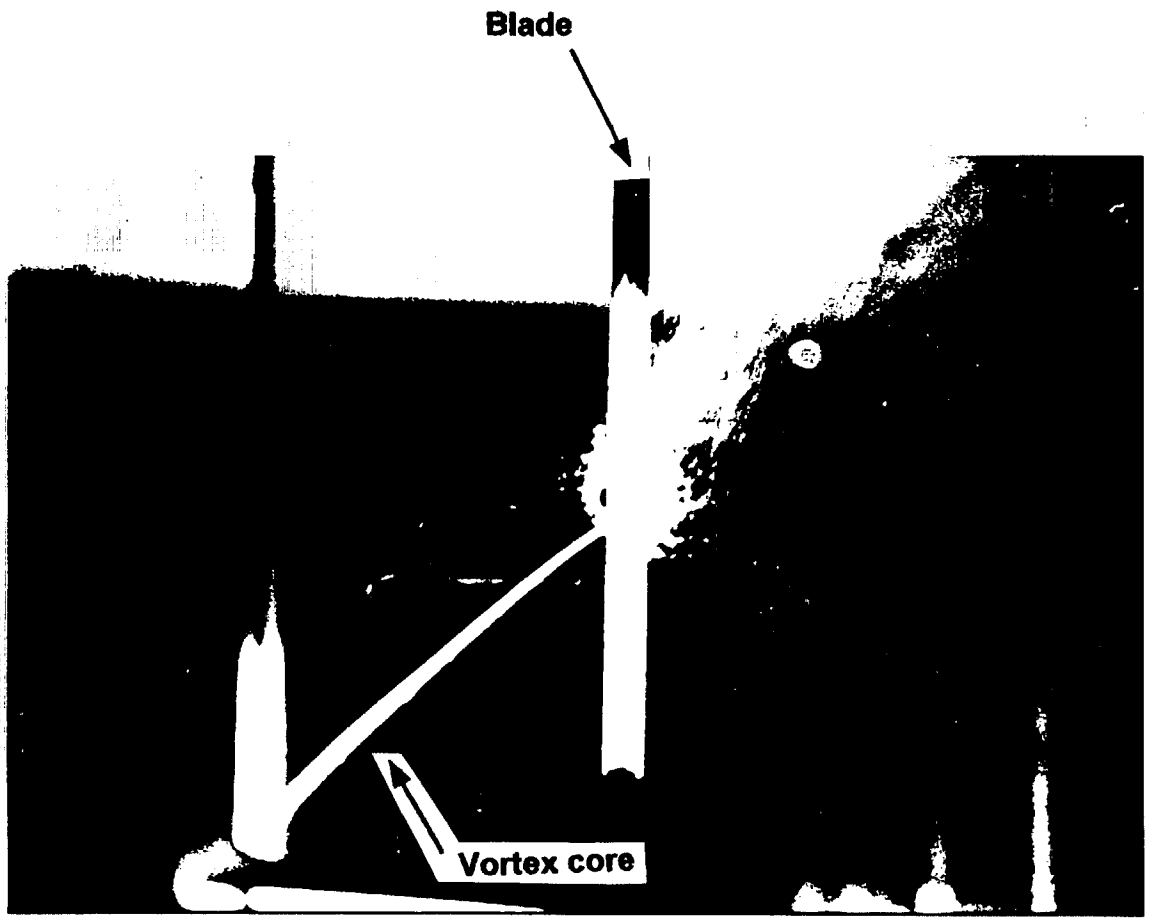

(b)

Figure 36. Flow visualization for $z_s = .0$, $Re_c = 130{,}000$, $\alpha_1 = \alpha_2 = 10°$. (a) Side view. (b) View from downstream. (c) Close up of burst region.

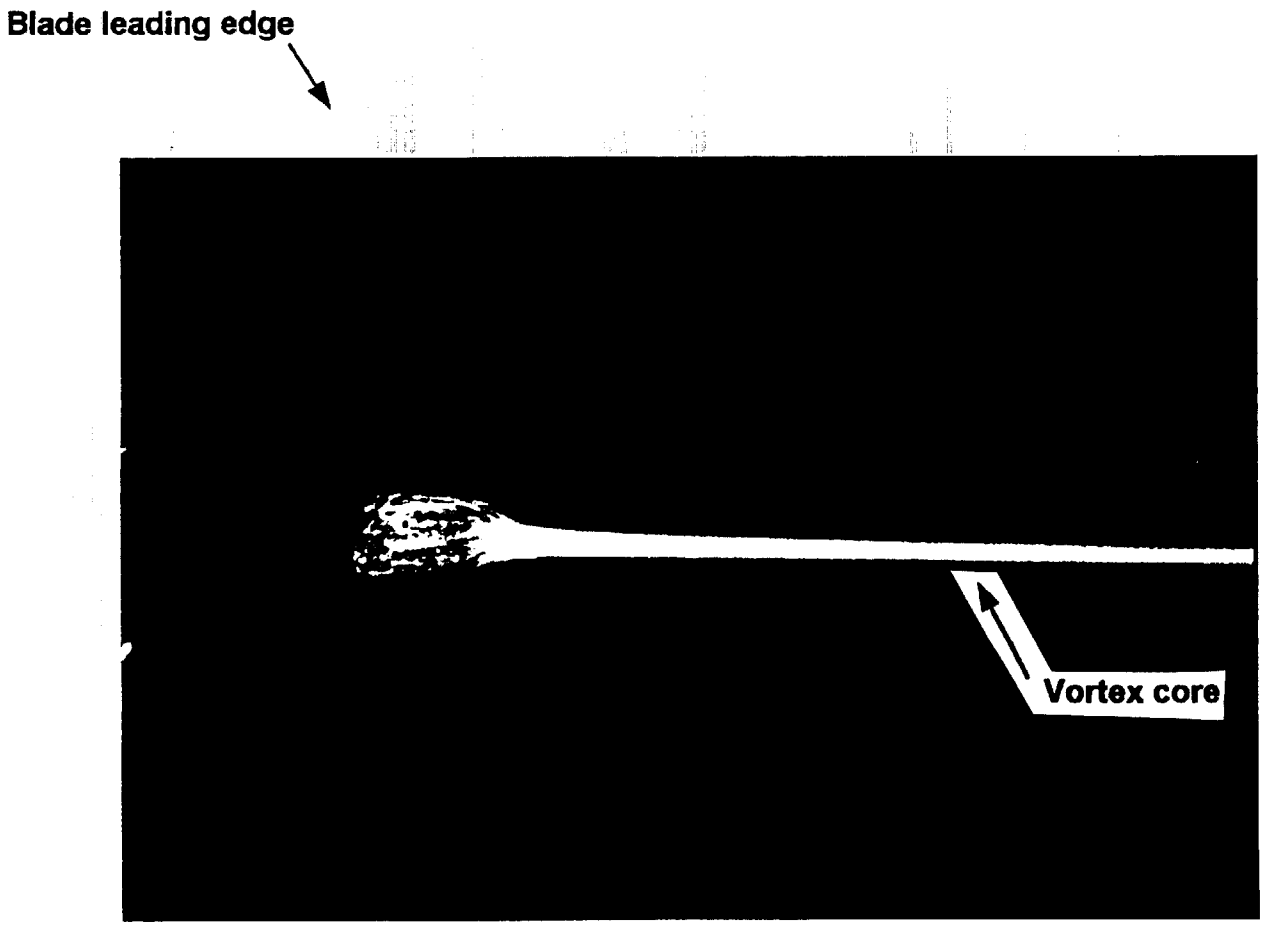

(c)

Figure 36. Flow visualization for $z_s = .0$, $Re_c = 130{,}000$, $\alpha_1 = \alpha_2 = 10°$. (a) Side view. (b) View from downstream. (c) Close up of burst region.

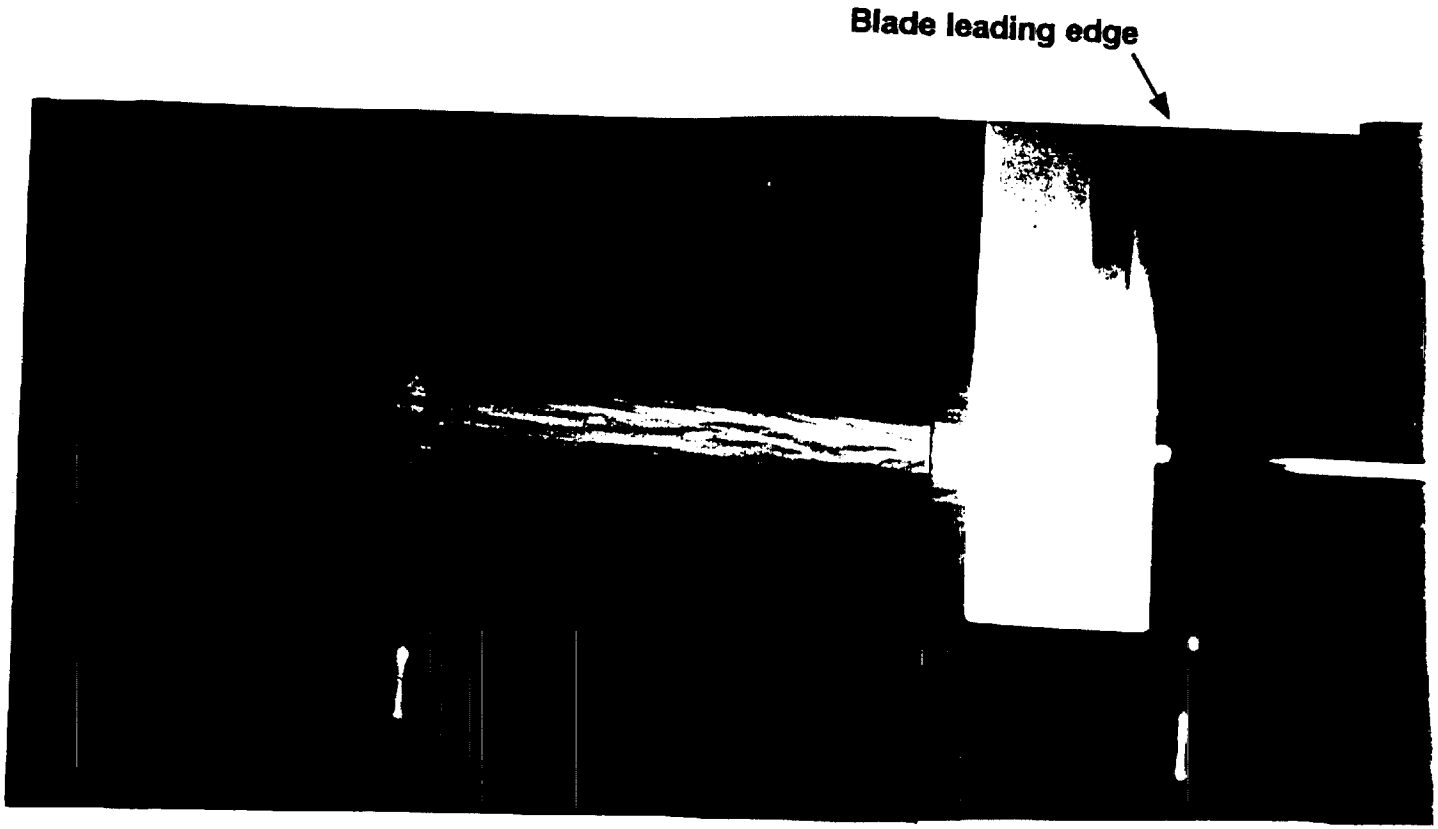

(a)

Figure 37. Flow visualization for z_s = -.063, Re_c = 130,000, $\alpha_1 = \alpha_2 = 10°$. (a) Side view. (b) View from wing root.

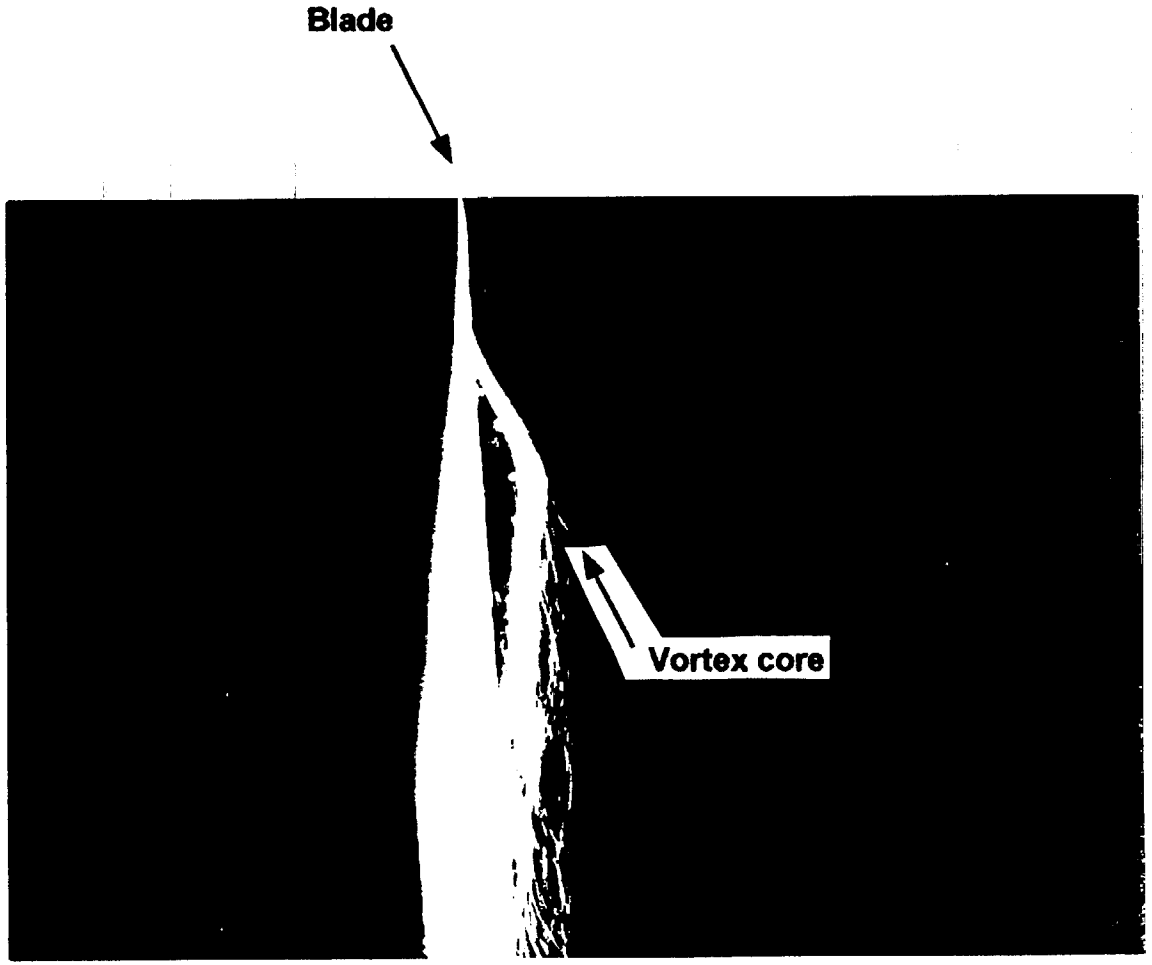

(b)

Figure 37. Flow visualization for z_s = -.063, Re_c = 130,000, $\alpha_1 = \alpha_2 = 10°$. (a) Side view. (b) View from wing root.

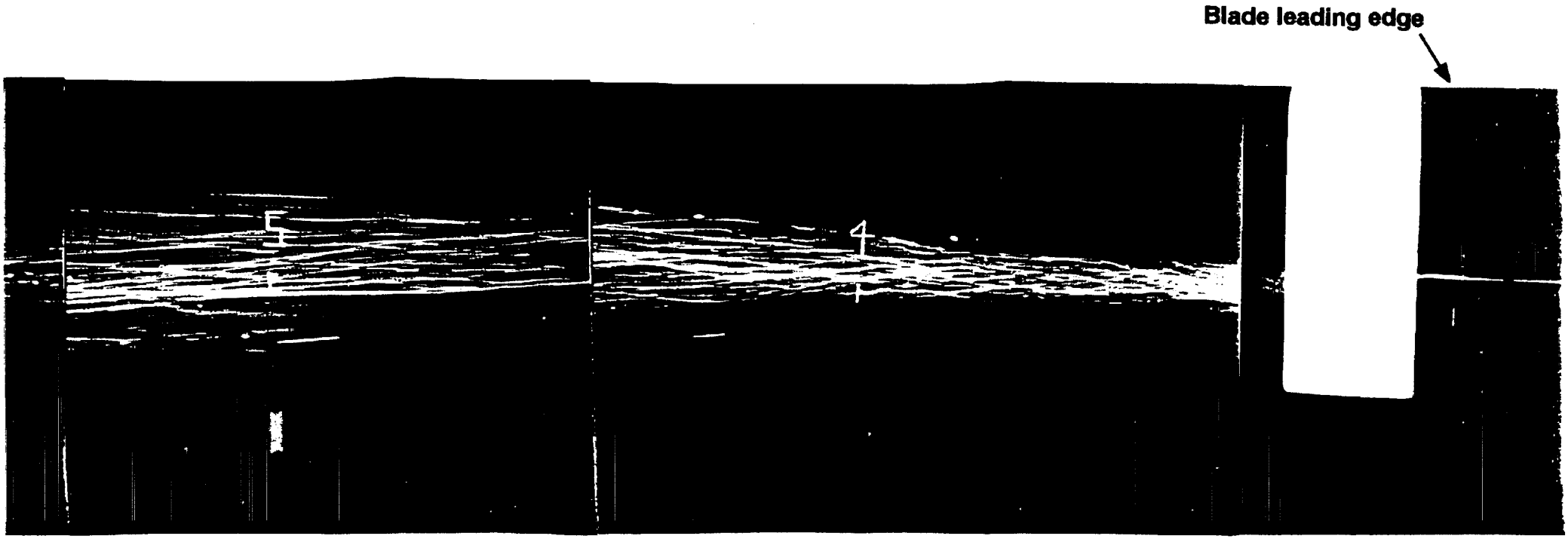

(a)

Figure 38. Flow visualization for z_s = -.125, Re_c = 130,000, $\alpha_1 = \alpha_2 = 10°$. (a) Side view. (b) View from wing root.

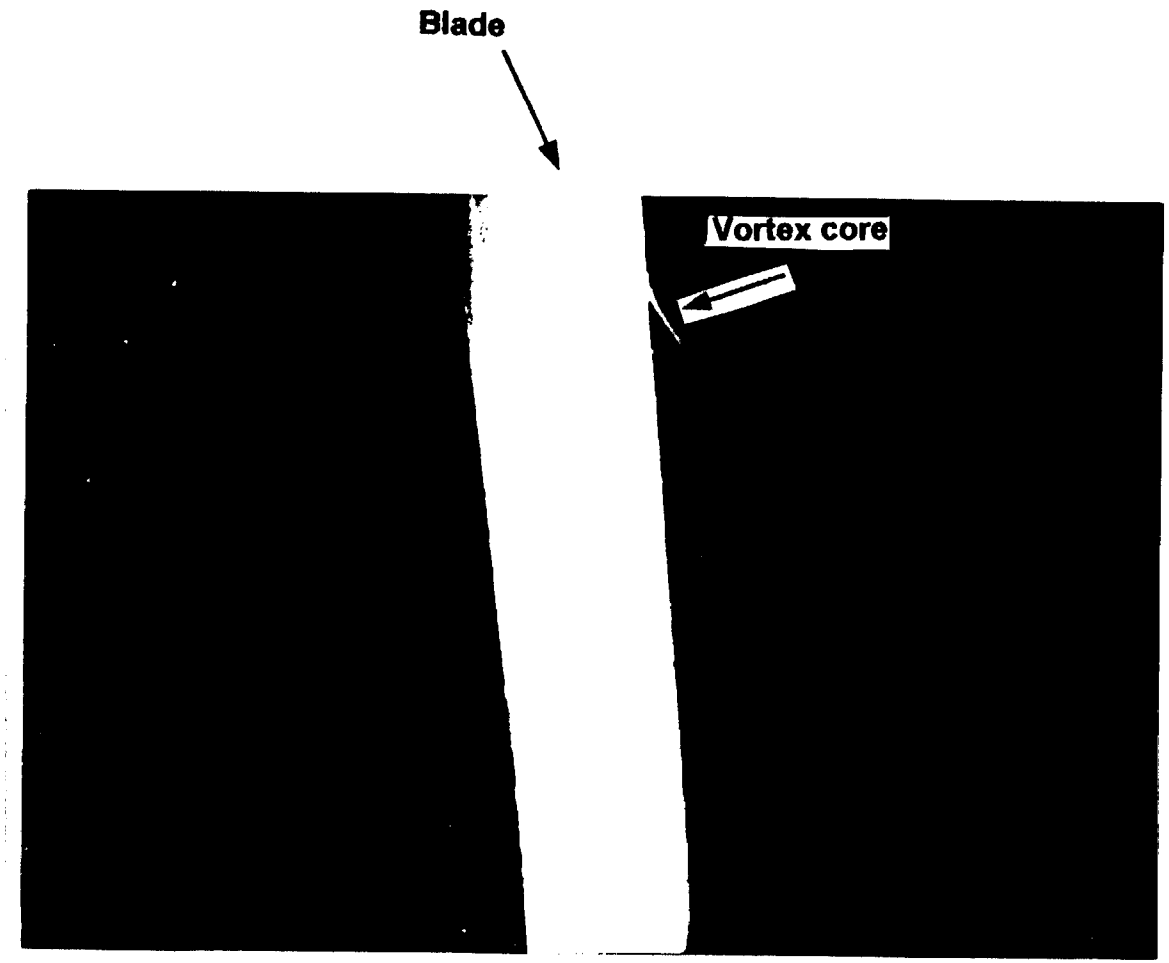

(b)

Figure 38. Flow visualization for z_s = -.125, Re_c = 130,000, $\alpha_1 = \alpha_2 = 10°$. (a) Side view. (b) View from wing root.

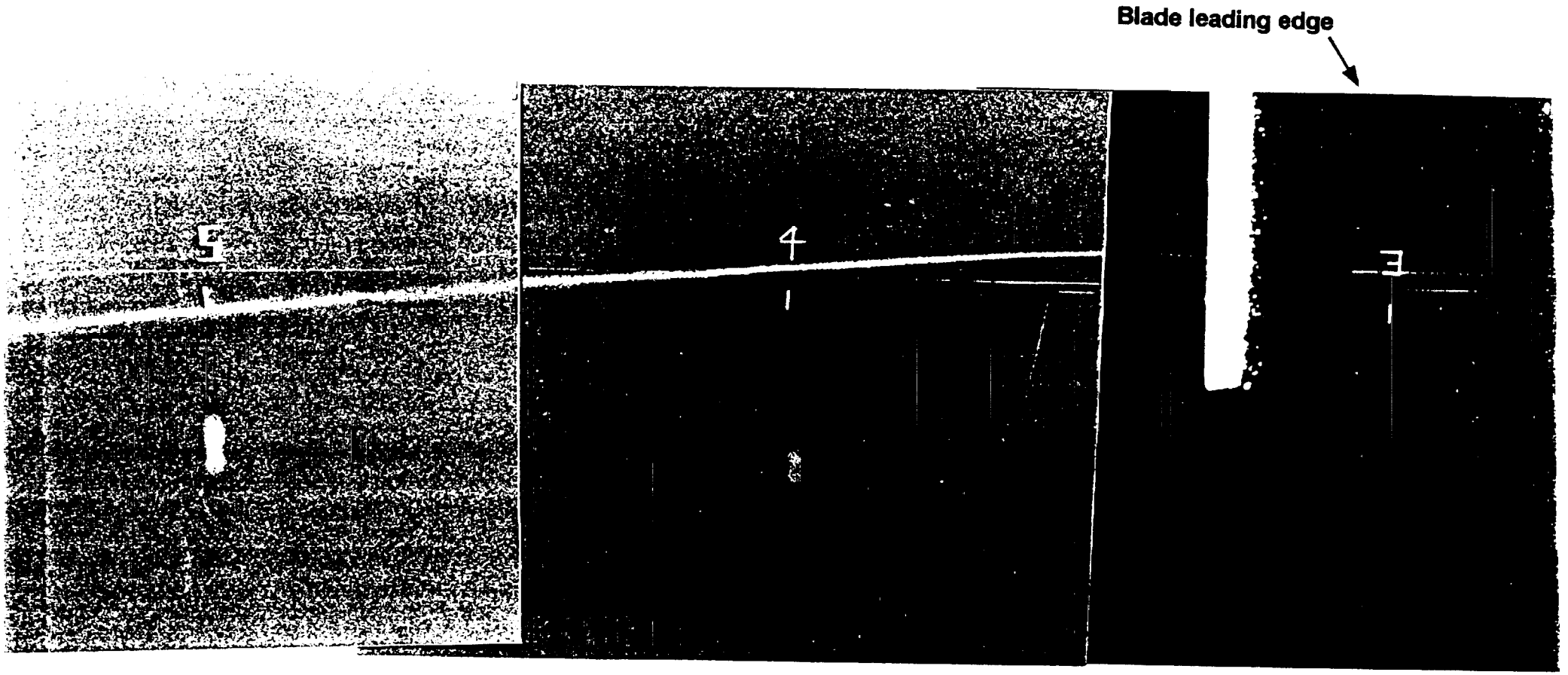

Figure 39. Flow visualization for z_s = .125, Re_c = 260,000, $\alpha_1 = \alpha_2 = 10°$. Side view.

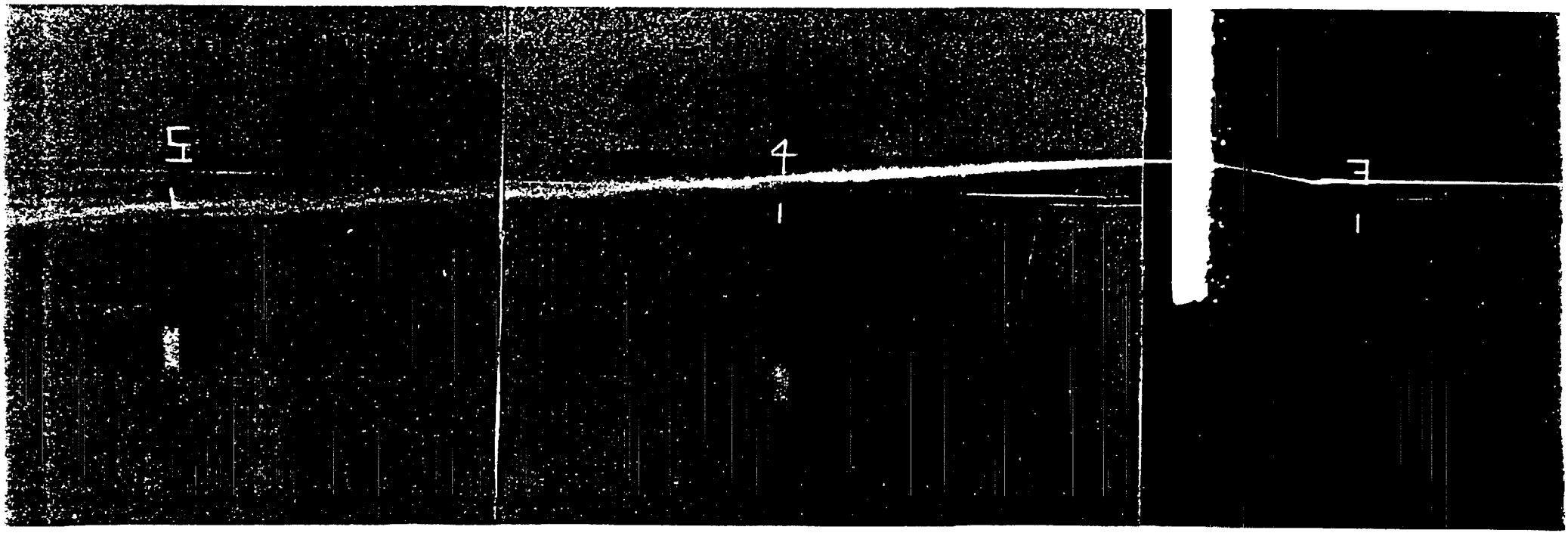

Figure 40. Flow visualization for z_s = .063, Re_c = 260,000, $\alpha_1 = \alpha_2 = 10°$. Side view.

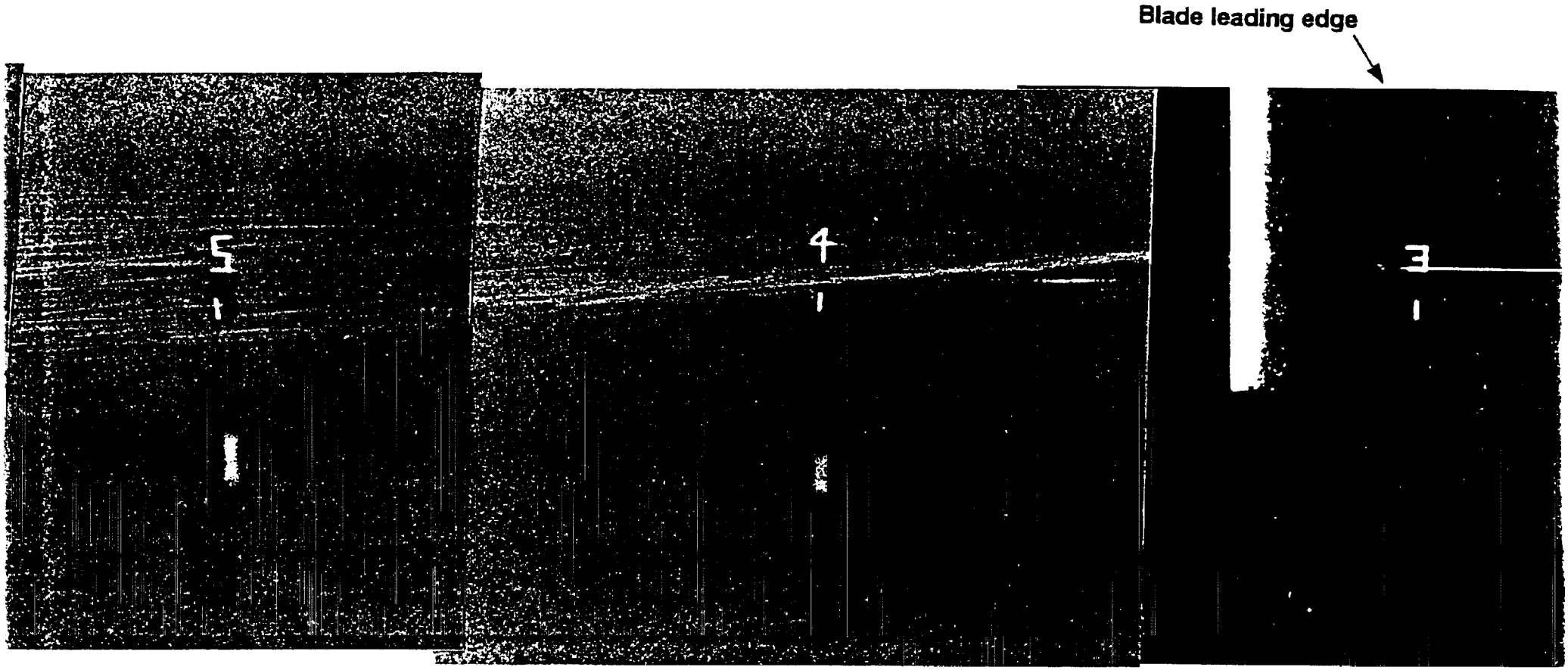

Figure 41. Flow visualization for z_s = .031, Re_c = 260,000, $\alpha_1 = \alpha_2 = 10°$. Side view.

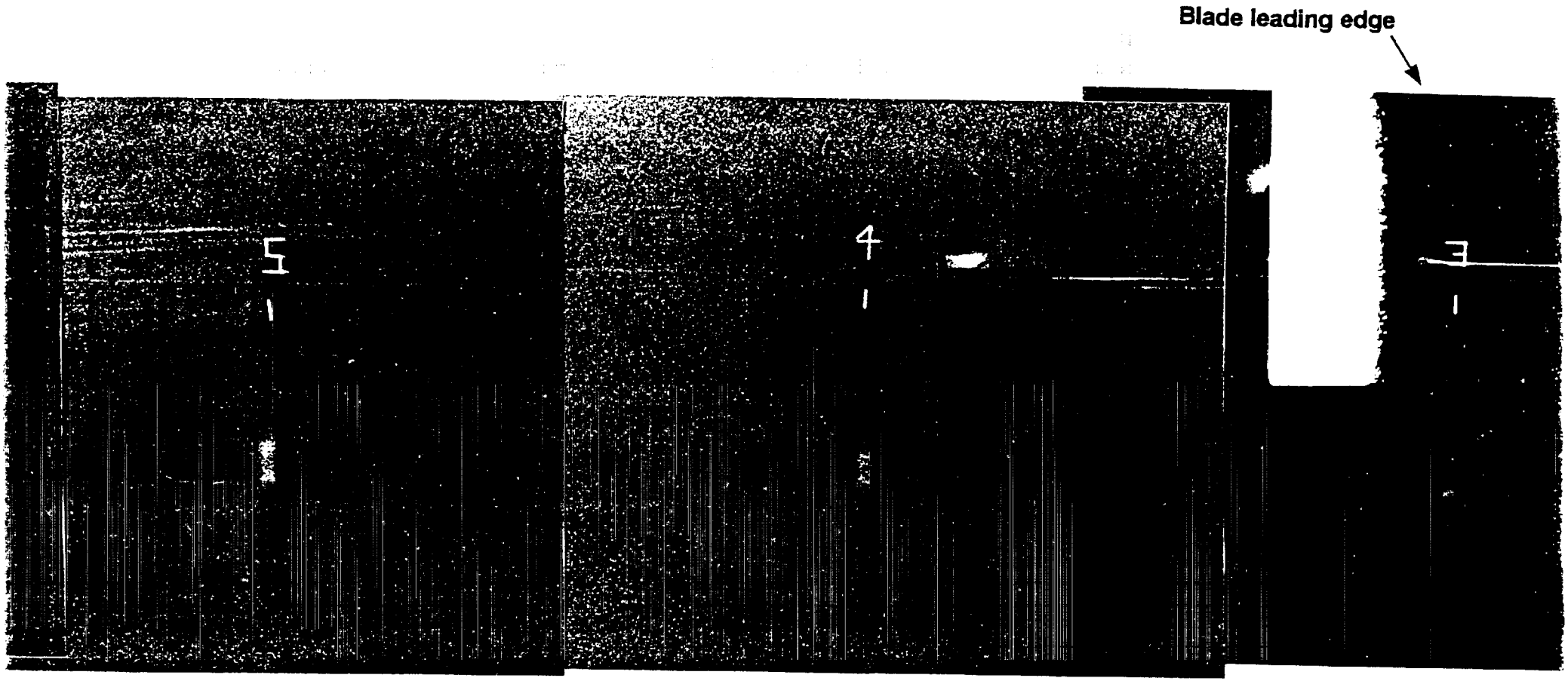

Figure 42. Flow visualization for z_s = .0, Re_c = 260,000, $\alpha_1 = \alpha_2 = 10°$. Side view.

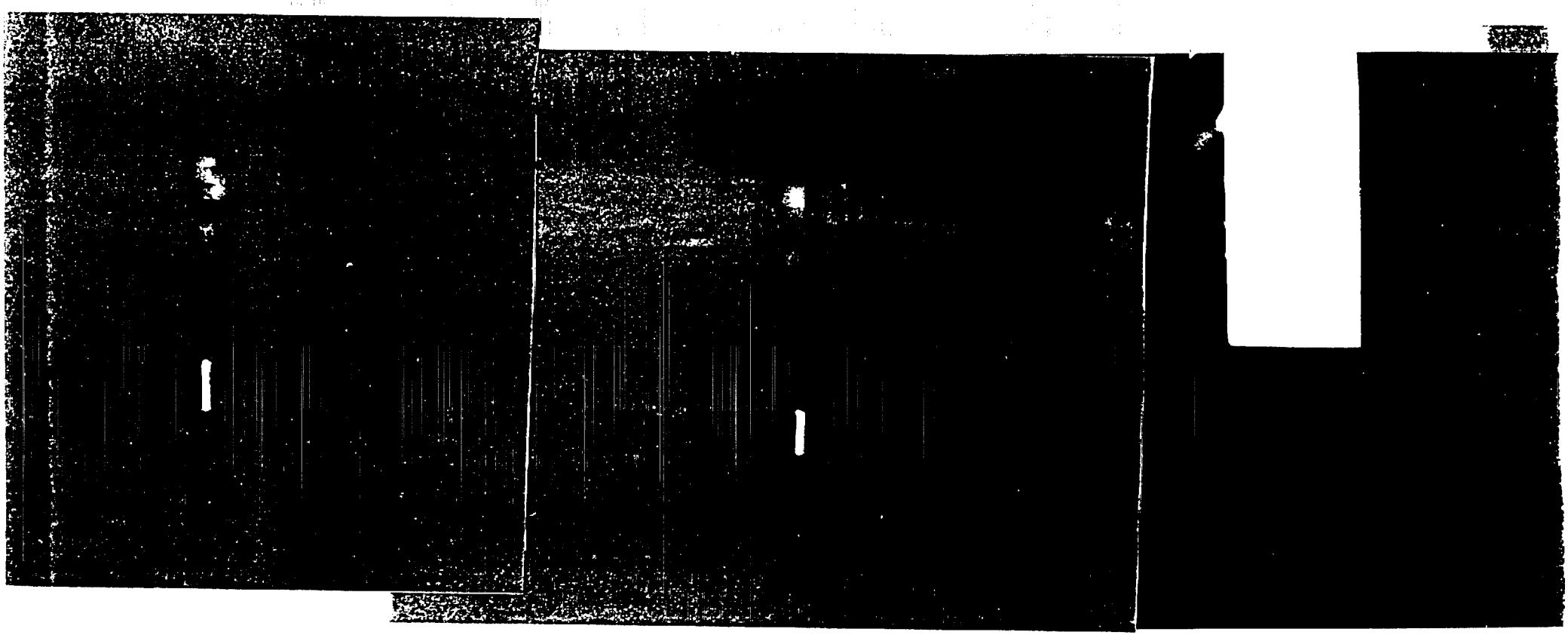

Figure 43. Flow visualization for z_s = -.031, Re_c = 260,000, $\alpha_1 = \alpha_2 = 10°$. Side view.

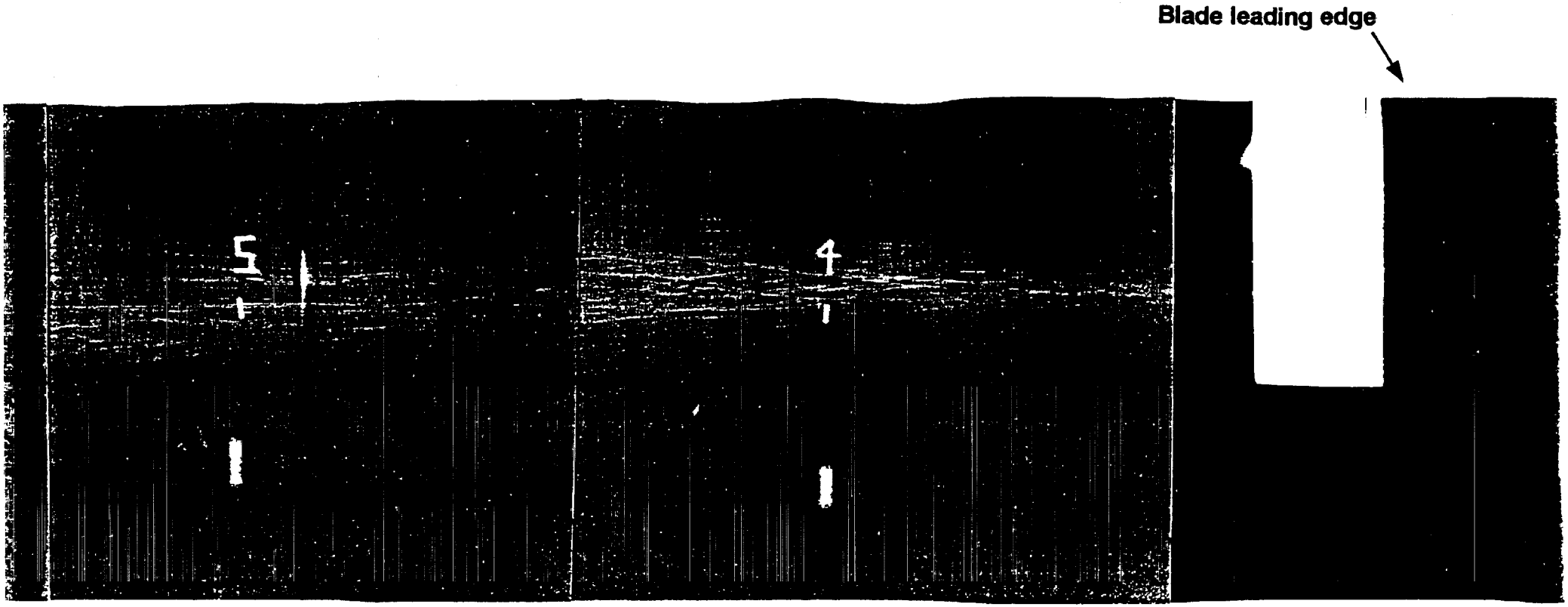

Figure 44. Flow visualization for z_s = -.063, Re_c = 260,000, $\alpha_1 = \alpha_2 = 10°$. Side view.

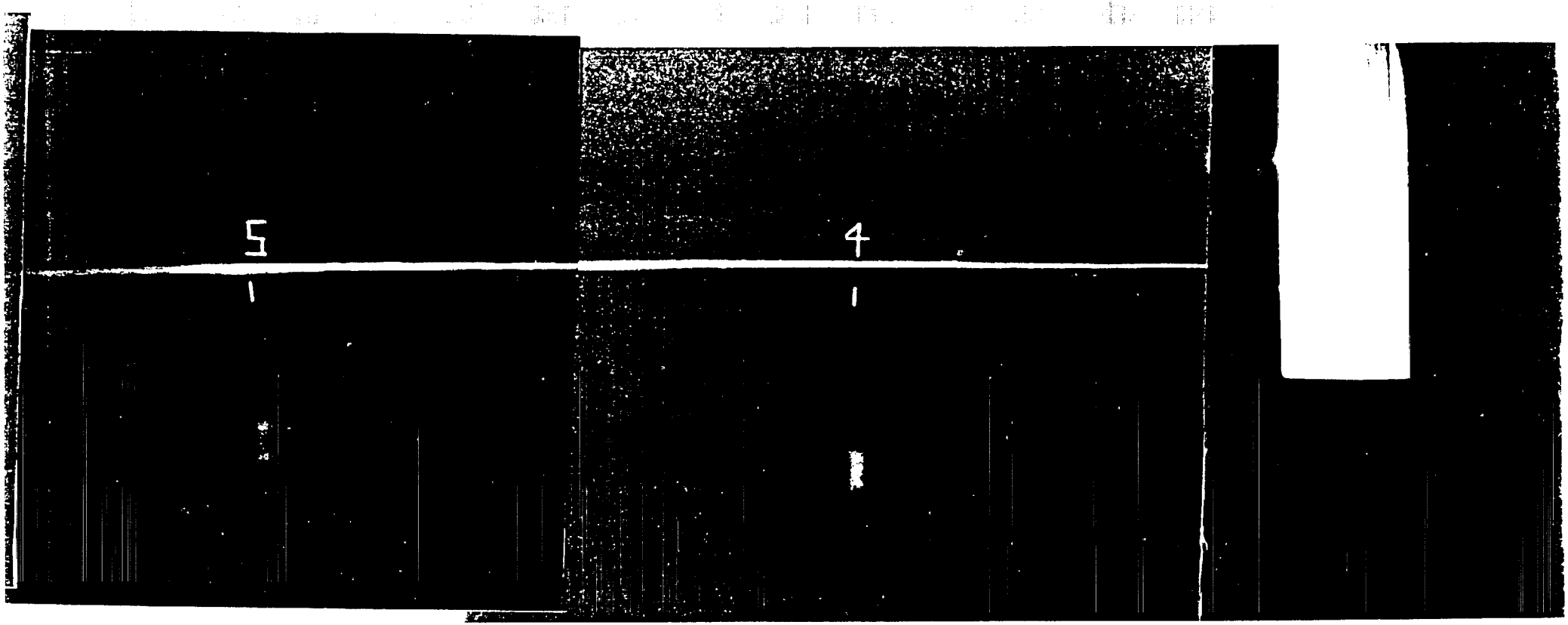

Figure 45. Flow visualization for z_s = -.125, Re_c = 260,000, $\alpha_1 = \alpha_2 = 10°$. Side view.

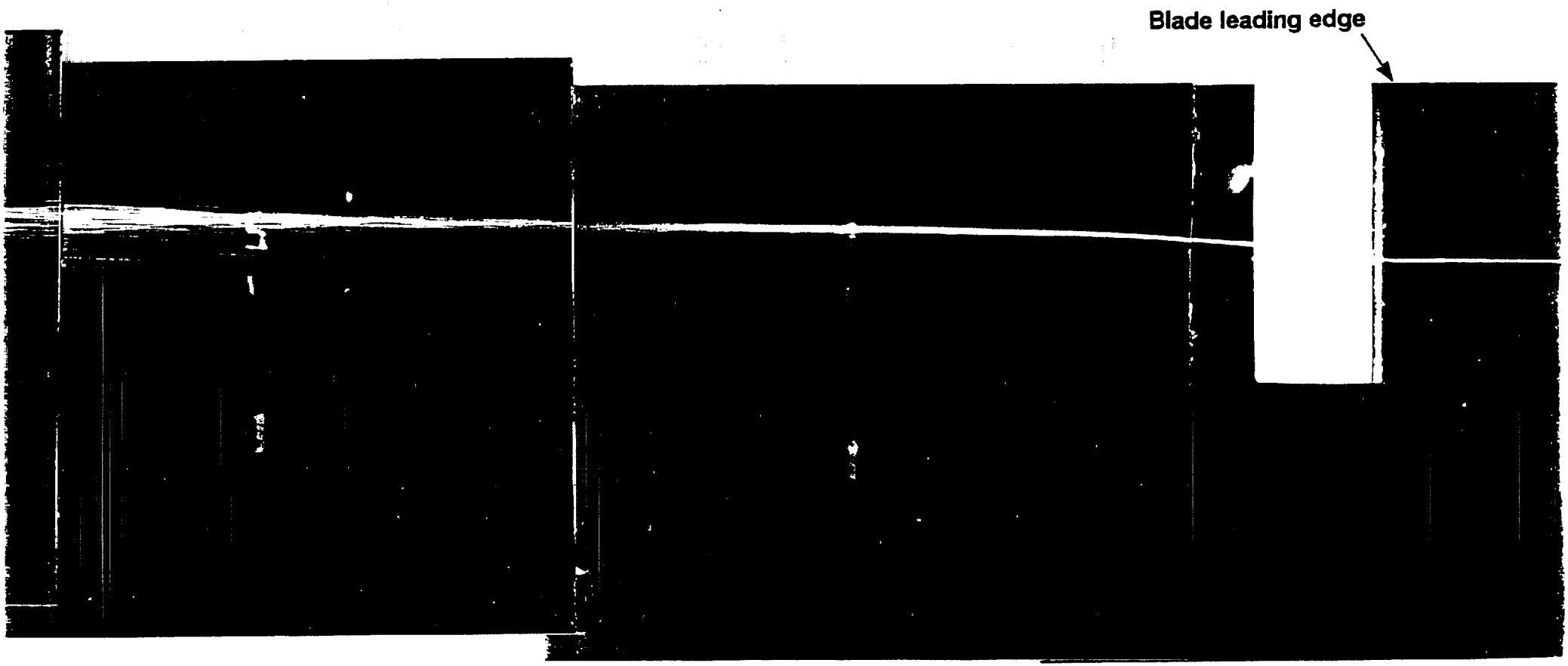

Figure 46. Flow visualization for z_s = .063, Re_c = 260,000, α_1 = 5°, α_2 = 0°. Side view.

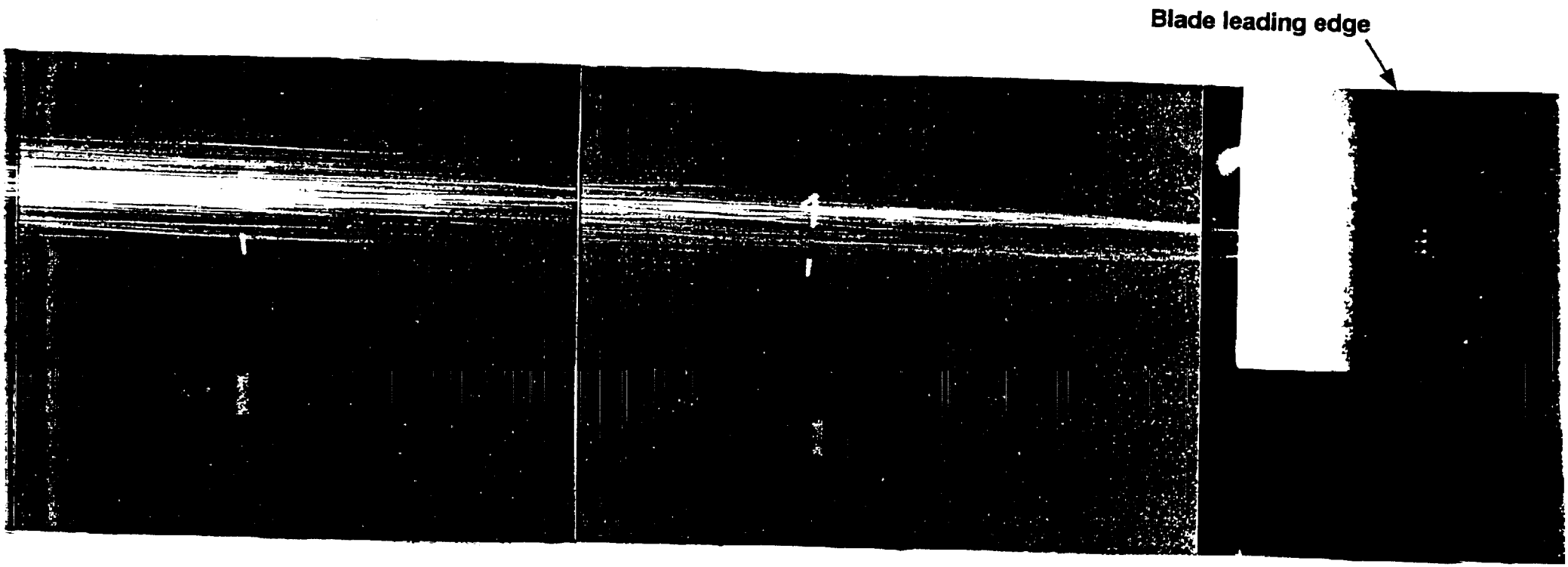

Figure 47. Flow visualization for z_s = .0, Re_c = 260,000, α_1 = 5°, α_2 = 0°. Side view.

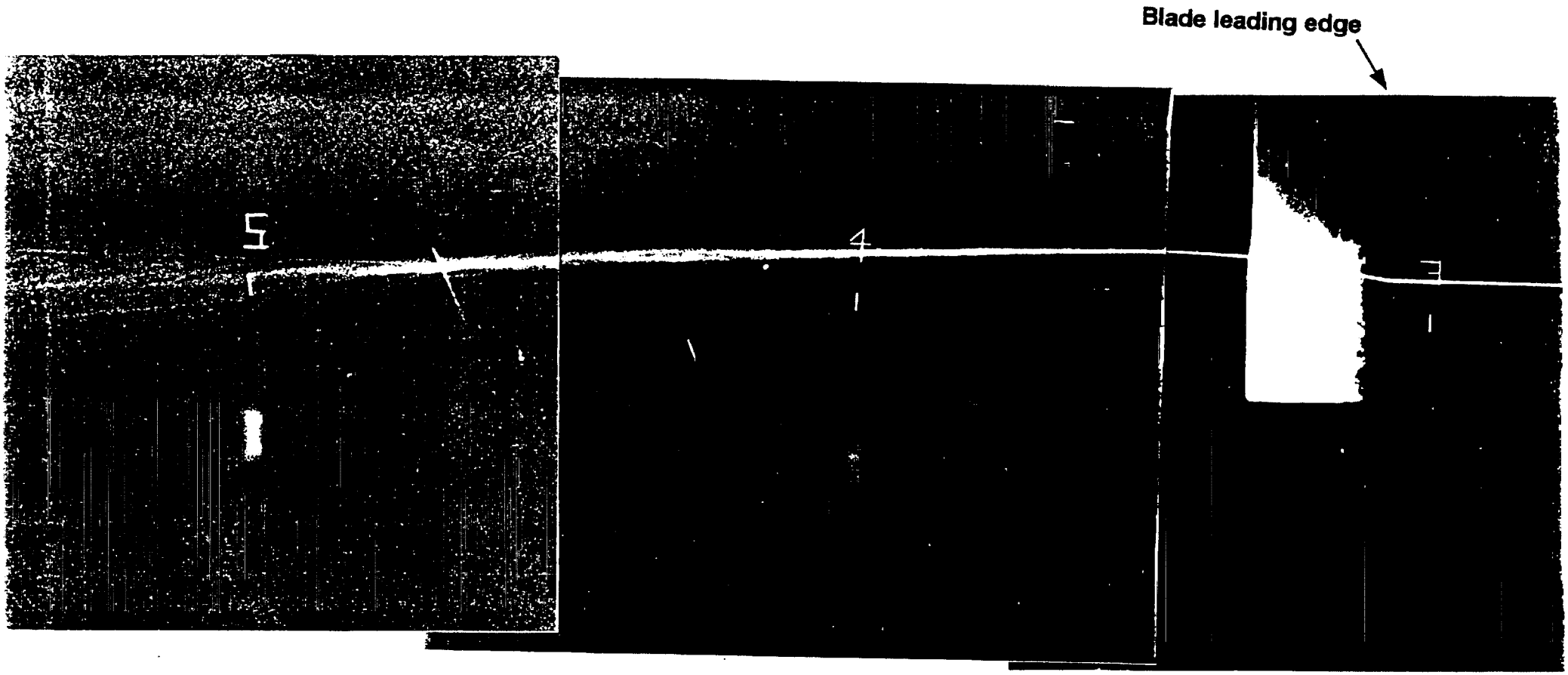

Figure 48. Flow visualization for z_s = .063, Re_c = 260,000, α_1 = 10°, α_2 = 5°. Side view.

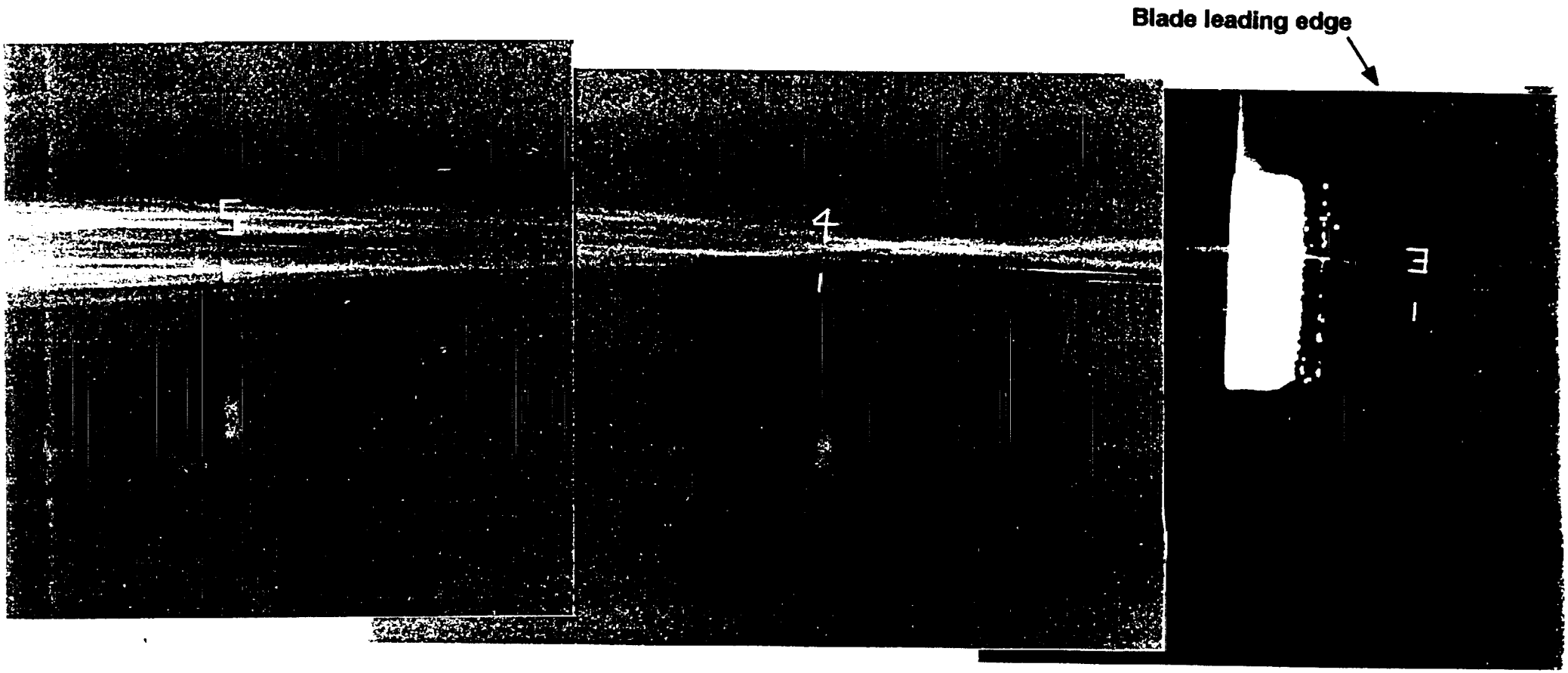

(a)

Figure 49. Flow visualization for $z_s = .0$, $Re_c = 260{,}000$, $\alpha_1 = 10°$, $\alpha_2 = 5°$. (a) Side view. (b) Detail of burst region.

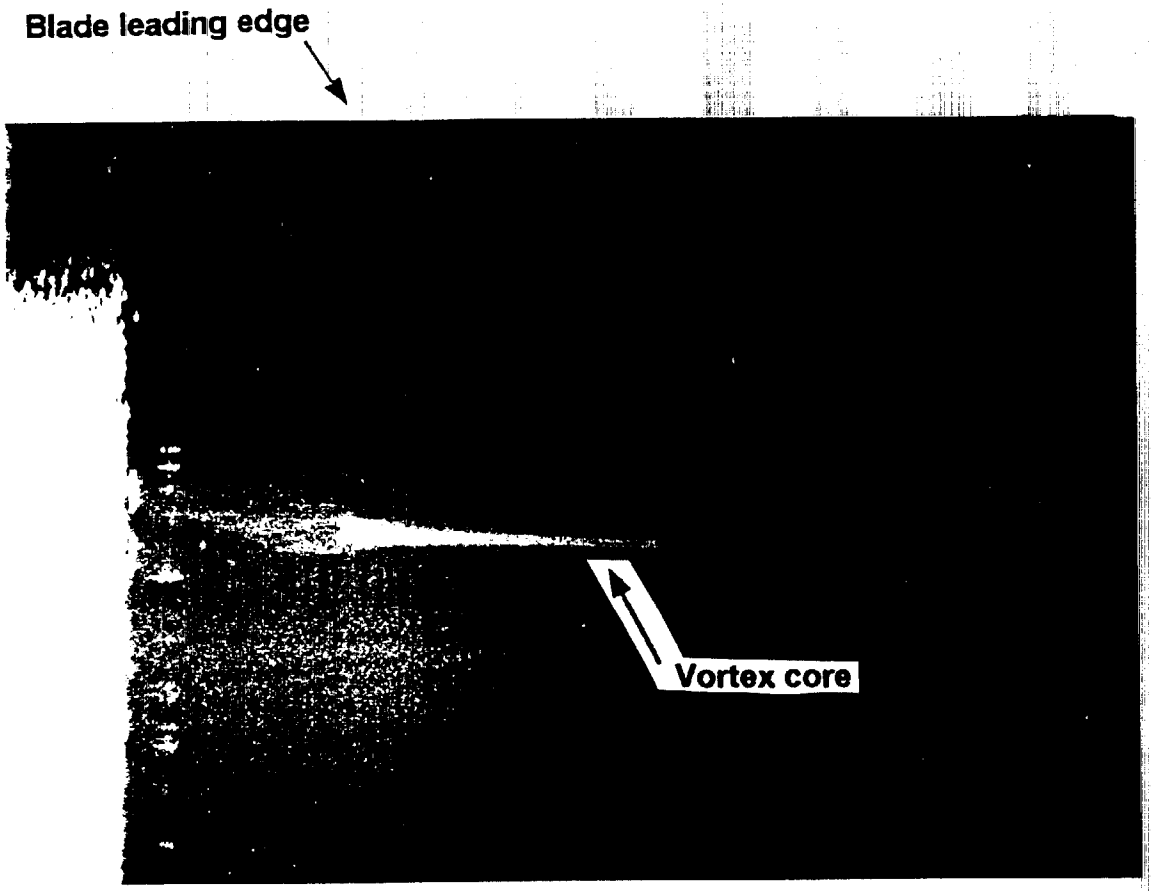

(b)

Figure 49. Flow visualization for $z_s = .0$, $Re_c = 260{,}000$, $\alpha_1 = 10°$, $\alpha_2 = 5°$. (a) Side view. (b) Detail of burst region.

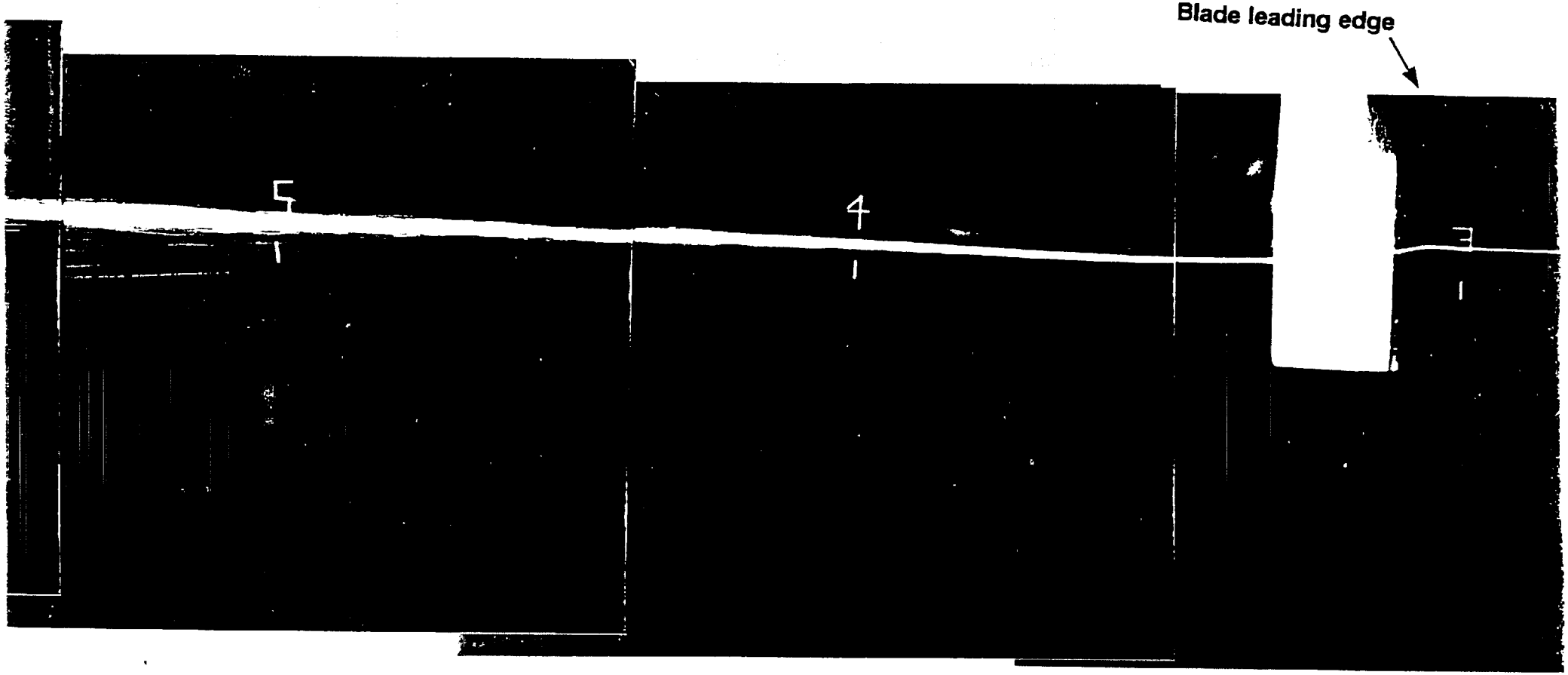

Figure 50. Flow visualization for z_s = -.063, Re_c = 260,000, α_1 = 10°, α_2 = 5°. Side view.

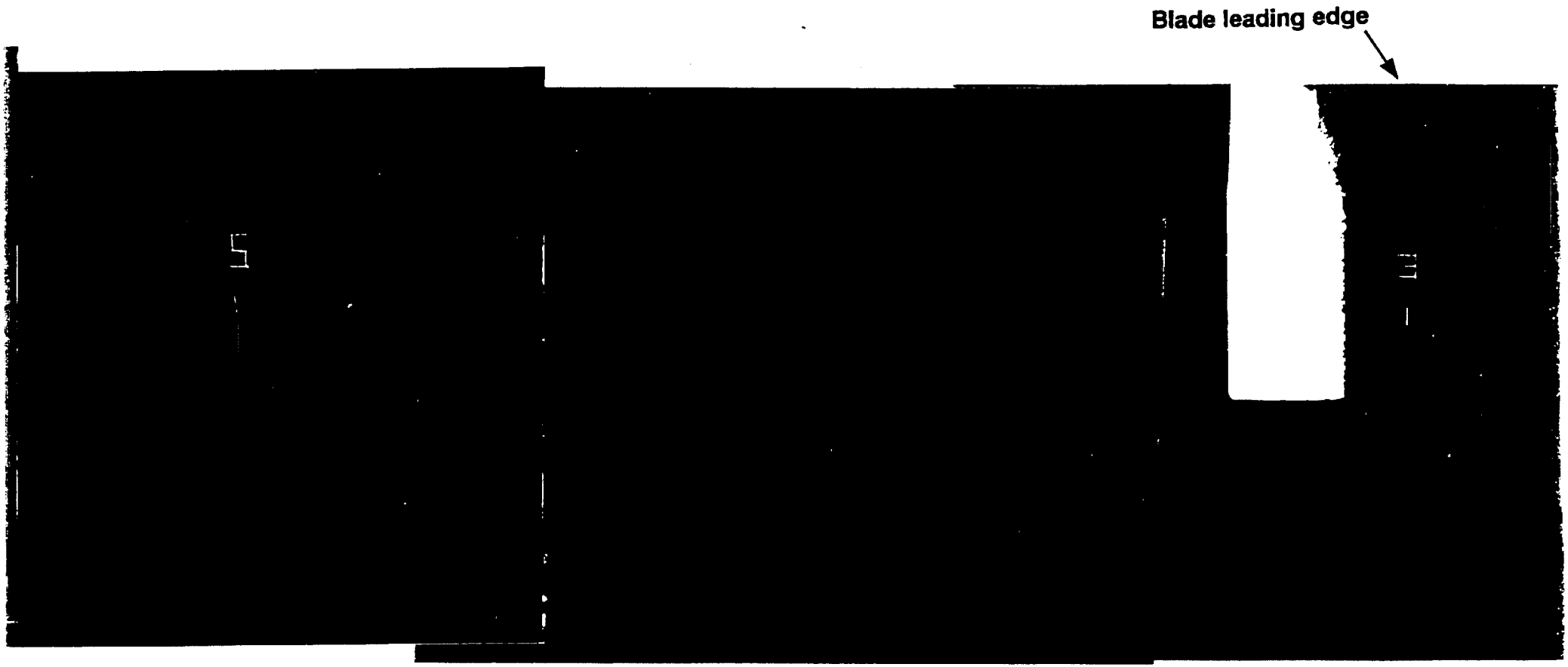

Figure 51. Flow visualization for z_s = .063, Re_c = 260,000, α_1 = 10°, α_2 = 0°. Side view.

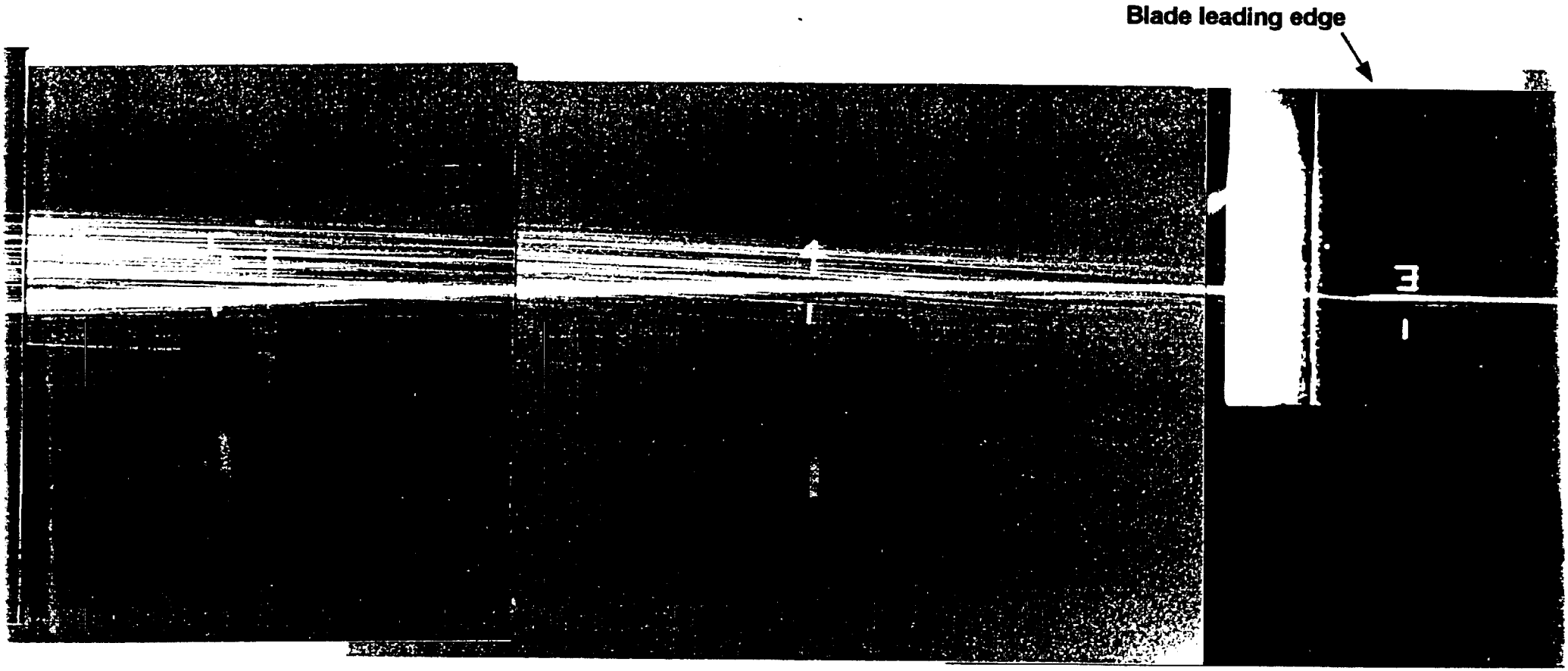

Figure 52. Flow visualization for z_s = .063, Re_c = 260,000, α_1 = 2.5°, α_2 = 5°. Side view.

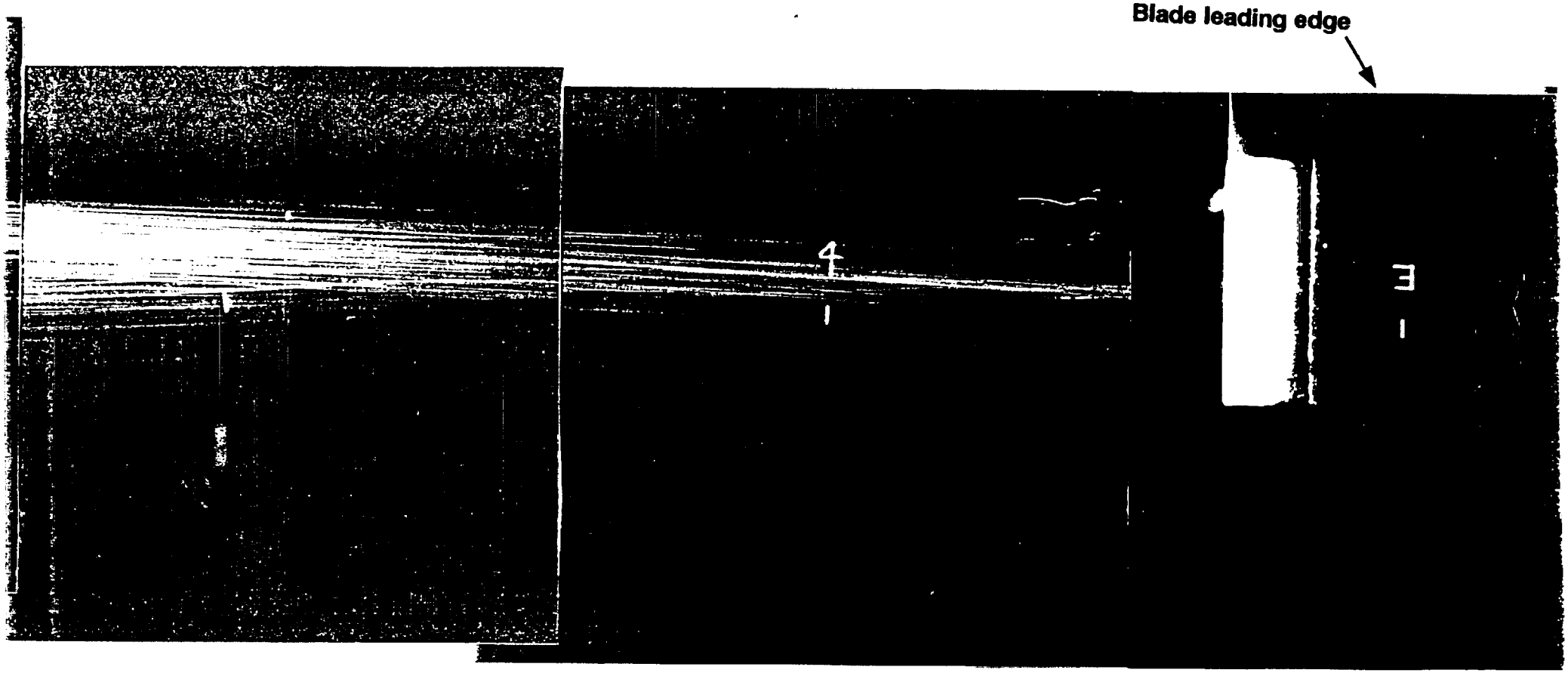

Figure 53. Flow visualization for $z_s = .0$, $Re_c = 260{,}000$, $\alpha_1 = 2.5°$, $\alpha_2 = 5°$. Side view.

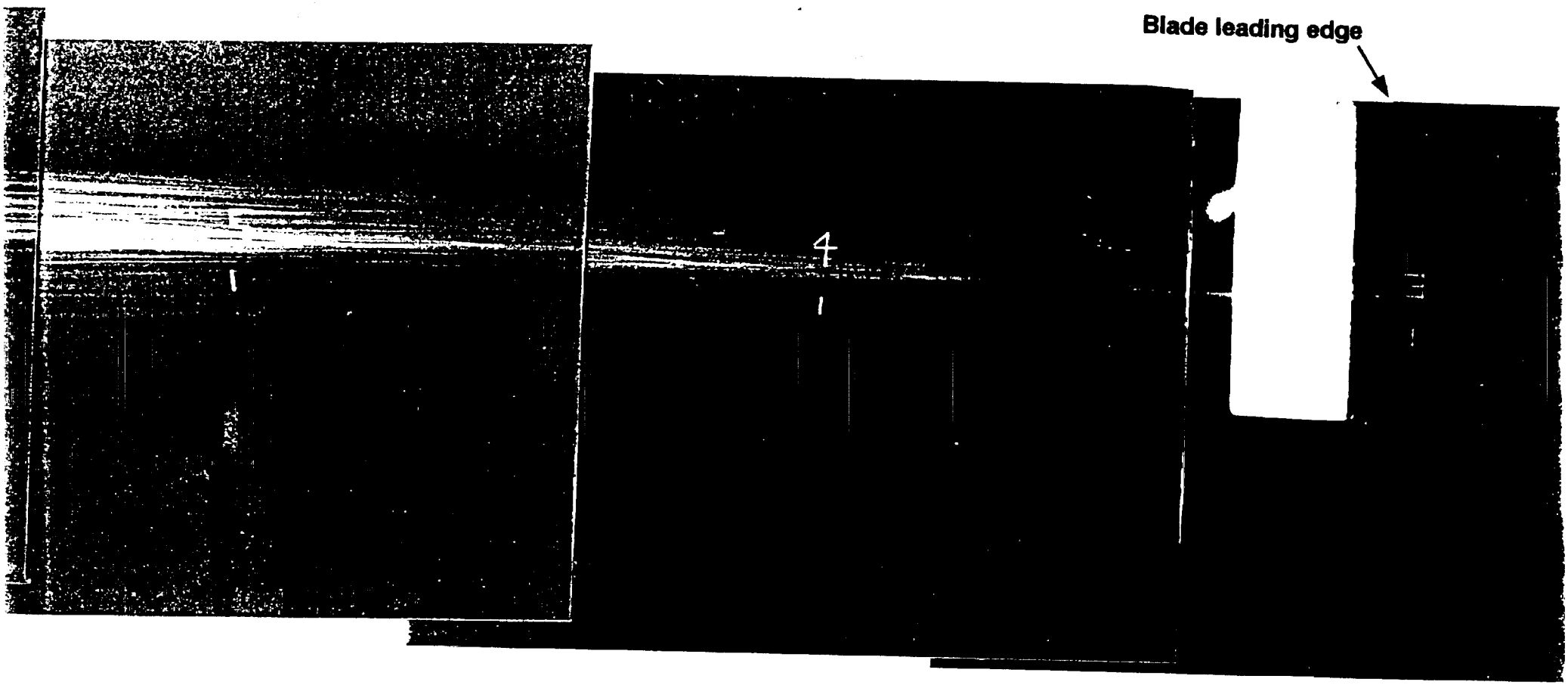

Figure 54. Flow visualization for z_s = .-063, Re_c = 260,000, α_1 = 2.5°, α_2 = 5°. Side view.